University of Rhode Island

DigitalCommons@URI

2018

EXPERIMENTAL AND NUMERICAL SIMULATIONS FOR FLUID BODY INTERACTION PROBLEMS

Amin Mivehchi
University of Rhode Island, aminmivehchi@gmail.com

Follow this and additional works at: https://digitalcommons.uri.edu/oa_diss

EXPERIMENTAL AND NUMERICAL SIMULATIONS FOR FLUID BODY

INTERACTION PROBLEMS

BY

AMIN MIVEHCHI

A DISSERTATION SUBMITTED IN PARTIAL FULFILLMENT OF THE

REQUIREMENTS FOR THE DEGREE OF

DOCTOR OF PHILOSOPHY

IN

OCEAN ENGINEERING

UNIVERSITY OF RHODE ISLAND

2018

DOCTOR OF PHILOSOPHY DISSERTATION

OF

AMIN MIVEHCHI

APPROVED:

Dissertation Committee:

Major Professor   Jason M. Dahl

Stephan T. Grilli

Stephen Licht

Kathleen Donohue

Nasser H. Zawia
DEAN OF THE GRADUATE SCHOOL

UNIVERSITY OF RHODE ISLAND

2018

ABSTRACT

This dissertation focuses on the experimental and numerical modelling of fluid structure interaction (FSI) problems. The main objective of this work was to develop state-of-art experimental and numerical tools to investigate a variety of Fluid-Structure Interaction problems. This topic is of critical importance to Naval Hydrodynamics and offshore applications,such as in ship design, floating offshore wind platforms and offshore ocean energy systems.

On the experimental modelling of FSI, this dissertation includes detailed of state-of-art hydrodynamic testing tank system for studying biomimetic fluid-structure interaction problems. This system was employed to study unsteady ground effect for pitching and heaving flapping foil propulsors in the near near presence of a wall. More than 2000 experiment were conducted demonstrating the dynamic ground effect on lift and thrust with flapping foil propulsor as a function of Strouhal number, distance from the wall, and foil kinematics. It was demonstrated that 2D and 3D ground effect in a dynamically flapping system are fundamentally different.

The dissertation also focus on the development and improvement of a numerical wave tank based on fully nonlinear potential flow method accelerated with the Fast Multipole Method (FMM) for advanced FSI problems. In the past 30 years, increasingly accurate and efficient models have been developed to simulate nonlinear wave propagation and transformations over a varying nearshore bathymetry as well as their interactions with submerged and surface piercing fixed or floating structures. One successful approach has been based on models solving Fully Nonlinear Potential Flow (FNPF) theory, by a higher-order Boundary Element Method (BEM), in 2D and 3D. Such models can accurately simulate overturning waves and have been used to investigate their physical properties just before

breaking.In this thesis, an improved Numerical Wave Tank (NWT) based on BEM-FNPF is discussed with developed improvements for implementation with a fast hybrid BEM-LBM solver for ship seakeeping simulations. In particular, improvements are developed to incorporate compatibility condition in 3D corner intersections and implementation method to suppress wave breaking in 3D potential flow simulations.

In many naval hydrodynamics and ocean/coastal engineering applications, it is desirable to prevent steep waves from overturning as this eventually leads to instabilities and stops computations. A number of methods have been proposed to do so, some based on specifying an "absorbing surface pressure", similar to the method used in absorbing beaches. A method is implemented in the NWT using Hilbert transform tracking of wave crest to implement slope and curvature based criteria to identify and suppress breaking waves.Impending breaking is detected based on local maximum free surface slope/steepness criterion, and wave energy absorbed using local "absorbing pressure" patch whose strength is calibrated with a physical criterion.The method is validated for a submerged hydrofoil generating waves at the free surface with experiments from Duncan(1981).

ACKNOWLEDGMENTS

First and foremost, I would like to express my deepest gratitude to my advisors Dr. Jason Dahl and Prof. Stephan Grilli for their guidance and continuous support of my doctoral studies. Their guidance helped me a lot throughout my time at the University of Rhode Island.

Stephan and Jason has provided a supportive environment that has allowed me to explore my interests, and I am grateful for their patience and optimism about my work. Their attention to detail and dedication to exceptional scientific writing have made each of our manuscripts a work of art. It has been an honor to work with both of them and a great pleasure to be their student.

Also, I want to express my gratitude to Dr. Stephen Licht and Dr. Jeff Harris, for their full support and encouragement during the years of my PhD. Their insight and expertise help me to improve my work to higher level.

I wish to thank my committee members, Dr. Stephen Licht, Dr. Kathleen Donohue and Dr. Donna Meyer, who were more than generous with their expertise and precious time. I thank my friends and colleagues, Gail Paolino, Fred Pease, Robin Freeland, Amanda, Amir, Tayebeh, Chris, Lauren, Jack, Erdem, Deniz, Mustafa, Eric and JJ for a pleasant working environment during my 6 years of PhD.

Also, I would like to extend my greatest appreciation to my family who have always supported me in my academic pursuits.

DEDICATION

I dedicate this dissertation work to my parents, who offered unconditional love and support and have always been there for me. Thank you so much.

PREFACE

This dissertation, *Experimental and Numerical Simulations for Fluid-Structure Interaction Problems*, is constructed in the manuscript format and consists of 4 manuscripts.

The first manuscript (chapter 1), *Heaving and pitching oscillating foil propulsion in ground effect* was published in Journal of Fluids and Structures, 63 (2016) 174-187.

The second manuscript (chapter 2) is *A Hybrid Solver Based on Efficient BEM-Potential and LBM-NS Models: Recent BEM Developments and Applications to Naval Hydrodynamics*, is published as a conference proceeding in the 27th Offshore and Polar Engng. Conf. ISOPE17, San Francsico, USA. (2017), 721-728.

The third manuscript (chapter 3), *Identification and individual energy absorption of breaking waves in 3D fully nonlinear BEM simulations.*, will be submitted to Journal Engineering Analysis with Boundary Element Method.

The forth manuscript (chapter 4), *Three Dimensional Boundary Element Solution of Nonlinear Wave Flow with Uniform Cubic B-Spline Elements and Corner Treatments.*, will be submitted to Journal of Engineering Analysis with Boundary Element Method.

TABLE OF CONTENTS

LIST OF FIGURES

xiv

LIST OF TABLES

MANUSCRIPT 1

Heaving and pitching oscillating foil propulsion in ground effect

by

Amin Mivehchi, Jason Dahl, Stephen Licht

Department of Ocean Engineering, University of Rhode Island, Narragansett, RI 02881, USA

Abstract

A detailed series of experiments is performed to investigate the 'ground effect' experienced by propulsive flapping foils operating near a solid boundary. A high aspect ratio foil is towed at constant speed and oscillated in pitch and heave at varying distances from a rigid wall. It is shown that this distance has a significant impact on the lift and thrust forces generated by the foil, both in the time averaged mean forces and the phase averaged periodic forces. For some thrust producing kinematics, the instantaneous force profile may change significantly without altering the time averaged mean force; thus, mean force measurements alone are not sufficient to indicate the proximity, or the effect, of the solid boundary. Results are presented across a wide range of thrust generating kinematics, showing that the strength of the ground effect can be modulated, for any achievable level of thrust, through appropriate selection of kinematics. This finding in particular has significance for underwater vehicles propelled by oscillating foil thrusters, as it follows that the sensitivity of the thrusters to ground effect can be controlled independently of the desired thrust. While propulsive efficiency is increased slightly near the wall for some kinematics, in general this does not occur for kinematics where a strong ground cushion (repulsion) effect is observed. Finally, the results suggest that span-wise flow around the tip of the foil is important in determining whether the foil is repelled from or pulled into the wall.

1.1   Introduction

At least since Gray [1] , biologists and engineers have actively studied how aquatic animals propel themselves through the water with foils, fins, and other active control surfaces. Research on biological propulsion methods has had the dual goal of (a) understanding animal morphology and behavior from an evolutionary biology perspective, and (b) extracting useful techniques and principles that can

be applied to the engineering development of man-made underwater vehicles. One engineering rationale for the use of alternative propulsion approaches is the desire to use unmanned underwater vehicles (UUVs) in dynamic, shallow water environments. In near-bottom operations, the impact of the solid bottom boundary on the propulsor dynamics is of critical importance; indeed, gliding birds Reyner [2] and swimming and 'flying' fish (Nowroozi et. al. [3] and Park and Choi [4]) are believed to take advantage of near-ground and near-boundary effects to reduce cost-of-transport.

In steady flight, the physical mechanisms by which a 'ground effect' arises when an airfoil is operated near the ground is a well understood phenomena that has been exhaustively researched in the aeronautical engineering literature [5]. While fixed foils produce lift and a small amount of drag with a steady wake, oscillating foils can produce both thrust and lift with a fundamentally unsteady fluid wake [6]. It is therefore expected that an oscillating foil's interactions with the ground will arise from different, time dependent physical mechanisms. The growing body of research into ground effect in oscillating foils has approached the problem using a variety of numerical and experimental techniques.

1.1.1 Experimental Studies

The creation of robotic models has become a standard technique in both biological and engineering focused research into oscillatory propulsors. These models, which are of varying fidelity to the biological muse according to the motivation for the experimenters, are used to measure the force, power, and wake structure generated by moving the propulsors through water with different kinematics. Examples of robotic investigations of oscillating propulsors in the free-stream, i.e. far from obstacles or surfaces, include systems which rely on deformation of highly flexible structures such as ribbon fins [7, 8] and batoid wings [9], as well as systems where

3

rigid foils are actuated in one [10] or two [11] degrees of freedom.

Fernandez-Pratz et al.[12] experimentally investigated pitching-only oscillating foils near the wall using a very flexible, very low aspect ratio foil ($AR = 0.9$) with span-wise flow allowed over both ends. Quinn et al.[13] investigated a rigid, surface piercing foil spanning an entire flow channel ($AR = \infty$) with no spanwise flow allowed at either end. Quinn et al.[14] and Belvins and Lauder[15] also investigated a very flexible, very low aspect ratio foil ($AR = 0.5$), in this case to experimentally study undulatory swimming. A traveling wave was generated in this foil by actuating the leading edge of the foil in heave as well as pitch; spanwise flow was allowed around both ends. Quinn et al.[13] is the only previous case in which "high net thrust conditions" are considered, i.e. $0.25 < St < 0.45$.

Table 1: Comparison of Existing Literature to Present Effort

	AR	Flexibility	Spanwise Flow	Relative Flow	Actuation
Fernandez-Pratz et al. (2015)	0.9	Very Flexible	Allowed Both Ends	Self-Propelled	Pitch Only
Blevins and Lauder (2013)	0.5	Very Flexible	Allowed Both Ends	Self-Propelled, Flow Channel	Heave and Pitch, Undulatory
Quinn et al.(2014a)	∞	Very Flexible	Allowed Both Ends	Self-Propelled, Flow Channel	Heave and Pitch, Undulatory
Quinn et al.(2014b)	∞	Rigid	Blocked	Flow Channel	Pitch Only
Current Work	4.9 and ∞	Rigid	Allowed at Tip	Towed	Heave and Pitch

Although the methods and morphologies vary greatly across the four experimental studies, as laid out in Table 1, there is a clear consensus that operating

in proximity to the ground can have a significant effect on mean lift and thrust production. Both Fernandez-Prats et al. [12] and Blevins and Lauder [15] found that swimming speed increased for given kinematics at very close approaches to the ground. Using a similar apparatus as Blevins and Lauder [15] but with varying flexibility of the undulating foil, Quinn et al. [14] found that increased swimming speed near the wall did not necessarily translate to lower cost of transport. Quinn et al. [13] found that once close enough to the ground for an effect to be measured, thrust increased monotonically with ground proximity, with no experimentally measurable efficiency changes; in addition, a stable equilibrium position with zero net lift and 40% thrust improvement was identified.

another focus for previous experiments is the effect of the ground on hovering and vertical take-off dynamics of insects [16], where take-off kinematics are mimicked using a dynamically scaled model of a beetle wing, or in the case of Lu et al. [17], using an oscillating elliptical wing (with nominally infinite aspect ratio) undergoing linear and rotational motions. Both experiments demonstrate a near ground effect, although by design, the mean thrust force is oriented perpendicular to the wall, rather than parallel to the wall as in the present study, so no direct comparison to the results of the present study is appropriate.

1.1.2 Numerical Studies

Numerical studies of oscillating foils in ground effect have covered a wide range of applications, largely focusing on undesired airfoil perturbations. Liang et al. [18] simulated heaving only motion of aircraft wings at $Re = 7.0 \times 10^4$ using a discrete vortex potential flow approach. Molina and Zhang [19] used an unsteady Reynolds averaged Navier-Stokes solver to simulate pitching only foil motion for race car spoilers at $Re = 3.9 \times 10^4$ while Moryossef and Levy [20] attempted to isolate inviscid and viscous effects for race car spoilers.

Wu et al. [21] used an immersed boundary-lattice Boltzmann method to investigate hovering performance of insects, and used the same techniques for studying energy extraction from a uniform flow with heaving and pitching foils at Re near 1000 [22, 23].

1.1.3 Contribution

The current work is an experimental characterization of instantaneous and mean thrust production in ground effect for oscillating foils. It is the first published effort to measure forces on a two-degree of freedom high aspect ratio foil near a wall *with span-wise flow* allowed. In contrast, previous studies have only allowed three-dimensional flow around the tip for lower aspect ratio foils. In addition, the present experiments are performed in a towing tank as opposed to a recirculating water channel. This has a small, but important effect, as experiments may be performed in ground-effect, very near the wall, *without the presence of an existing boundary layer* due to the incoming flow velocity. Finally, the present experiments cover a range of dynamically scaled parameters which encompass *high thrust regimes* typical of operational UUVs. As such, the results are the most directly applicable to the high aspect ratio foil propulsors that are currently employed on a number of existing biologically inspired UUVs, such as the Roboturtle [24] and the Razor platform [25].

1.2 Experimental Methods
1.2.1 Experimental Apparatus

The results reported below were obtained using an extruded aluminum NACA 0012 foil with a chord length of 0.07 m (Vortech Inc. Aluminum NACA 0012 Tail Rotor Kit). The foil is rigidly mounted to a 6-axis strain gauge dynamometer (factory-calibrated ATI Gamma SI-65-15) on a towing carriage above the free surface of a 0.9 m × 0.9 m × 4.3 m glass walled tank. The carriage is pulled down

the length of the tank by a chain drive attached to a stationary motor. A linear actuator mounted to the moving carriage generates horizontal ('heave') motion perpendicular to the direction of carriage travel. A rotary actuator mounted to the output of the linear actuator generates twist ('pitch') motion about an axis normal to the free surface. A rigid false wall was installed on one side of the tank, reducing the channel width to 0.84 m, to allow the linear actuator to bring the foil to within 0.01 m of the wall. The dynamometer and foil are mounted to the output of the rotary motor such that the foil is rotated about an axis located $\frac{1}{3}$ of the chord length from the leading edge. The span (length) of the foil was varied to allow testing for cases where the foil spans the entire flow channel, and for cases where the foil ends in the middle of the tank. Figure 1 shows a rendering of the experimental apparatus with the major components indicated in the figure.
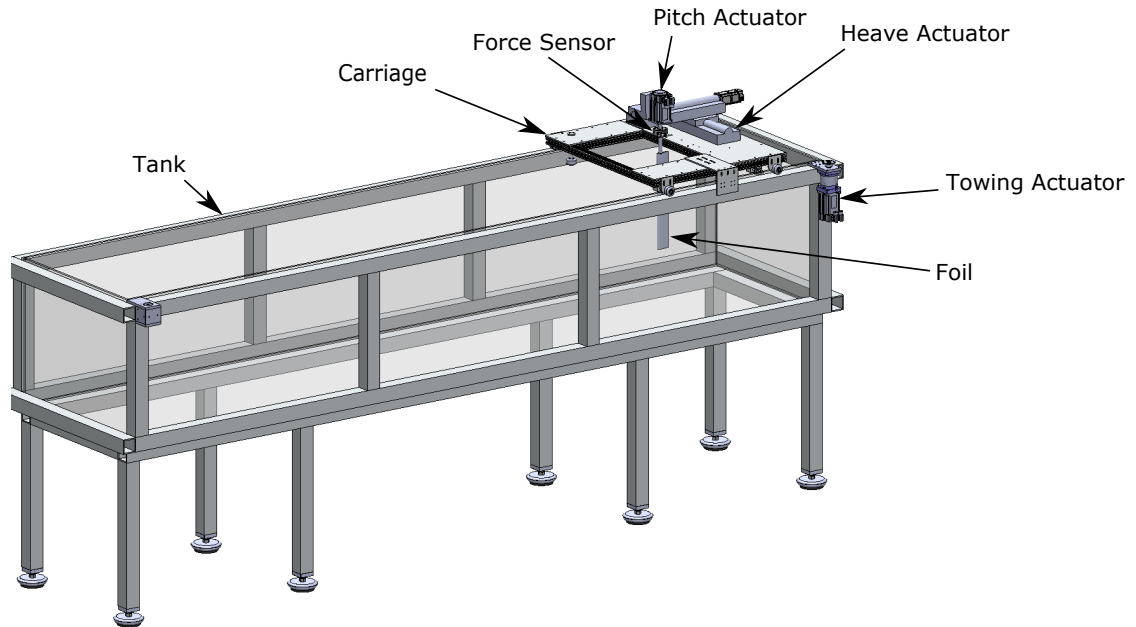
Figure 1: Rendering of the towing tank and carriage apparatus used in experiments. The force sensor is connected between the pitch actuator and the foil. Drawing shows the heave and pitch actuators along with the carriage and tank. In the drawing, the test foil is suspended from the carriage such that the foil tip is not near the tank bottom.

1.2.2 Foil Kinematics

All tests were performed with the foil undergoing sinusoidal pitch oscillations and with the foil heave velocity constrained to generate sinusoidal oscillations in the nominal angle of attack. Following Licht et al. [26], kinematics that generate a sinusoidal angle of attack were chosen over kinematics that use sinusoidal pitch and heave trajectories, despite the added computational complexity. Read et al.[27] demonstrated that this approach achieves higher thrust and efficiency in high aspect ratio oscillating foils across the entire parameter space investigated in the present study.

Following the notation detailed in Figure 2, the kinematic and geometric parameters governing the motion of the foil to be varied are shown in Table 2.

Table 2: List of Geometric and Kinematic Parameters

Heave amplitude	h_0
Pitch amplitude	θ_0
Angle of attack amplitude	α_0
Oscillation frequency	ω
Mean heave position	H
Tip distance	d
Carriage velocity	U

Given these parameters and the two kinematic constraints, the foil motion is then fully defined by five equations. The desired kinematics are described by:

$$\theta(t) = \theta_0 \sin(\omega t) \tag{1}$$

$$\alpha(t) = \alpha_0 \sin(\omega t) \tag{2}$$

Equations (1)-(2) impose sinusoidal constraints on the pitch angle and the nominal angle of attack.

The nominal angle of attack is defined by the pitch angle and the instantaneous velocity of the foil through the water. Where the instantaneous velocity of the foil is decomposed into U and $\dot{h}$ components, the result is:

$$\alpha(t) = \theta_0(t) - \arctan(\frac{\dot{h}(t)}{U}) \tag{3}$$

The instantaneous heave position at time t can be calculated by integrating heave velocity from time 0 up to time t:

$$h(t) = H + \int_0^t \dot{h}(t)\,\mathrm{d}t \tag{4}$$

Finally, the kinematics must satisfy the desired maximum heave excursion:

$$h^{\mathrm{max}} - h^{\mathrm{min}} = h_0 \tag{5}$$

For any set of parameters $(\alpha_0, \omega, H, h_0, U)$, $h(t)$ is implicitly defined by Equations (1) - (5). The iterative process described in Licht et al.[26] was used to determine the value of the constant θ_0 which produces the desired maximum heave excursion, h_0, while still satisfying the trajectory constraints on $\theta(t)$ and $\alpha(t)$.

To generalize the problem, results are presented as a function of non-dimensional parameters based on the kinematics, geometry, and fluid properties, as listed in Table 3.

Table 3: List of Non-Dimensional Parameters and Experimental Values

Reynolds number	$Re = \frac{Uc}{\nu}$	2.10×10^4
Strouhal number	$St = \frac{h_o f}{U}$	$[0.3, 0.35, 0.4, 0.45, 0.5]$
Maximum nominal angle of attack	α_o	$[15, 20, 25, 30, 35, 40, 45]$
Heave amplitude to chord length	$h^* = \frac{h_o}{c}$	1
Mean heave distance to chord length	$H^* = \frac{\bar{h}}{c}$	$[1.33, 1.66, 2, 3, 4, 5, 6]$
Tip clearance to chord length	$d^* = \frac{d}{c}$	$[0.029, 0.74]$

1.2.3 Experimental Procedure

Experiments were performed for varying wall distance, Strouhal number, and maximum angle of attack. Non-dimensional wall distances of $H^* = [1.33, 1.66, 2, 3, 4, 5, 6]$ represent the full range from the closest safe wall approach in the experimental setup to the center of the flow channel. The maximum angle of attack, α_o, ranged from 15 to 45 degrees in 5 degree steps, and Strouhal number ranged from 0.3 to 0.5 in steps of 0.05. The selected range of St was constrained by limitations of the experimental apparatus and force measurement equipment. For high St, corresponding to higher frequency motions, the acceleration of the trailing edge of the foil at the free surface produces strong vortices that may entrain air. The upper limit of St was selected to avoid this air entrainment in the wake. The lower limit of St was selected based on the resolution of the force sensor. At lower frequencies, the dynamic variation of hydrodynamic forces is small compared to the inertia of the test foil. Since the hydrodynamic force is determined as a difference between the measured total force and inertial force of the foil, increased uncertainty exists in the measurement of hydrodynamic forces at low frequencies and low speeds. The lower limit of St was selected to ensure measurable hydrodynamic forces with the particular experimental setup. For all dynamic motion tests, the non-dimensional heave amplitude was held at $h^* = 1$. Figure 2 shows a schematic trajectory of the foil relative to the wall.

Two sets of experiments were performed in order to isolate the effects of spanwise flow around the tip of the foil. In the first set of experiments, nominally two dimensional flow was investigated with an average tip clearance, $d = 2$ mm, such that $d^* < 0.029$. In the second set of experiments, three dimensional flow was investigated with the average tip clearance distance set at 52 mm, such that $d^* = 0.74$, allowing significant spanwise flow around the tip of the foil. The tip

distance, d, is illustrated in Figure 2. The submerged span was held constant at $s = 0.343$ m by varying the water depth, D, from 0.345 m to 0.395 m for $d = 2$ mm and $d = 52$ mm, respectively.

In all cases, the towing velocity was set to $U = 0.3$ m/s, resulting in the chord based Reynolds number $Re = 2.10 \times 10^4$. At the center of the flow channel, where $H^* = 6$, the foil was considered to be in the 'far-field' with no ground induced asymmetry in the lift force present. In order to align the mean foil pitch angle with carriage travel direction, a series of tests was performed at $H^* = 6$, where the foil was towed with static angles of attack varied at increments of 1 degree. Zero pitch angle was chosen as the static angle of attack where the minimum absolute value of mean drag was recorded and mean lift was observed to be zero. A nine minute tank settling interval was allowed between tests, following validation experiments indicating that a six minute settling interval was sufficient to avoid measurable interference between experiments. This observation was made by varying the tank settling time for a series of repeated motion experiments with $St = 0.4$ and $\alpha_0 = 30$. Confidence in the repeatability in the measurement of forces was obtained by repeating the same experiment 30 times with $St = 0.4$, $\alpha_0 = 30$, and $H^* = 6$. It was found that the mean lift coefficient had a standard deviation of 0.0034.

1.2.4 Analysis Procedure

Results are presented in terms of lift coefficient, thrust coefficient, and efficiency. The instantaneous lift and thrust coefficients, C_L and C_T, respectively, are given by:

$$C_T = \frac{F_x}{0.5\rho U^2 A} \tag{6}$$

$$C_L = \frac{F_y}{0.5\rho U^2 A} \tag{7}$$

where ρ is the fluid density, and $A = sc$ is the planform area of the submerged

(a)

(b)
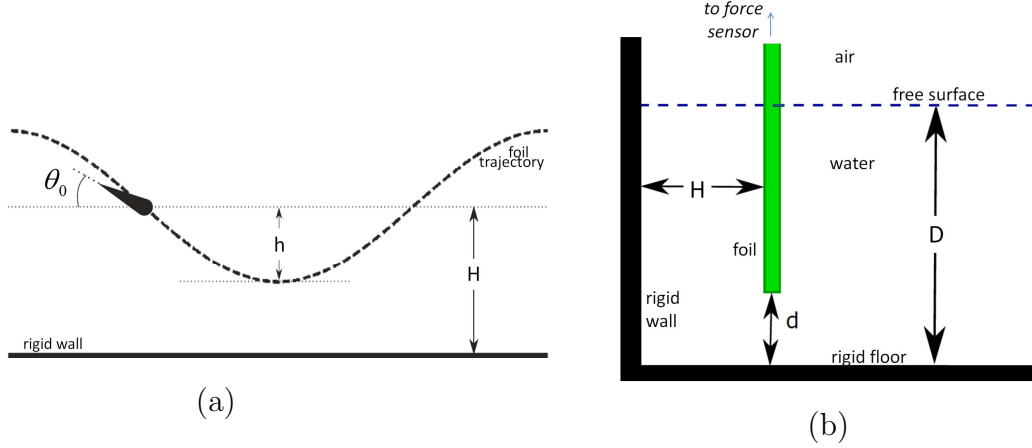
Figure 2: (a) Top view of foil trajectory. h is the maximum heave excursion from the mean heave position, H, where heave position is measured from the wall. θ_0, the maximum pitch angle, is achieved where the foil crosses the mean heave position. $\theta = 0$ at the maximum and minimum heave excursion. (b) Rear view of foil in mean heave position. The tip clearance between the foil and the bottom of the tank is denoted as d, while the depth of the water is $D = s + d$. Experiments were performed with $(d, D) = (0.002, 0.345)\ m$ and $(d, D) = (0.052, 0.395)\ m$.

foil found using the submerged span, s, and chord length c. F_x is the instantaneous measured force in the direction of carriage travel. F_y is the instantaneous measured force perpendicular to the direction of carriage travel.

Mean thrust and lift coefficients are reported based on data from whole motion cycles, i.e.:

$$\bar{C}_T = \frac{\int_0^{nT} C_T(t)\, \mathrm{d}t}{nT} \tag{8}$$

$$\bar{C}_L = \frac{\int_0^{nT} C_L(t)\, \mathrm{d}t}{nT} \tag{9}$$

where T is the cycle period given by $T = \frac{2\pi}{\omega}$.

The hydrodynamic efficiency is the ratio of extracted power to the input power over whole cycles, where input and output power are calculated using measured foil speed, force, and torque:

$$\eta = \frac{P_{OUT}}{P_{IN}} = \frac{\int_0^{nT} U F_x(t)\,\mathrm{d}t}{\int_0^{nT} \dot{h}(t)F_y(t) + \dot{\theta}(t)M_\theta(t)\,\mathrm{d}t} \tag{10}$$

where M_θ is the measured torque about the foil rotational axis. For each set

of $(St, \frac{H_o}{c}, \alpha_o)$ values, the reported values for mean non-dimensional outputs were

calculated based on five cycles of motions, i.e. $n = 5$ in Eqn. 6-10. Data from

the first two oscillations after the start of motion in each test run are not included

in any analysis, in order to eliminate the effect of start up transients. Based on

cycle-to-cycle comparison, the transient effects disappear after approximately one

full cycle of motion.

Where instantaneous values of C_L and C_T are reported, they are based on the

ensemble averaged values from those five cycles.

1.3   Results

Detailed results are presented only for a tip clearance to chord length ratio,

d^*, equal to 0.74, which corresponds to the foil tip suspended near the middle of

the tank, far from the bottom, allowing for an unhindered three-dimensional flow

around the foil tip.

1.3.1   Comparison of Near-Wall and Free-Stream Results

As a first indicator for the presence of ground effect, the mean thrust, mean

lift, and efficiency is compared for when the foil is close to the ground ($H^* = 1.33$),

and when the foil is in the free stream far from the wall ($H^* = 6$). Figure 3(a) shows

the mean thrust coefficient measured for all kinematics tested; differences in mean

lift, thrust, and efficiency between the free-stream and at the closest approach to

the wall for identical kinematics are shown in Figure 3(b)-(c). The contours of

mean thrust are consistent with the results presented in Anderson et al.[28] and

Read er al. [27] for flapping foil thrust production with harmonic oscillation and
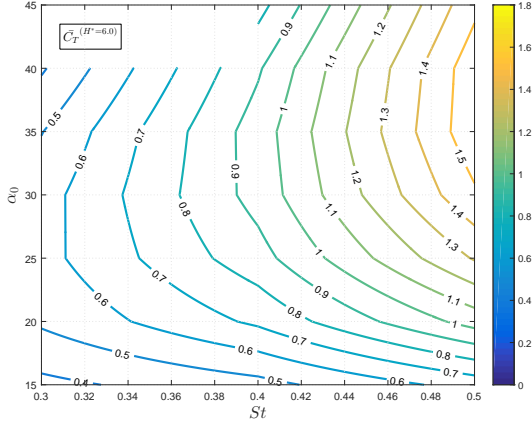
(a) Thrust Coefficient, $\bar{C}_T$
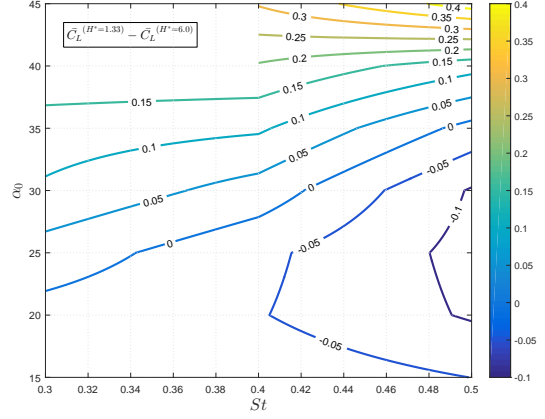
(b) Lift Coefficient Change $\Delta\bar{C}_L$
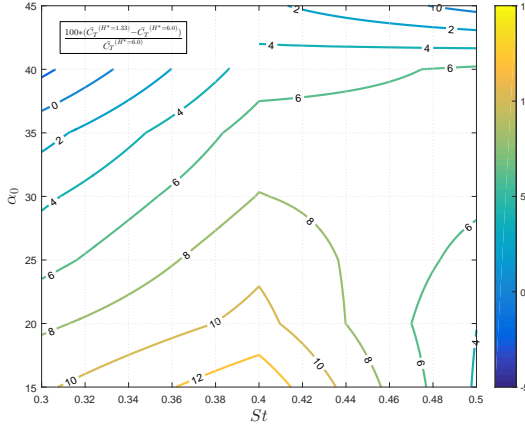
(c) Thrust Change, $\Delta\bar{C}_T$ [%]
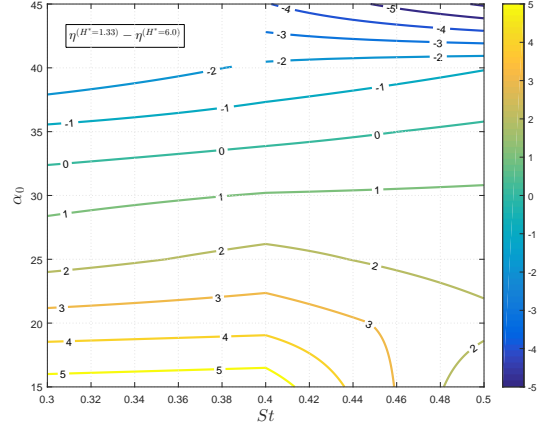
(d) Efficiency Change, $\Delta\eta$ [%]

Figure 3: (a) Mean thrust coefficient when operating at the closest approach to the wall, $H^* = 1.33$. (b)-(d) Differences in the lift coefficient, the magnitude of the thrust force, and the efficiency when the foil is operating at the closest approach to the wall ($H^* = 1.33$) vs. operation in the free stream ($H^* = 6.0$). Thrust changes range from 0% to 12%. Efficiency changes range over $\pm 6\%$. $\Delta\bar{C}_L$ ranges from -0.1 to 0.4.

14

sinusoidal angle of attack. The thrust gradient is positive with increasing St, with a ridge of optimal thrust running along $25° < \alpha_0 < 35°$ for the range of St tested.

Consistent with Blevins and Lauder [15] and Fernandez-Prats et al. [12], thrust increases in the presence of the wall for almost all cases studied (Figure 38e). Efficiency changes are small and not uniformly positive (Figure 38f), similar to observations by Quinn et al. [14], with changes in η ranging over $\pm 6\%$. Large mean lift forces are observed, which act to push the foil away from the wall, i.e. a ground cushion exists in the traditional sense of fixed foil ground effect. This ground effect is observed primarily for higher α_0 over the range of St (Figure 38b). The maximum angle of attack plays a critical role in the orientation of the lift force, and for smaller α_0, a transition occurs where the mean lift demonstrates a suction towards the wall, largely at the higher St values. The areas of increased efficiency and near zero or negative lift overlap over a large region of the studied parameters, implying that there is a trade-off between increased efficiency and the presence of a stabilizing ground effect. This is despite the fact that absolute thrust is increased for almost all kinematics when the foil is oscillated in close proximity to the wall.

1.3.2   Nonlinear Evolution of Forces as Foil Approaches the Wall

The direct comparison between the closest approach and the free stream case illustrates a net ground effect in unsteady flow. However a finer variation of H^* is necessary to show the evolution of the mean forces as the mean position of the foil is moved closer to the wall with the dynamic motion of the foil otherwise unchanged. The effect of this decrease in the mean position relative to the wall on the mean forces exerted on the foil is very non-linear.

The most dramatic changes in the forces exerted on the foil occur almost entirely within a very small region of H^*, where the foil comes very close to the

(a) $\bar{C}_T$ vs. H^*, $St = 0.4$

(b) $\bar{C}_L$ vs. H^*, $St = 0.4$
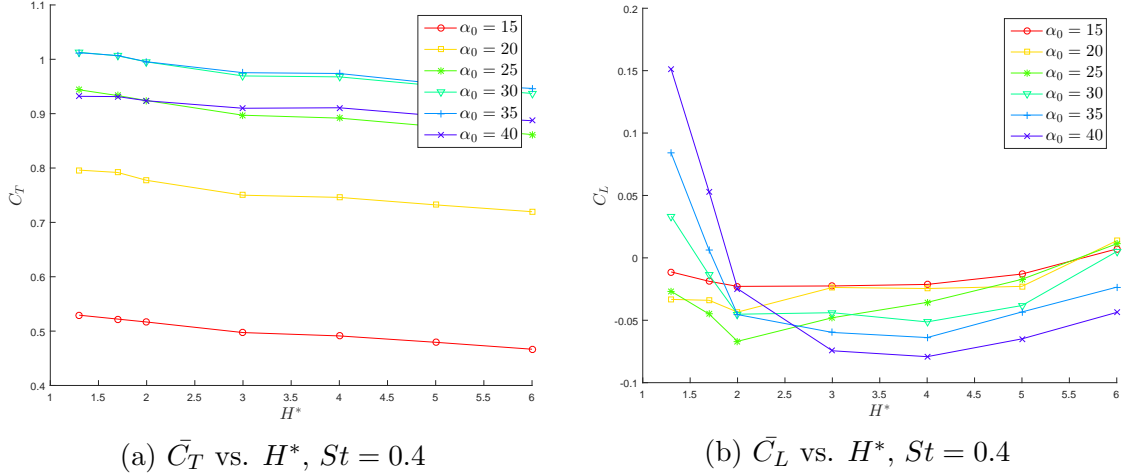
Figure 4: The evolution of (a) mean thrust coefficient, $\bar{C}_T$, and (b) mean lift coefficient, $\bar{C}_L$), as the foil distance to the wall decreases from $\frac{H}{c} = 6$ to $\frac{H}{c} = 1.33$, for the representative case where $St = 0.4$. Each curve represents a different value of the nominal angle of attack, α_0, with higher α_0 producing a plunging motion with less feathering, and lower α_0 producing a more feathered motion with high pitch amplitudes.

wall. This effect is illustrated in Figure 4, which shows mean lift and thrust as functions of the mean wall distance (H^*) for a fixed Strouhal number of 0.4 and fixed non-dimensional heave amplitude of $h^* = 1$. Separate curves are given for each increment of maximum angle of attack.

The proximity of the flapping foil to the solid wall clearly has a strongly non-linear effect on mean lift. As shown in Figure 4b, both the magnitude and the sign of the lift force vary with distance to the wall. Far from the wall, at $H^* = 6$, the mean lift over the cycle is near zero. When the foil trajectory is first moved closer to the wall ($6 > H^* > 3$), the mean lift gradually decreases, indicating a slight suction towards the wall. The suction force is experienced regardless of the maximum angle of attack. However, as the foil approaches the wall more closely, i.e for $H^* < 3$ the maximum angle of attack plays a critical role in the magnitude of the lift that develops. At low angles of attack, the foil continues to experience a slight but lessening suction force even at the closest approach. However, when

16

$\alpha_0 > 25°$ a strong repelling force develops at the closest approaches to the wall, with $\bar{C}_L$ reaching a maximum 0.15 for the most extreme cases ($\alpha_0 = 40°$).

The mean lift effects shown in Figure 4b are illustrative of the phenomenon at other Strouhal numbers, where the magnitude of mean lift may change slightly, but the general trend of a mean repelling force at high angle of attack is still seen. The suction force far from the wall and reversal to a repelling force near the wall is consistent with ground effect observations for a fixed wing near a wall, and with observations by Quinn et al. [13], where a zero lift equilibrium may be achieved near the wall. In the fixed foil case, the foil is pushed away from the wall if it moves closer, and pulled back towards the wall if it moves further away. In the flapping foil case in this study, at $St = 0.4$, this stable equilibrium point is only reached for $\alpha_0 > 25°$, where the closest foil approach was limited to $\frac{c}{3}$.

In addition to a change in average lift, the cycle averaged thrust force displays uniformly positive changes as H^* decreases. Figure 4a shows the cycle averaged thrust for the same representative case of fixed Strouhal number 0.4 and $h^* = 1$. The time averaged thrust coefficient, $\bar{C}_T$, gradually increases as the foil gets closer to the wall for all maximum angles of attack. This change is nearly the same in magnitude regardless of angle of attack, ranging from a difference in $\bar{C}_T$ between the near wall ($H^* = 1.33$) and far wall ($H^* = 6$) trajectories of 0.05 to 0.08 depending on the specific angle of attack. The maximum relative change ranges from 13% (from $\bar{C}_T = 0.47$ to 0.53) at $\alpha_0 = 15°$ to 4% (from $\bar{C}_T = 0.89$ to 0.93) for $\alpha_0 = 40°$, the least aggressive and most aggressive plunging motions, respectively. An 8% increase (from 0.94 to 1.01) occurs for the maximum thrust producing condition where $\alpha_0 = 30°$.

1.3.3 Evolution of Characteristic Force Vector as Foil Approaches the Wall

To better illustrate the average vector change in force based on the foil proximity to the wall, the magnitude and direction of the characteristic force coefficient vector may be defined as:

$$\bar{C}_A = \sqrt{\bar{C}_T{}^2 + \bar{C}_L{}^2} \tag{11}$$

$$\gamma(St, \alpha_0, H^*) = \tan^{-1}\left(\frac{\bar{C}_L}{\bar{C}_T}\right) \tag{12}$$

Figure 5 recasts the results in Figure 4, showing C_T on the horizontal and C_L on the vertical axis. The mean force magnitude, $\bar{C}_A$, and characteristic force angle relative to the wall, γ, are shown for a reference case where $(St, h^*, \alpha_0) = (0.4, 1.33, 40°)$.) A positive value of γ indicates that the mean force is angled away from the wall (a repelling force,) and negative values indicate a suction force towards the wall. Figure 5 highlights the dependence of ground effect on α_0, where each curve follows the total force vector for a single value of α_0 as the foil's mean trajectory is moved from the far-field into ground effect near the wall. Both the magnitude and direction of the mean force change as the foil comes closer to the wall. It is apparent that the direction of these changes are most dramatic for high angle of attack 'plunging' motions, rather than low angle of attack 'feathered' motions.

Figure 6 shows the evolution of the characteristic force angle as the foil approaches the wall at three different St numbers. The ground induced lift is much more significant at low St numbers; for $(St, \alpha_0) = (0.3, 40°)$ the mean force is directed away from the wall at an angle of 19.0°, while for $(St, \alpha_0) = (0.5, 40°)$ the maximum characteristic angle is only 4.8°. This sensitivity to St number is not evident for very low angles of attack, i.e. $\alpha_0 < 25°$.
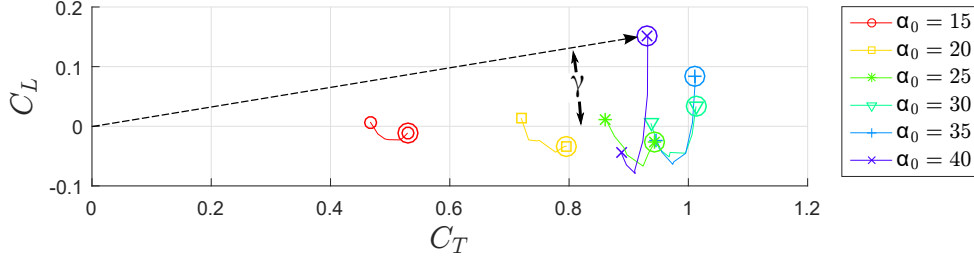
Figure 5: The evolution of total force vector $(\bar{C}_T, \bar{C}_L)$ for $St = 0.4$ as the foil distance to the wall decreases from $\frac{H}{c} = 6$ to $\frac{H}{c} = 1.33$. Each curve represents a different value for α_0. The circled point in each case is the closest approach to the wall $(\frac{H}{c} = 1.33)$. The direction of the mean force is captured in the angle $\gamma = \gamma(St, \alpha_0, \frac{H}{c})$, a function of kinematics and distance to the wall. γ is shown above for $(St, \alpha_0, \frac{H}{c}) = (0.4, 40°, 1.33)$

1.3.4 Ground effect in instantaneous thrust and lift throughout motion cycle.

The previous results show changes in mean thrust and mean lift averaged over several oscillatory cycles of motion. Unlike fixed wings, where the flow field and forcing is nominally steady, the instantaneous force experienced by the oscillatory wing varies significantly throughout the period of motion. Figure 7 shows the phase averaged instantaneous forces for the cycle of motion experienced by the foil near the wall superimposed on the foil trajectory. Results are shown for nine different cases with $\alpha_0 = (30°, 40°, 50°)$ and $St = (0.3, 0.4, 0.5)$, spanning the full range of kinematics parameters tested. The nine separate cases are marked as A-I for reference on Figure 9.

As in previous work related to the forces on propulsive flapping foils [29, 26, 11], very large and opposing peak lift forces are experienced during the upstroke

19
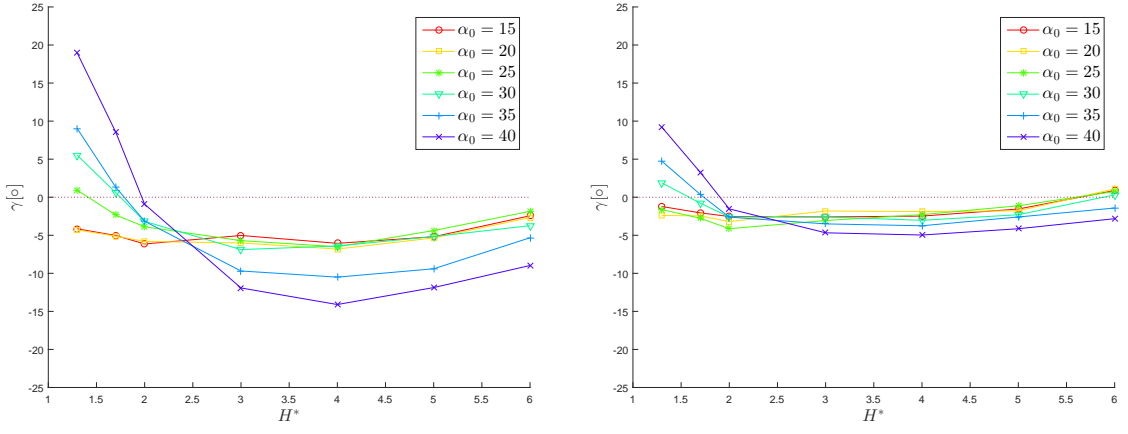
(a) γ vs. H^*, $St = 0.3$

(b) γ vs. H^*, $St = 0.4$
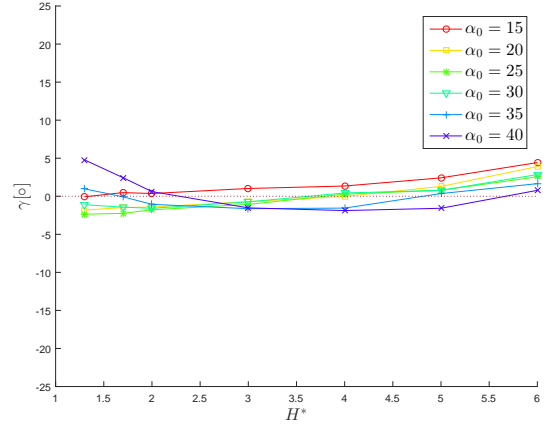
(c) γ vs. H^*, $St = 0.5$

Figure 6: The evolution of γ, the direction of the mean force, as the foil distance to the wall decreases from $\frac{H}{c} = 6$ to $\frac{H}{c} = 1.33$. Results are shown for $St = [0.3, 0.4, 0.5]$.
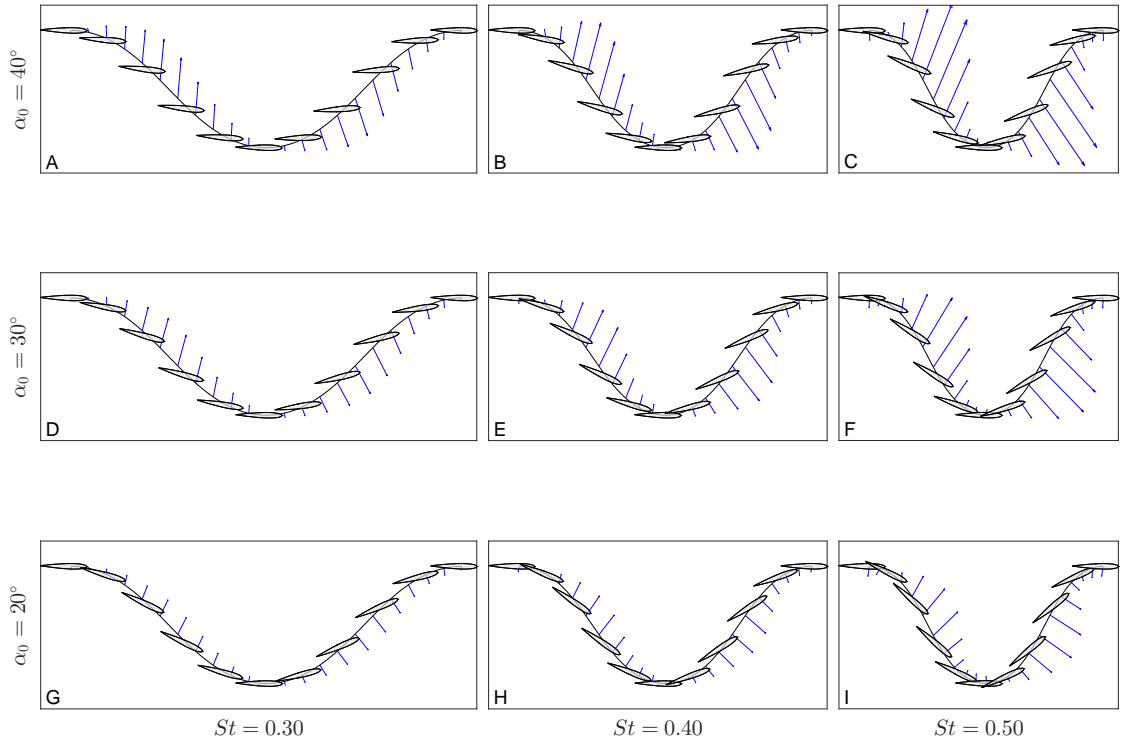
Figure 7: Instantaneous force vectors, (C_T, C_L), superimposed over foil position tracks for nine different cases with $\alpha_0 = (30°, 40°, 50°)$ and $St = (0.3, 0.4, 0.5)$, near wall condition, $\frac{H}{c} = 1.33$. (Cases A-I correspond to parameters values marked on Figure 9.)
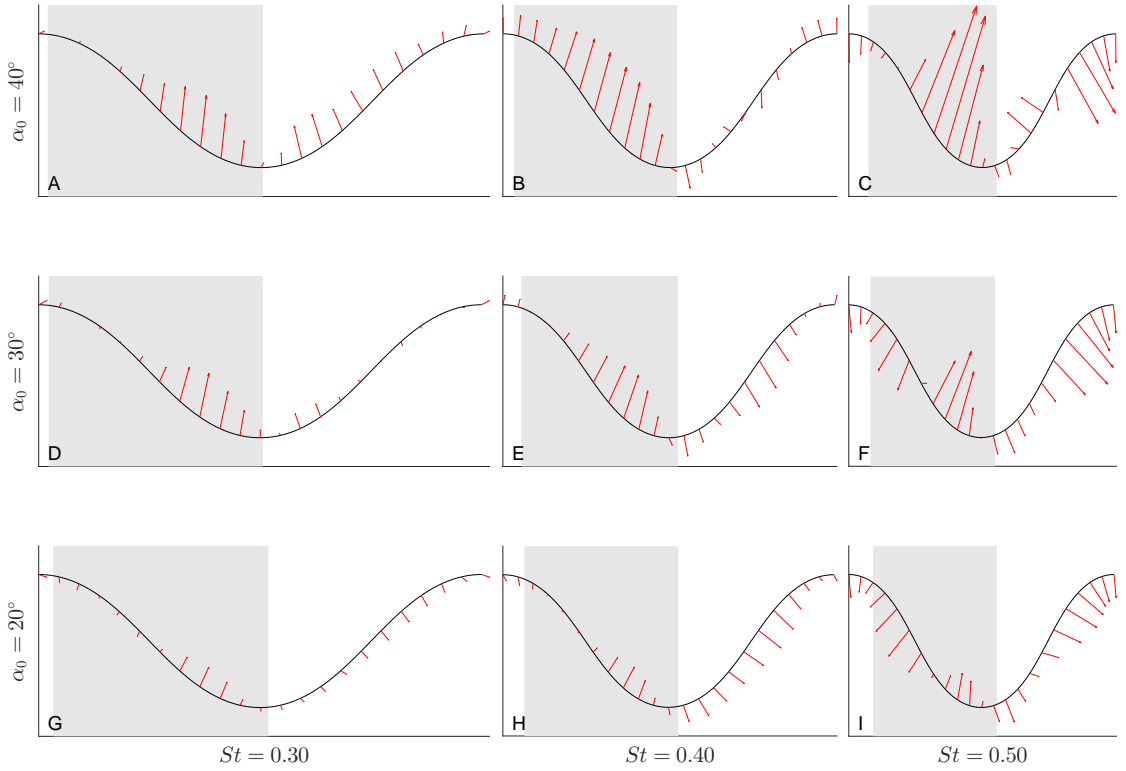
Figure 8: *Difference* in the instantaneous force vectors between $\frac{H}{c} = 1.33$ to $\frac{H}{c} = 6$. The vectors $(\Delta C_T, \Delta C_L)$ are superimposed over foil position tracks for nine different cases with $\alpha_0 = (30°, 40°, 50°)$ and $St = (0.3, 0.4, 0.5)$. Shading indicates cycle phase during which the total instantaneous lift force is positive (directed away from the wall.) Note that the vector magnitude scaling factor is different from that of Figure 7. (Cases A-I correspond to parameters values marked on Figure 9.)

and downstroke, with net thrust generated due to the slight forward angle of the net force during both upstroke and downstroke. The peak lift forces are very high relative to the mean thrust force, and very high relative to the mean ground effect in thrust and lift, making it difficult to distinguish differences in the instantaneous force between individual $\frac{H}{c}$ positions. In order to isolate and visualize the wall effect in the instantaneous force, the *difference* in instantaneous lift and thrust force is shown in Figure 8.

The difference is computed for instantaneous force vectors between the near-wall ($\frac{H}{c} = 1.33$) and far-field ($\frac{H}{c} = 6$) cases. Thus an upward pointing vector indicates an increase in repelling force due to proximity to the wall. The shaded regions in the figure indicate phases in the cycle where the total instantaneous lift force in the near-field experiment is positive, resulting in a net repelling force away from the wall, while the unshaded region indicates where the total lift force is negative, resulting in a net suction force towards the wall. The vectors show the change in the magnitude and direction of the total force resulting from moving the foil trajectory near the wall. In a shaded region, if the change in force points upward, the instantaneous lift is enhanced, resulting in an increased repelling force from the wall. If the vector points downward in the shaded region, there is still a net repelling force, but the force magnitude is reduced by the presence of the wall. A similar argument holds for the net suction regions, where an upward pointing arrow corresponds to a decrease in suction and a downward pointing arrow corresponds to an increase in suction. This interaction is complex and dependent on the phase of a particular motion. For example, in Case B, upward pointing vectors in nearly all of the shaded region indicates that the cycle dependent repelling force is enhanced throughout the cycle, although there is some loss in suction at the peak of the motion, where the total lift force is very small. As another example, Case A shows

difference vectors that point upward throughout the cycle of motion, while the shaded region indicates a net repelling during the first half of the cycle and a net suction during the second half of the cycle. For this condition, the repelling force is consistently amplified in the downstroke, while the suction force is consistently reduced in the upstroke.

The observed difference in instantaneous force vectors over the cycle also helps to illustrate the presence of a cycle averaged mean repelling force or suction. Where the lift force changes more on the downstroke (e.g. Case B) there is a net force away from the wall, and where the lift changes more on the upstroke (e.g. Case H) there is a net suction force towards the wall. Where these opposing changes in the lift force are of nearly equal magnitude (e.g. Case E) there is minimal change in the mean lift force ($\gamma \approx 0$), indicating that a ground effect can be present even when no net cycle averaged change is found.

1.4 Discussion

The dynamic forces associated with a flapping foil in proximity with a wall are inherently different than the case of a static wing near the wall due to the constantly changing distance between the foil and the wall. This dynamic motion results in a very different flow field, altering both time averaged mean forces and phase averaged instantaneous forces acting on the wing. In the context of a maneuvering body using foils for propulsion in the presence of a solid boundary, these effects may be utilized to detect the presence of a wall, and to provide altitude stabilization. General observations from the present experiments are made which may be understood in the context of potential applications. In the presence of a wall, the present experiments show:

- Time averaged mean forces are insufficient indicators of the presence of ground effect.

- Foil kinematics may be adjusted to modulate the strength of ground effect for any achievable thrust level.

- Increased hydrodynamic efficiency in the presence of the solid boundary is inversely correlated to the strength of repulsion caused by ground effect.

- Ground effect is an inherently three-dimensional phenomenon, even for unsteady, dynamic flows.

1.4.1 Mean force results are insufficient indicators for the presence of ground effect.

In a steady flow, time averaging of the fluid force is commonly used as a method to simplify the characterization of the fluid dynamics, such as in the definition of a drag coefficient or lift coefficient. In periodic dynamic processes, such as a propulsive flapping foil, mean thrust and mean lift may be used for general maneuvering purposes, allowing for these types of forces to be built into a dynamic model for a particular vehicle. When a bias angle [30] is used in flapping foil propulsion, the bias of the pitching angle introduces an asymmetry in the flow field which can provide a reproducible offset to the mean lift force and adjustment to the mean thrust force, leading to time averaged maneuvering forces.

The presence of the wall in the present experiments also introduces an asymmetry to the flow field, however this asymmetry does not always result in a non-zero mean lift. As seen in Figure 8, the presence of the wall has a strong impact on the instantaneous forces acting on the foil, however the time averaged mean lift may not be significantly changed. This effect is both a function of Strouhal number and of the maximum angle of attack, hence it is necessary to to evaluate the orientation of the wake in order to further understand this lack of a mean bias despite the presence of flow asymmetry. Since the mean force is an unreliable indicator of the presence of ground effect, the mean force should not be used alone as a mechanism
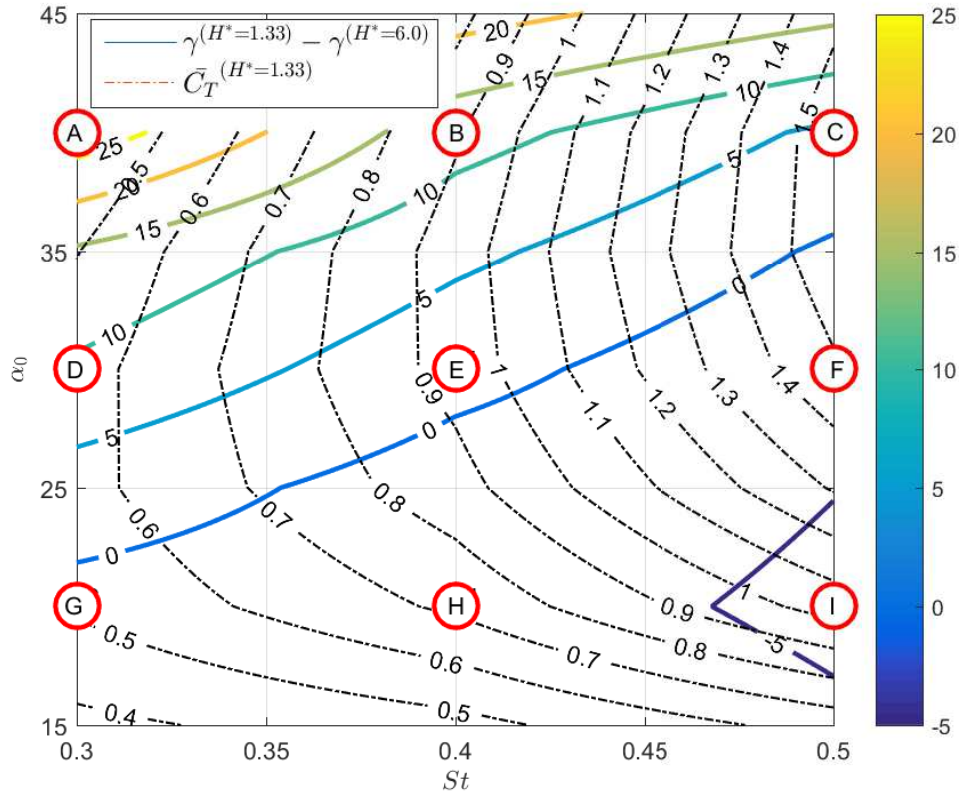
Figure 9: Contours of characteristic angle of force near the wall are overlaid on contours of thrust coefficient. All thrust contours are positive. Positive characteristic angles represent a mean force pushing the foil away from the wall, negative angles represent a mean force pulling the foil in towards the wall.

for wall or bottom sensing and phase dependent forces may be more relevant in a wall sensing application.

1.4.2 Foil kinematics can be adjusted to modulate the strength of the ground effect for any achievable thrust level.

Using the characteristic force angle, one can directly compare results across all cases, despite the widely varying force magnitudes, as in Figure 9, where contours of angle at the closest approach to the wall are superimposed over contours of mean thrust for all kinematics investigated. The contours of thrust and the contours of characteristic force angle are nearly perpendicular for all kinematics with positive

deflection, i.e. wherever the ground effect tends to repel the foil from the solid boundary. Using the deflection angle of the mean force as a proxy for the 'strength' of the ground effect, one may independently select the amount of thrust and the strength of ground effect simply by varying foil kinematics.

This is especially significant from the perspective of an animal or a man-made vehicle attempting to operate near a solid boundary. The mean thrust generated through flapping correlates with mean vehicle speed in a viscous medium. A positive ground effect implies that there will exist some distance away from the wall at which the vehicle is in a stable equilibrium. The strength of the ground effect will be correlated with increased stability of that equilibrium. Thus, given the independence of thrust magnitude and ground effect strength, kinematics can be chosen at any speed to enhance stability and provide a passive ground avoidance mechanism.

The passive (i.e. not explicitly actuated) nature of this ground avoidance mechanism is critical for cases where accurately sensing the distance to the bottom is difficult or impossible; it also increases the viability of simplified control schemes where the kinematics may only be adjusted at discrete phases within the stroke, as in e.g. [24].

1.4.3 Increased hydrodynamic efficiency in the presence of the solid boundary is inversely correlated the strength of repulsion caused by ground effect.

A comparison of Figure 38b and Figure 38f makes it clear that increases in propulsive efficiency, which occur only at angles of attack below 35° are generally associated with a negative mean lift coefficient. A $> 10\%$ increase in thrust coefficient at $(St, \alpha_0) = (0.4, 25°)$ results in nearly 4% efficiency improvement. However, this comes at the cost of incurring a suction force on the foil, pulling it in towards the wall.

There is a narrow range of α_0 in which a positive ground effect occurs without efficiency loss. For lower St, lower thrust conditions, a positive 10° deflection of the force vector can be achieved with zero efficiency change, by choosing $\alpha_0 = 30°$. As St number and thrust coefficient increase, the maximum positive deflection of the force vector that can be achieved is reduced. For the most aggressive kinematics tested, $St = 0.5$, net zero change in efficiency corresponds to net zero change in force vector. This implies that increased efficiency can only be achieved by incurring suction force, or that the benefits of a positive ground effect can only be achieved at the expense of reduced efficiency.

1.4.4 Ground effect as an inherently three-dimensional flow phenomena.

Previous studies with high-aspect ratio foils, both numerical [21, 17] and experimental [13], have considered a two-dimensional representation of the problem of wall interaction. Ground effect is fundamentally different in a two-dimensional flow field compared with a three-dimensional flow field, as the three-dimensional flow around the tip of the foil plays a critical role in determining the direction of lift experienced by the foil. For a three-dimensional foil geometry with relatively low aspect ratio, flow forced around the tip in the presence of the ground may generate increased suction on the upper side of the foil resulting in a repelling force in the presence of the ground. In contrast, a two-dimensional flow cannot exhibit this out of plane flow around the tip, hence the presence of the ground may result in accelerated flow below the foil, leading to an increased suction on the underside of the foil and an attraction force towards the wall. This conceptual simplification is not perfect for all flow conditions, but illustrates some of the inherent differences between a 3-D and 2-D foil experiencing effects from proximity to the ground.

Experiments were performed in which the same foil was oscillated with its tip
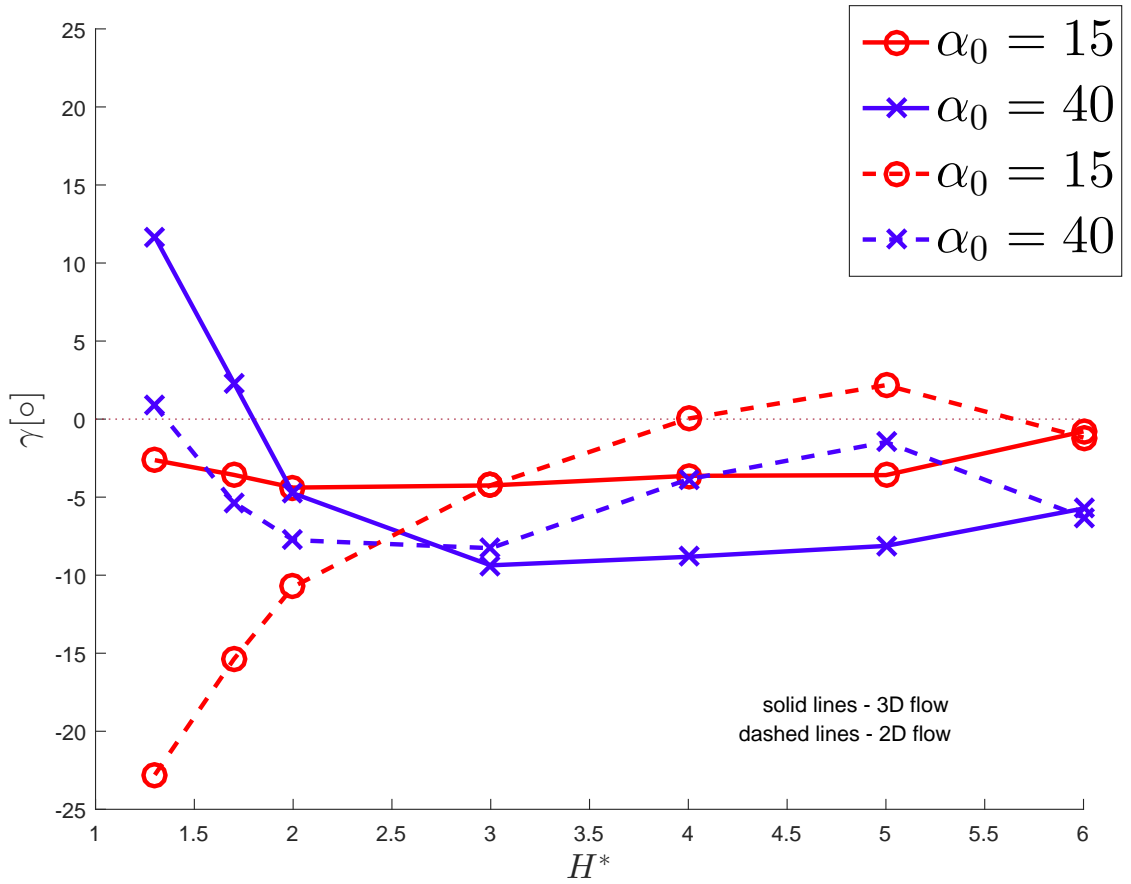
Figure 10: The evolution of γ, the direction of the mean force, as the foil distance to the wall decreases from $\frac{H}{c} = 6$ to $\frac{H}{c} = 1.33$. Results are compared at $St = 0.35$ for the two dimensional (no flow allowed around foil tip) and three dimensional case.

very close to the tank bottom, approximating the 2-D condition and limiting flow around the tip. Figure 10 compares the two dimensional and three dimensional flow cases for $(St, \alpha_0) = (0.35, 15)$ and $(St, \alpha_0) = (0.35, 40)$. As the foil approaches the ground with high α_0, the ground effect is greatly reduced in the two dimensional case. With low α_0, a large suction force is experienced in the two dimensional case. These preliminary results suggest that fundamental differences can be observed between the two dimensional case with flow restriction at the tip and the three dimensional results presented in detail above. This difference is important for modeling of ground effect, as two-dimensional simulations on a flapping foil will incorrectly predict the resulting forces.

1.5 Conclusions

A detailed series of experiments were performed to study the effect of wall proximity on the forces exerted by the fluid on a propulsive flapping foil. The prescribed flapping foil motion followed a sinusoidal heave and sinusoidal angle of attack. The maximum angle of attack, mean distance from the wall, and Strouhal number of the motion were varied, while the amplitude of the motion was held constant. It was found that the mean distance from the wall has a significant impact on the measured mean lift and mean thrust acting on the foil, however the mean force is not always indicative of the presence of a wall. For a range of kinematics, the instantaneous force profile may change significantly, but in such a way that increases in the strength of repulsion on the downstroke and suction on the upstroke effectively cancel one another in the mean. Additionally, propulsive foil kinematics may be adjusted appropriately to modulate the strength of the ground effect without sacrificing thrust.

One important area of further research is an investigation of how span-wise flow around the tip of the foil affects these results. Preliminary results collected

at a few locations within the parameter space show that blocking span-wise flow on the foil may play an important role in reducing or even reversing the net effect of operating near a solid boundary. Future efforts are expected to include a comprehensive investigation of the effect of blocking the span-wise flow (i.e. approximating 2-D motion) across the same parameter space examined here in order to provide context to experimental and numerical results using 2-D fluid flow. In much of the literature, it appears that computational constraints make the inclusion of span-wise flow calculation unattractive, as this implies successfully simulating a three-dimensional fluid domain at high Reynolds numbers. Where numerical approaches struggle to add span-wise flow, experimental approaches struggle to eliminate span-wise flow if not desired. Three dimensional effects and span-wise flow will likely be present, and be significant, in real world applications of oscillating foils in ground effect, both for animals and UUVs. As a result, it is expected that experimental studies or computational studies incorporating a full three-dimensional flow field will be the more fruitful path towards understanding and quantifying ground effect in the near future.

List of References

[1] J. Gray, "Studies in Animal Locomotion VI. The Propulsive Powers of the Dolphin," *Journal of Experimental Biology*, vol. 13, no. 2, pp. 192–199, Apr. 1936.

[2] J. M. V. Rayner, "On the Aerodynamics of Animal Flight in Ground Effect," *Philosophical Transactions: Biological Sciences*, vol. 334, no. 1269, pp. 119–128, Oct. 1991.

[3] B. N. Nowroozi, J. A. Strother, J. M. Horton, A. P. Summers, and E. L. Brainerd, "Whole-body lift and ground effect during pectoral fin locomotion in the northern spearnose poacher (Agonopsis vulsa)," *Zoology (Jena, Germany)*, vol. 112, no. 5, pp. 393–402, 2009.

[4] H. Park and H. Choi, "Aerodynamic characteristics of flying fish in gliding flight," *The Journal of Experimental Biology*, vol. 213, no. 19, pp. 3269–3279, Oct. 2010.

[5] E. Cui and X. Zhang, *Ground Effect Aerodynamics, Encyclopedia of Aerospace Engineering.* John Wiley and Sons, Inc., 2015.

[6] M. S. Triantafyllou, A. H. Techet, and F. S. Hover, "Review of experimental work in biomimetic foils," *Oceanic Engineering, IEEE Journal of*, vol. 29, no. 3, pp. 585–594, 2004.

[7] O. M. Curet, N. A. Patankar, G. V. Lauder, and M. A. MacIver, "Mechanical properties of a bio-inspired robotic knifefish with an undulatory propulsor," *Bioinspiration & Biomimetics*, vol. 6, no. 2, p. 026004, June 2011.

[8] J. Tangorra, S. Davidson, P. Madden, G. Lauder, and I. Hunter, "A Biorobotic Pectoral Fin for Autonomous Undersea Vehicles," in *28th Annual International Conference of the IEEE Engineering in Medicine and Biology Society, 2006. EMBS '06*, 2006, pp. 2726–2729.

[9] T. I. Um, Z. Chen, and H. Bart-Smith, "A novel electroactive polymer buoyancy control device for bio-inspired underwater vehicles," in *Robotics and Automation (ICRA), 2011 IEEE International Conference on.* IEEE, 2011, pp. 172–177.

[10] J. H. Long, J. Schumacher, N. Livingston, and M. Kemp, "Four flippers or two? Tetrapodal swimming with an aquatic robot," *Bioinspiration & Biomimetics*, vol. 1, no. 1, pp. 20–29, Mar. 2006.

[11] A. H. Techet, "Propulsive performance of biologically inspired flapping foils at high Reynolds numbers," *Journal of Experimental Biology*, vol. 211, no. 2, pp. 274–279, Jan. 2008.

[12] R. Fernandez-Prats, V. Raspa, B. Thiria, F. Huera-Huarte, and R. Godoy-Diana, "Large-amplitude undulatory swimming near a wall," *Bioinspiration & Biomimetics*, vol. 10, no. 1, p. 016003, Feb. 2015.

[13] D. B. Quinn, K. W. Moored, P. A. Dewey, and A. J. Smits, "Unsteady propulsion near a solid boundary," *Journal of Fluid Mechanics*, vol. 742, pp. 152–170, Mar. 2014.

[14] D. B. Quinn, G. V. Lauder, and A. J. Smits, "Flexible propulsors in ground effect," *Bioinspiration & Biomimetics*, vol. 9, no. 3, p. 036008, Sept. 2014.

[15] E. Blevins and G. V. Lauder, "Swimming near the substrate: a simple robotic model of stingray locomotion," *Bioinspiration & Biomimetics*, vol. 8, no. 1, p. 016005, Mar. 2013.

[16] T. V. Truong, D. Byun, M. J. Kim, K. J. Yoon, and H. C. Park, "Aerodynamic forces and flow structures of the leading edge vortex on a flapping wing considering ground effect," *Bioinspiration & Biomimetics*, vol. 8, no. 3, p. 036007, Sept. 2013.

[17] H. Lu, K. B. Lua, T. T. Lim, and K. S. Yeo, "Ground effect on the aerodynamics of a two-dimensional oscillating airfoil," *Experiments in Fluids*, vol. 55, no. 7, pp. 1–15, July 2014.

[18] H. Liang, X. Wang, L. Zou, and Z. Zong, "Numerical study of two-dimensional heaving airfoils in ground effect," *Journal of Fluids and Structures*, vol. 48, pp. 188–202, jul 2014.

[19] J. Molina and X. Zhang, "Aerodynamics of a heaving airfoil in ground effect," *AIAA journal*, vol. 49, no. 6, pp. 1168–1179, 2011.

[20] Y. Moryossef and Y. Levy, "Effect of Oscillations on Airfoils in Close Proximity to the Ground," *AIAA Journal*, vol. 42, no. 9, pp. 1755–1764, 2004.

[21] J. Wu, C. Shu, N. Zhao, and W. Yan, "Fluid Dynamics of Flapping Insect Wing in Ground Effect," *Journal of Bionic Engineering*, vol. 11, no. 1, pp. 52–60, Jan. 2014.

[22] J. Wu, Y. L. Qiu, C. Shu, and N. Zhao, "Pitching-motion-activated flapping foil near solid walls for power extraction: A numerical investigation," *Physics of Fluids (1994-present)*, vol. 26, no. 8, p. 083601, Aug. 2014.

[23] J. Wu, Y. L. Qiu, C. Shu, N. Zhao, and X. Wang, "An adaptive immersed boundary-lattice Boltzmann method for simulating a flapping foil in ground effect," *Computers & Fluids*, vol. 106, pp. 171–184, Jan. 2015.

[24] S. C. Licht, "Biomimetic oscillating foil propulsion to enhance underwater vehicle agility and maneuverability," Thesis, Massachusetts Institute of Technology, 2008.

[25] Autonomous Undersea Vehicle Applications Center, "AUV system spec sheet: Razor configuration," 2015, [Online; accessed 09-27-2015]. [Online]. Available: http://auvac.org/configurations/view/218

[26] S. C. Licht, M. S. Wibawa, F. S. Hover, and M. S. Triantafyllou, "In-line motion causes high thrust and efficiency in flapping foils that use power downstroke," *The Journal of Experimental Biology*, vol. 213, no. 1, pp. 63–71, Jan. 2010.

[27] D. A. Read, F. S. Hover, and M. S. Triantafyllou, "Forces on oscillating foils for propulsion and maneuvering," *Journal of Fluids and Structures*, vol. 17, no. 1, pp. 163–183, Jan. 2003.

[28] J. M. Anderson, K. Streitlien, D. S. Barrett, and M. S. Triantafyllou, "Oscillating foils of high propulsive efficiency," *Journal of Fluid Mechanics*, vol. 360, pp. 41–72, Apr. 1998.

[29] J. S. Izraelevitz and M. S. Triantafyllou, "Adding in-line motion and model-based optimization offers exceptional force control authority in flapping foils," *Journal of Fluid Mechanics*, vol. 742, pp. 5–34, 2014.

[30] S. Licht, V. Polidoro, M. Flores, F. S. Hover, and M. S. Triantafyllou, "Design and projected performance of a flapping foil AUV," *IEEE Journal of Oceanic Engineering*, vol. 29, no. 3, pp. 786–794, 2004.

MANUSCRIPT 2

A Hybrid Solver Based on Efficient BEM-Potential and LBM-NS Models: Recent BEM Developments and Applications to Naval Hydrodynamics

by
A.MIVEHCHI[1],J. C. HARRIS[2],S.T. Grilli[1],J.M. Dahl[1],
C.M. O'Reilly[1], K. Kuznetsov[2], C.F. Janssen[3]

(1) Dept. of Ocean Engineering, University of Rhode Island, Narragansett, RI 02882,

USA
(2) LHSV, Ecole des Ponts, CEREMA, EDF R&D, Université Paris-Est, Chatou, France
(3)Fluid Dynamics and Ship Theory Inst., Hamburg University of Technology (TUHH),

Germany

Abstract We report on recent developments of a 3D hybrid model for naval hydrodynamics based on a perturbation method, in which velocity and pressure are decomposed as the sum of an inviscid flow and a viscous perturbation. The far- to near-field inviscid flows are solved with a Boundary Element Method (BEM), based on fully nonlinear potential flow theory, accelerated with a fast multipole method (FMM), and the near-field perturbation flow is solved with a Navier-Stokes (NS) model based on a Lattice Boltzmann Method (LBM) with a LES modeling of turbulent properties. The BEM model is efficiently parallelized on CPU clusters and the LBM model on massively parallel GPGPU co-processors.

2.1 Introduction

We present the hybrid model formulation and latest developments, in particular regarding the improvement and validation of the BEM-FMM model for naval hydrodynamics applications. We show that the BEM-FMM can accurately solve a variety of problems while providing a nearly linear scaling with the number of unknowns (up to millions of nodes) and a speed-up with the number of processors of 35-50%, for small (e.g., 24 cores) to large (e.g., hundreds of cores) CPU clusters. The hybrid model formulation and its latest developments and implementation, in particular, regarding the improvement and validation of the model for naval hydrodynamics applications, are presented in a companion paper by O'Reilly et. al (2017) [1], in this conference. In this paper, we concentrate on the BEM model aspects and show that the BEM-FMM can accurately solve a variety of problems while providing a nearly linear scaling with the number of unknowns (up to millions of nodes) and a speed-up with the number of processors of 35-50%, for small (e.g., 24 cores) to large (e.g., hundreds of cores) CPU clusters.

The simulation of the dynamic response of maritime structures in waves and wave-induced forces is typically based on linear wave models, such as AEGIR [2],

or in case of large motions and/or steep waves, on using nonlinear wave models based on potential flow theory (PFT), usually solved with a higher-order Boundary element method (BEM). For structures with a forward speed, semi-empirical corrections are often made to account for viscous/turbulent effects in the total resistance. While standard Computational Fluid Dynamics (CFD) models based on the full Navier-Stokes (NS) equations can also be used to simulate such problems, their computational cost is typically too prohibitive and their accuracy for long-term wave modeling usually less than that of PFT-BEM models. However, in some cases, the viscous/turbulent flow around the structure's hull and possible breaking waves and wakes require to be more accurately modeled to capture the salient physics of the problem.

Here, instead of using a CFD-NS method to solve the complete problem, we present a fully three-dimensional (3D) hybrid method for solving the hydrodynamic problem based on perturbation method, in which the total velocity and pressure fields are decomposed into inviscid and viscous (perturbation) parts (e.g., [3, 4]). Further, in the hybrid model, the perturbation flow component is only solved in the near-field, using a NS model based on a Lattice Boltzmann Method (LBM; e.g., [5, 6, 7]) with Large Eddy Simulation (LES) of the turbulence (e.g.,[8]); and the far- to near-field inviscid flow component is solved with a BEM model, based on Fully Nonlinear PFT (FNPF). The latter model is also referred to as a "Numerical Wave Tank" (NWT; [9]), since it has the typical functionalities of a physical wave tank (i.e., wave generation, propagation, and absorption). The free surface representation in the LBM is based on a VOF method, with piecewise linear interpolation (PLIC) (e.g.,[10]) and in the NWT on an explicit time updating.

More specifically, in the hybrid model, the NWT solution is computed over the entire domain, for the incident wave field, including diffraction around the

structure and radiation due to its possible motions (for floating-surface piercing structures). The NWT solution results are then used to force the LBM solution, which as indicated is only computed in the near-field of the marine structures, in a domain overlapping with that of the NWT. Hence, the hybrid approach can be much more computationally efficient than traditional CFD solutions, in which the NS solver must be applied to the entire domain.This concept had already been demonstrated for instance by Reliquet et al.[11], based on different types of numerical models; see O'Reilly et al. (2016)[10] and O'Reilly et al. (2017) [1] in this conference, for details of the hybrid model characteristics and efficiency.

The LBM has proved to be accurate and efficient for simulating a variety of complex fluid flow and fluid-structure interaction problems and, when implemented on a massively parallel General Purpose Graphical Processor Unit (GPGPU) co-processor, it has also been shown to achieve very high efficiency (over 100 million node updates per second on a single GPGPU; e.g.,[6, 7, 12]). In this respect, LBM developments in this work are based on the highly efficient, GPGPU-accelerated, Lattice Boltzmann solver ELBE ([13]; www.tuhh.de/elbe), developed at the Hamburg University of Technology (TUHH), which features various LBM models, an on-device grid generator, higher-order boundary conditions, and the possibility of specifying overlapping nested grids. ELBE also includes the earlier LBM perturbation model based on Janssen et al.[7] approach. Simple validations of the hybrid LBM and hybrid LBM-LES approaches, for viscous and turbulent oscillatory boundary layers, were reported by O'Reilly et al. [10], Janssen et al. [13], and in greater details in O'Reilly et al.(2017) at this conference.

For the NWT part of the hybrid model, which is the focus of this paper, we use a 3D-BEM-FNPF model based on the same approach as the wave model of Grilli et al. [9], which was successful at modeling many wave phenomena, in-

cluding landslide generated tsunamis, rogue waves, surface effect ships, and the initiation of wave breaking caused by bathymetry (also see Grilli et al., 2010[14]). For the types of applications considered in earlier work, Grilli et al. were able to use structured grids made of quadrilaterals, which enabled simpler approaches for setting up higher-order (cubic) elements. In order to tackle more complex geometries and grids, as well as accommodating surface-piercing fixed or floating bodies, an implementation of Grilli et al.'s model for unstructured triangular grids was developed in recent years e.g., Harris et al.,[15]). Additionally, the efficiency of the BEM solution in the model for large grids was improved by using a parallelized Fast Multipole Method (FMM; Greengard and Rokhlin,1987[16]), that was efficiently implement on large computer clusters [15] [Note, Grilli et al.'s NWT was accelerated with less efficient scalar FMM; Grilli et al., 2010].

The NWT was initially validated for wave propagation as well as radiation and diffraction from vertical cylinders (Harris et al., 2016). More recent improvements were made to increase the accuracy of such results, for instance, when computing the internal solution within the NWT domain (which is required for coupling to the LBM models). Indeed, the numerical integration of the BEM boundary integrals typically has increasingly large errors for points approaching the domain boundary, such as the free-surface or a maritime structure's hull. Adaptively subdividing the integration over BEM elements in this case (as proposed by Grilli and Subramanya (1994) [17] in 2D and extended by Guyenne and Grilli (2006)[18] in 3D), allows maintaining a constant accuracy of the solution throughout the domain. An adaptive integration method was implemented in the new BEM-FMM-NWT, which also allowed for a more accurate solution near corners and considering elements with larger aspect ratios.

Initially, to represent the solution at corners/edges located at intersections

between various part of the BEM boundary (e.g., sidewall-bottom, free surface-structure, sidewall-free surface,...), the NWT used a multiple-node representation in which, following Grilli and Svendsen (GSV; 1990)[19] and Grilli and Subramanya (GSU; 1996)[20], individual nodes were specified on the various intersecting boundaries, having the same coordinates but different outwards normal vectors. Individual BEM equations were expressed at all nodes of a multiple-node, and continuity conditions were specified for the velocity potential in order to have a non-singular algebraic BEM system (see GSV for details of corner continuity conditions at double-nodes, for a variety of 2D Dirichlet-Neumann problems). To more accurately solve for the flow near strongly moving solid structures intersecting the free surface, such as a wavemaker, GSU formulated and implemented extended compatibility at double nodes in their 2D BEM model, where they also specified that, besides a continuous potential, the flow velocity vector should also be unique at double nodes. In this paper, we extend the latter method to the multiple-nodes occurring in our 3D-BEM NWT, in various mixed boundary condition cases and assess its accuracy through systematic numerical benchmarking.

2.2 Mathematical and Numerical Model
2.2.1 Governing Equations and Boundary Conditions

The 3D-BEM-NWT assumes an incompressible, inviscid and irrotational flow represented by a velocity potential $\phi(\mathbf{x}, t)$, in Cartesian coordinates, with $\mathbf{x} = (x, y, z)$ and z pointing vertically upward. The governing equation is a Laplace's equation for the velocity potential,

$$\nabla^2 \phi = 0 \quad , \quad \text{with} \quad \mathbf{u} = \nabla\phi \quad \text{in} \quad \Omega(t) \tag{13}$$

expressed over the domain $\Omega(t)$ with boundary $\Gamma(t)$, where $\mathbf{u}$ is the veloc-

ity vector. Using Green's second identity, this equation is solved as a Boundary Integral Equation (BIE),

$$\alpha(\mathbf{x}_l)\phi(\mathbf{x}_l) = \int_{\Gamma(\mathbf{x}(t))} \left\{ \frac{\partial \phi}{\partial n}(\mathbf{x})G(\mathbf{x},\mathbf{x}_l) - \phi(\mathbf{x})\frac{\partial G}{\partial n}(\mathbf{x},\mathbf{x}_l) \right\} d\Gamma(\mathbf{x}(t)) \qquad (14)$$

in which $\mathbf{x} = (x, y, z)$ and $\mathbf{x}_l = (x_l, y_l, z_l)$ are points on the boundary, $\mathbf{n} = (n_x, n_y, n_z)$ is the unit outward normal vector on the boundary, and $\alpha(\mathbf{x}_l)$ is a geometric coefficient function of the interior angle of the boundary at $\mathbf{x}_l$. In this BIE, the 3D free space Green's function and its normal derivative are defined as,

$$G(\mathbf{x},\mathbf{x}_l) = \frac{1}{4\pi r_l} \quad \text{and} \quad \frac{\partial G}{\partial n} = -\frac{\mathbf{r}_l \cdot \mathbf{n}}{4\pi r^3} \qquad (15)$$

in which $r_l = |\mathbf{r}_l| = |\mathbf{x} - \mathbf{x}_l|$ is the distance between any point $\mathbf{x}$ from collocation point $\mathbf{x}_l$, both on the boundary $\Gamma(t)$.

On the free surface $\Gamma_f(t)$, ϕ satisfies the nonlinear kinematic and dynamic boundary conditions,

$$\frac{D\mathbf{R}}{Dt} = \mathbf{u} = \nabla\phi \qquad\qquad \text{on} \quad \Gamma_f \qquad (16)$$
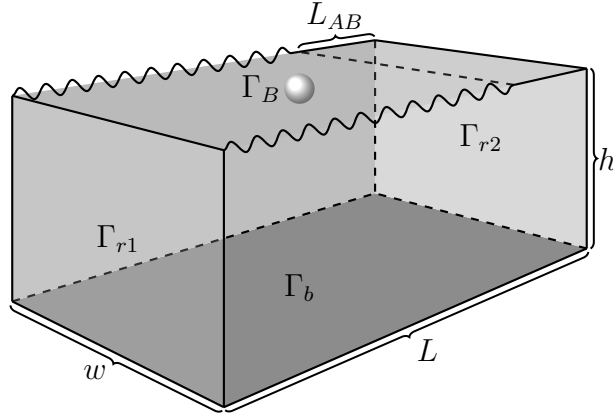
Figure 11: Definition sketch of NWT computational domain for wave interaction with a rigid body (in this paper a Karman-Trefftz foil) (length L by width w by depth h). The no flow condition has been defined for the bottom (Γ_b) and lateral (Γ_{r2}) boundaries; waves are generated on the leftward boundary (Neumann boundary condition for known velocity and acceleration) and are damped on the far end of the NWT over an absorbing beach (AB) of length L_{AB}.

$$\frac{D\phi}{Dt} = -g\zeta + \frac{1}{2}\nabla\phi \cdot \nabla\phi - \frac{p_a}{\rho} \qquad \text{on} \quad \Gamma_f \tag{17}$$

respectively, with $\mathbf{R}$ the position vector of nodes on the free surface, g the acceleration due to gravity, ζ the vertical elevation of the free surface (referred to $z = 0$, denoting the still water level), p_a the atmospheric pressure, ρ the fluid density, and the material derivative being defined as,

$$\frac{D}{Dt} = \frac{\partial}{\partial t} + \mathbf{u}.\nabla \tag{18}$$

In the NWT, waves can be generated by simulating a piston wavemaker motion on the "open sea" boundary of the computational domain, $\Gamma_{r1}(t)$. In this case, wavemaker motion and velocity are specified over the wavemaker paddle as,

$$\overline{x} = x_p; \qquad u_p = -\nabla\phi \cdot \mathbf{n} = -\overline{\frac{\partial\phi}{\partial n}} \qquad \text{on} \quad \Gamma_{r1}(t) \tag{19}$$

respectively, where the overline denotes a specified value (see Grilli et al., 2001 for detail). Along the stationary bottom Γ_b and on other fixed boundaries Γ_{r2}, a no-flow condition is prescribed as,

$$\overline{\frac{\partial\phi}{\partial n}} = 0 \qquad \text{on} \quad \Gamma_b, \ \Gamma_{r2} \tag{20}$$

The boundary condition along a rigid surface piercing maritime structure, which moves with velocity $\mathbf{V}_B$ would be define as,

$$\overline{\frac{\partial\phi}{\partial n}} = \mathbf{V}_B \cdot \mathbf{n} \qquad \text{on} \quad \Gamma_B \tag{21}$$

To prevent wave reflection at open boundaries of the NWT domain an *absorbing beach* (AB) is specified by adding terms: $-\nu(x)\zeta$ and $-\nu(x)\phi$ to the right side of the kinematic and dynamic boundary conditions, respectively, where $\nu = 0$ for all of the domain except for points with abscissa $x \geq x_{AB}$, where $\nu(x) = \nu_0((x - x_{AB})/L_{AB})^2$ (Grilli and Horrillo, 1997 [21]).

2.2.2 BIE for internal velocities

Based on the BIE (77), another BIE can be derived that directly computes the internal velocity as a function of boundary values of the velocity potential and its normal derivative,

$$\mathbf{u} = \nabla\phi(\mathbf{x}_i) = \int \left[\frac{\partial\phi}{\partial n}(\mathbf{x})Q(\mathbf{x},\mathbf{x}_i) - \phi(\mathbf{x})\frac{\partial Q}{\partial n}(\mathbf{x},\mathbf{x}_i) \right] d\Gamma \qquad (22)$$

where $\mathbf{x}_i$ is a point inside domain Ω and (Guyenne and Grilli, 2006 [18]),

$$
\begin{aligned}
Q(\mathbf{x},\mathbf{x}_i) &= \frac{\mathbf{r}_i}{4\pi r_i^3} \\
\frac{\partial Q}{\partial n}(\mathbf{x},\mathbf{x}_i) &= \frac{1}{4\pi r_i^3}\left\{ \mathbf{n} - 3(\mathbf{r}_i \cdot \mathbf{n})\frac{\mathbf{r}_i}{r_i^2} \right\}
\end{aligned}
\qquad (23)
$$

Eqs. (22) and (23) are explicit (i.e., they do not include any new unknown), and can be evaluated with the same discretization as that used to compute the the boundary solution with BIE (77) (see next Section). However, as pointed out by Guyenne and Grilli [18], these are potentially hypersingular equations for $\mathbf{r}_i \to 0$, as they have highly varying kernels for very small $\mathbf{r}_i$ values as compared to the equivalent boundary element length. Hence, as indicated in introduction, an adaptive integration method was implemented; details are given later.

2.2.3 Boundary discretization and standard algebraic system

The BIE (77) is discretized and solved by a BEM, using N_Γ collocation nodes (equal to the number of unknowns) and M_Γ boundary elements, defined over boundary $\Gamma(t)$. In this NWT, in past work, linear isoparametric triangular and quadrangular elements were mostly used, with spline elements being used in a more limited way; future applications, however, will make increasing use of the latter more accurate elements. Given the BEM discretization, BIE (77) is transformed into a sum of integrals over each element, which are computed by numerical integration after transforming each element k, of boundary Γ_e^k, from the physical space

to a standard 2D reference element of domain $\Gamma_{\xi,\eta}$ defined with curvilinear coordinates (ξ, η), by way of a Jacobian matrix $\mathbf{J}^k$. Polynomial shape functions $N_j(\xi, \eta)$, which interpolate both the geometry and field variables over each isoparametric elements, are defined over the reference element. Therefore the integrals in Eq. (77) read,

$$
\begin{aligned}
\int_{\Gamma(x)} \frac{\partial \phi}{\partial n}(\mathbf{x}) G(\mathbf{x}, \mathbf{x}_l) d\Gamma &= \sum_{k=1}^{M_\Gamma} \int_{\Gamma_e^k} \frac{\partial \phi}{\partial n}(\mathbf{x}) G(\mathbf{x}, \mathbf{x}_l) d\Gamma \\
&= \sum_{j=1}^{N_\Gamma} \left\{ \sum_{k=1}^{M_\Gamma} \int_{\Gamma_{\xi,\eta}} N_j(\xi, \eta) G(\mathbf{x}(\xi, \eta), \mathbf{x}_l) |\mathbf{J}^k(\xi, \eta)| \, d\xi d\eta \right\} \frac{\partial \phi}{\partial n}(\mathbf{x}_j) \\
&= \sum_{j=1}^{N_\Gamma} \left\{ \sum_{k=1}^{M_\Gamma} D_{lj}^k \right\} \frac{\partial \phi_j}{\partial n} \\
&= \sum_{j=1}^{N_\Gamma} K_{lj}^d \frac{\partial \phi_j}{\partial n}
\end{aligned}
\tag{24}
$$

and,

$$
\begin{aligned}
\int_{\Gamma(x)} \phi(\mathbf{x}) \frac{\partial G}{\partial n}(\mathbf{x}, \mathbf{x}_l) d\Gamma &= \sum_{k=1}^{M_\Gamma} \int_{\Gamma_e^k} \phi(\mathbf{x}) \frac{\partial G}{\partial n}(\mathbf{x}, \mathbf{x}_l) d\Gamma \\
&= \sum_{j=1}^{N_\Gamma} \left\{ \sum_{k=1}^{M_\Gamma} \int_{\Gamma_{\xi,\eta}} N_j(\xi, \eta) \frac{\partial G}{\partial n}(\mathbf{x}(\xi, \eta), \mathbf{x}_l) |\mathbf{J}^k(\xi, \eta)| \, d\xi d\eta \right\} \phi(\mathbf{x}_j) \\
&= \sum_{j=1}^{N_\Gamma} \left\{ \sum_{k=1}^{M_\Gamma} E_{lj}^k \right\} \phi_j \\
&= \sum_{j=1}^{N_\Gamma} K_{lj}^n \phi_j
\end{aligned}
\tag{25}
$$

in which $l = 1, ..., N_\Gamma$, D_{lj}^k and E_{lj}^k denote the *local* Dirichlet and Neumann element matrices, and K_{lj}^d, K_{lj}^n the corresponding *global* (assembled) matrices, respectively; note that j refers to local nodal values of element k, but is expressed in the global node numbering, by way of assembling.

Eqs. (10) and (11) yield the algebraic form of Eq. (2) as,

$$
\alpha_l \phi_l = \sum_{j=1}^{N_\Gamma} \left\{ K_{lj}^d \frac{\partial \phi_j}{\partial n} - K_{lj}^n \phi_j \right\}
\tag{26}
$$

Boundary conditions are expressed with Eqs. (82) to (84) and the final algebraic system is assembled by moving unknowns to the left hand side and knowns to the right hand side of the equation (see Grilli et al., 2001 [9]for a detailed description of the method.)

Evaluating Eqs. (10) and (11) matrix terms D_{lj}^k and E_{lj}^k requires integrating complex kernels over each boundary element k, which become singular when $r_l \to 0$ in the Green's functions. For triangular elements, the weakly singular integrals are desingularized using Dunavant's (1984) rule [22], and for quadrangular elements by way of a tensor product of Gauss integration. For linear triangular elements, singular integrals can then be analytically integrated. Although analytical solutions of non-singular integrals exist for linear triangular elements, to allow using the same formulation for higher-order elements, we compute these integrals numerically; and likewise for quadrangular elements (e.g., Grilli et al. 2001, 2010 [9, 14]). Coefficients α in the BIE are found by applying the rigid mode method (e.g., Grilli et al. 1989[23]), which expresses that for a Dirichlet problem with a homogeneous $\phi = 1$ value specified over the entire boundary, the discretized BIE solution must yield $\partial\phi/\partial n = 0$; the α coefficients are then found as the residuals of this Dirichlet problem. The discretized algebraic BEM system is solved with BiCGSTAB, a Krylov iterative solver.

In the non-singular integrals, as the free space Green's function Eq. (78) varies rapidly when collocation point l is specified close to the considered element (i.e., $r_l \to 0$), an adaptive integration technique is used, both for collocation points belonging to the boundary discretization or for internal points where the internal velocity is computed with Eqs. (22) and (23). The method used is similar to that described by Grilli et al.(2001) [9] for the same purpose, but here we consider a simpler distance criterion: when the point under consideration is closer to the

center of the element than twice the maximum element edge length, the element is recursively divided into four smaller elements, and this recursive process is done up to 16 times.

2.2.4 Fast Multipole Method

In the FMM, the free space Green's function is approximated for "distant" points by a truncated (order P) multipole expansion,

$$G(\mathbf{x}, \mathbf{x}_l) \approx \sum_{m_x=m_y=m_z=0}^{m_x+m_y+m_z=P} \frac{(x-x_l)^{m_x}(y-y_l)^{m_y}(z-z_l)^{m_z}}{m_x!\, m_y!\, m_z!}$$
$$\left\{ \left(\frac{\partial}{\partial x}\right)^{m_x} \left(\frac{\partial}{\partial y}\right)^{m_y} \left(\frac{\partial}{\partial z}\right)^{m_z} G(\mathbf{x}, \mathbf{x}_l) \right\} \tag{27}$$

In this approach, both interactions that are "distant enough" are neglected (yielding a sparse algebraic system matrix) and the full system matrix of the BIE does not have to be assembled and solved, which is typically one of the most time consuming part of the NWT solution, as it has a $O(N_\Gamma^2)$ numerical complexity. More specifically, to decide how to approximate (or even neglect) interactions, the FMM uses a divide-and-conquer strategy based on the distance between two points. Importantly, by assigning intermediate points (e.g., at the centers of groups of nodes or elements of the boundary mesh) and applying the binomial theorem, one is able to manipulate multipole coefficients that only need to be computed once, instead of directly evaluating the BIE between each element and node (see Harris et al., 2016 [24] for details).

Theoretically, if efficiently implemented and assuming N_Γ is more than a few thousand, the computational time of the FMM should scale with $O(N_\Gamma)$ or so. This is much faster than the solution of the complete BEM system with the best iterative solvers (which is $O(N_\Gamma^2)$). Several variations have been proposed for the implementation of the FMM on parallel clusters [25], which generally rely on domain decomposition, whereby the FMM is first applied on each processor over some

region of space and then results are combined. Harris et al. [24] implemented this domain decomposition parallel FMM approach and studied the scaling of the two main phases of the FMM-BEM, using an iterative solver : (i) the assembling of the global system (sparse) matrix, and (ii) the matrix-vector products involved in the FMM. They showed good scaling of the FMM-BEM assembling and matrix-vector products for a mesh with quadrangular elements and $N_\Gamma = 79,202$ nodes, with varying numbers of CPUs, up to a few hundreds, over a simple parallelipipedical domain, typical of modeling of nonlinear waves (e.g., Fig. 1). The grid was partitioned into 1,024 sub-domains and a 15th-order FMM expansion was used, with 100 integration points were used on each element.

While this approach permits good scaling, up to hundreds of processors and a billion unknowns [26], for BEM problems solved on small desktop computer clusters, that may only have $O(10^5)$ unknowns and less than 100 processors, a simpler approach referred to as single-level FMM was found to scale much more efficiently. This was pointed out by Waltz et al. (2007), who compared this approach to many other parallelization attempts of the FMM-BEM and showed that this is due to the fact that while the number of unknowns is large enough for the FMM to be efficient, the number of unknowns per processor is low. The FMM scaling of the present NWT will be studied later in applications.

2.2.5 Curvilinear coordinate transformation

A local non-orthogonal curvilinear coordinate system is used, following Fochesato et al. [27], to represent the geometry of higher-order BEMs, and field variables and their derivatives at each collocation node on the boundary, which extends the orthogonal coordinate assumption made by Grilli et al. [9]. Thus, at any point $\mathbf{x}$ within a n-node isoparametric BEM element k, the geometry and local

47

non-orthogonal unit tangential vectors are defined as,

$$\mathbf{x} = \sum_{j=1}^{n} N_j(\xi, \eta) \mathbf{x}_j^k \quad \text{and} \quad \mathbf{s} = \frac{\partial \mathbf{x}}{\partial \xi} \bigg/ \left| \frac{\partial \mathbf{x}}{\partial \xi} \right|, \quad \mathbf{m} = \frac{\partial \mathbf{x}}{\partial \eta} \bigg/ \left| \frac{\partial \mathbf{x}}{\partial \eta} \right| \qquad (28)$$

where $\mathbf{x}_j^k$ are the element k nodal coordinates. The unit vectors of a corresponding local orthogonal coordinate system $(\mathbf{s}, \mathbf{m}', \mathbf{n})$ are then defined as,

$$\mathbf{m}' = \frac{1}{\sqrt{1 - \kappa^2}} \mathbf{m} - \frac{\kappa}{\sqrt{1 - \kappa^2}} \mathbf{s} \quad \text{with} \quad \kappa = \mathbf{s} \cdot \mathbf{m} \qquad (29)$$

the cosine of the angle between the unit tangential vectors. The normal vector to the $(\mathbf{s}, \mathbf{m})$ plane (pointing outwards depending on proper number of element nodes) completes this orthogonal coordinate system and can be calculated as,

$$\mathbf{n} = \mathbf{s} \times \mathbf{m}' \qquad (30)$$

The Jacobian of the transformation between element k, in the global coordinate system, to the reference element is defined as,

$$|\mathbf{J}^k(\xi, \eta)| = \left\{ \left| \frac{\partial \mathbf{x}}{\partial \xi} \right|, \left| \frac{\partial \mathbf{x}}{\partial \eta} \right|, \mathbf{n} \right\}, \qquad (31)$$

which can be computed at any point $\mathbf{x}$ of element k with Eqs. (14-16).

Similarly, the gradient of the velocity potential, i.e., flow velocity, is expressed as [27],

$$\nabla \phi = \frac{1}{1 - \kappa^2} \left(\frac{\partial \phi}{\partial s} - \kappa \frac{\partial \phi}{\partial m} \right) \mathbf{s} + \frac{1}{1 - \kappa^2} \left(\frac{\partial \phi}{\partial m} - \kappa \frac{\partial \phi}{\partial s} \right) \mathbf{m} + \frac{\partial \phi}{\partial n} \mathbf{n} \qquad (32)$$

which can also be computed based on Eqs. (14-16), assuming the tangential and normal derivatives of the potential are known. The normal derivatives of the potential are obtained from BIE (2)'s solution and the computation of tangential derivatives is detailed below.

As for the geometry, the potential ϕ over an isoparametric element k is defined as the sum of nodal values multiplied by shape functions defined over the reference

48

element,

$$\phi = \sum_{j=1}^{n} N_j(\xi, \eta) \phi_j^k \tag{33}$$

The tangential derivatives of the potential over each element (i.e., tangential velocities) can thus be calculated by direct differentiation of Eq. (33) with the operators,

$$\frac{\partial}{\partial s} = \frac{\partial}{\partial \xi} \bigg/ \left| \frac{\partial \mathbf{x}}{\partial \xi} \right| \qquad \text{and} \qquad \frac{\partial}{\partial m} = \frac{\partial}{\partial \eta} \bigg/ \left| \frac{\partial \mathbf{x}}{\partial \eta} \right| \tag{34}$$

Hence, the tangential derivatives at point $\mathbf{x}_l = \mathbf{x}(\xi_l, \eta_l)$ of element k read,

$$\frac{\partial \phi}{\partial s} = \sum_{j=1}^{n} \frac{\partial N_j(\xi, \eta)}{\partial \xi} \frac{1}{\left| \frac{\partial \mathbf{x^k}}{\partial \xi} \right|} \phi_j^k = \sum_{j=1}^{n} \mathscr{S}_j^k \phi_j^k \tag{35}$$

$$\frac{\partial \phi}{\partial m} = \sum_{j=1}^{n} \frac{\partial N_j(\xi, \eta)}{\partial \eta} \frac{1}{\left| \frac{\partial \mathbf{x^k}}{\partial \eta} \right|} \phi_j^k = \sum_{j=1}^{n} \mathscr{M}_j^k \phi_j^k \tag{36}$$

Higher-order derivatives of the geometry and the potential on the boundary can be defined in the same manner, in the local orthogonal coordinate system (see [27]).

2.2.6 Treatment of corners in global system matrix

As mentioned in the introduction, following Grilli et al. [19, 20, 9], corners and edges of the BEM discretization, which mark intersections of different parts of the boundary of the computational domain, in general have different normal directions and boundary conditions. These are represented by multiple nodes, for which multiple BIEs are expressed based on different values of the normal derivative of the potential, but using a single value of the potential, as the latter must be unique (i.e., continuous) at the same location. This condition is enforced in the BEM solution by modifying all but one of the assembled algebraic equations for each multiple node, to satisfy a *potential continuity* condition. This assumes

that initially (for $t = 0$) the boundary conditions at all corners are prescribed in a way that does not cause a mathematical singularity in the problem.

In a 3D space there are both *double* (e.g., between the wavemaker and the free surface) and *triple* (e.g., where the wavemaker and free surface boundaries meet with a sidewall boundary) nodes. Thus, for double/triple nodes, there are 2/3 discretized BIEs expressed at each multiple node. To ensure uniqueness and well-posedness of the solution, however, and in particular a single potential at any given location, 1 (in case of a double node) or 2 (in case of a triple node) of these BIEs must be modified in the final algebraic system to ensure that both the global matrix is not singular and the solution yields a single (continuous) potential. For the simple domain shown in Fig. 28, the multiple nodes can be categorize based on their boundary conditions as : (i) Dirichlet-Neumann (DN) double nodes (e.g., wakemaker and free surface boundary); (ii) Neumann-Neumann (NN) double nodes (e.g., bottom and sidewall boundaries); (iii) Neumann-Neumann-Neumann (NNN) triple nodes (e.g., where the wavemaker, bottom and sidewall boundaries meet); and (iv) Drichlet-Neumann-Neumann (DNN) (e.g., where the wavemaker, free surface and sidewall boundaries meet).

In a NWT with a moving free surface, possibly moving maritime structure(s), and a moving wavemaker, Grilli and Subramaniya [20] showed in their 2D work that, to ensure a stable and accurate solution near multiple-nodes, the velocity vector should also be unique at such nodes, particularly on the free surface. Besides achieving an accurate solution, this will also ensure that individual nodes on the free surface, that are part of multiple nodes, move to an identical location through time updating. These authors indeed showed that if velocity is not explicitly *enforced* to be unique at multiple nodes, by modifying the algebraic BIE system in a proper way, large numerical errors will occur at and near such nodes in the BIE

solution, which will grow even larger through time updating and, eventually, lead to instability of the solution, particularly close to strongly moving rigid boundaries.

Hence, following Grilli and Subramanya [20], in the 3D-NWT, we extended the simple potential continuity condition at multiple nodes used in earlier work to also enforce uniqueness of the velocity (i.e., gradient of the potential) at individual nodes of multiple nodes. This was done for all cases of mixed boundary conditions (e.g., DN, NN, NNN, DNN) by replacing all but one of the assembled equations of a multiple node in the algebraic system, by a so-called velocity *compatibility* condition, which also includes the potential continuity condition; in the following, we only present one example for a DN double-node case. These extended multiple-node conditions, in fact, make the representation of the solution compatible (i.e., consistent) on both sides of a corner and effectively eliminate the occurrence of (numerical) singularities in the discretized solution. When using compatibility conditions at corners when solving mixed boundary value problems in simple rectangular domains, Grilli and Subramaniya [20] showed that numerical errors at corners could be reduced to almost arbitrarily small values in their 2D-NWT.

For instance, at a DN double node located at the intersection between a piston wavemaker and the free surface, the compatibility condition forced the BIE solution to compute a (corrected) value of the tangential velocity on the free surface node $l = f$ (of the double node), $\partial \phi_f / \partial s$, as a function of both the normal velocity $\partial \phi_f / \partial n$ obtained from the solution of the BIE (25) at the current time step, and the (specified) wavemaker velocity on the wavemaker node $l = p$ (of the double node), $\partial \phi_p / \partial n = -u_p$ (see Eq. (82)). Here, expressing this compatibility condition at a similar DN double nodes, defined at the intersection between the free surface and a wavemaker/maritime structure boundary in the 3D-NWT, we specify that

$\mathbf{u}_p = \mathbf{u}_f$, i.e.,

$$\frac{\overline{\partial \phi_f}}{\partial s}\mathbf{s}_f + \frac{\overline{\partial \phi_f}}{\partial m'}\mathbf{m}'_f + \frac{\partial \phi_f}{\partial n}\mathbf{n}_f = \frac{\partial \phi_p}{\partial s}\mathbf{s}_p + \frac{\partial \phi_p}{\partial m'}\mathbf{m}'_p + \frac{\overline{\partial \phi_p}}{\partial n}\mathbf{n}_p \quad (37)$$

in which the overlines indicate known/specified values. Note that the tangential derivatives of the specified potential on the free surface (Dirichlet boundary) are computed by way of the tangential derivative operators defined in Eqs. (35) and (36), assuming $l = f$ or $l = p$.

Moving the unknowns to the left-hand-side and projecting the equation in the direction of unit vector $\mathbf{i}$, we find,

$$-\frac{\partial \phi_p}{\partial s}(\mathbf{s}_p \cdot \mathbf{i}) - \frac{\partial \phi_p}{\partial m'}(\mathbf{m}'_p \cdot \mathbf{i}) + \frac{\partial \phi_f}{\partial n}(\mathbf{n}_f \cdot \mathbf{i}) =$$
$$-\frac{\overline{\partial \phi_f}}{\partial s}(\mathbf{s}_f \cdot \mathbf{i}) - \frac{\overline{\partial \phi_f}}{\partial m'}(\mathbf{m}'_f \cdot \mathbf{i}) + \frac{\overline{\partial \phi_p}}{\partial n}(\mathbf{n}_p \cdot \mathbf{i}) = \overline{u^i} \quad (38)$$

Assuming that element k is on the free surface boundary and element m is on the wavemaker/maritime structure boundary, and replacing the tangential derivatives into Eq. (38), while specifying the potential continuity condition $\phi_1^m = \overline{\phi_1^k}$, we find

$$-\sum_{j=2}^{n} \frac{\{\mathscr{S}_j^m - \kappa_m \mathscr{M}_j^m\}C_{s_p i} + \{\mathscr{M}_j^m - \kappa_m \mathscr{S}_j^m\}C_{m_p i}}{1 - \kappa_m^2}\phi_j^m + \frac{\partial \phi_f}{\partial n}C_{n_f i} =$$
$$-\sum_{j=1}^{n} \frac{\{\mathscr{S}_j^k - \kappa_k \mathscr{M}_j^k\}C_{s_f i} + \{\mathscr{M}_j^k - \kappa_k \mathscr{S}_j^k\}C_{m_f i}}{1 - \kappa_k^2}\phi_j^k + \frac{\overline{\partial \phi_p}}{\partial n}C_{n_p i}$$
$$+ \frac{\{\mathscr{S}_1^m - \kappa_m \mathscr{M}_1^m\}C_{s_p i} + \{\mathscr{M}_1^m - \kappa_m \mathscr{S}_1^m\}C_{m_p i}}{1 - \kappa_m^2}\phi_1^k = \overline{u'^i} \quad (39)$$

in which the C coefficients are the cosines of the angles between the unit vectors indicated as lower indices. For a DN wavemaker boundary, such as considered in this example, direction $\mathbf{i}$ can be individually selected at each double node, as the horizontal projection of the local normal vector to the wavemaker boundary $\mathbf{n}_p$.

Note that in Eq. (39) there are n unknowns in the left-hand side, $n-1$ potential values at the non-multiple nodes of element m on the wavemaker boundary and 1 normal derivative of the potential on the free surface node of the multiple node in element k; the right-hand side of the equation $\overline{u'^i}$ is built with specified or known values at the current time. Eq. (39) is substituted for 1 of the two BIE equations assembled in the BEM algebraic system for this DN double node.

In case of orthogonal elements (i.e., when $\kappa = 0$) and with $\mathbf{m} \cdot \mathbf{i} = 0$ for 2D problems, Eq. (39) simplifies to the equation developed by Grilli and Subramanya [20] and used as extended compatibility condition in their 2D-NWT.

For triple nodes, such as DNN, for instance at the intersection between a wavemaker $l = p$, free surface $l = f$, and sidewall $l = q$ boundary, 2 equations such as Eq. (37) would be derived, expressing $\mathbf{u}_p = \mathbf{u}_f = \mathbf{u}_q$, leading to 2 equations similar to Eq. (39), based on projections of each of these in directions $\mathbf{i}$ and $\mathbf{j}$, for instance pointing in the direction of the horizontal projections of the local normal vectors to the wavemaker and sidewall boundaries, respectively ($\mathbf{n}_p$ and $\mathbf{n}_q$). These 2 equations would then replace 2 of the 3 BIE equations assembled in the BEM algebraic system for this DNN triple node. Doing this, in the BEM solution, the value of the normal velocity at the free surface node of the triple node would depend upon both distributions of potential along the 2 intersecting Neumann boundaries.

2.3 Applications
2.3.1 Scaling of the FMM-BEM solution on parallel CPU clusters

We performed the same scaling study as Harris et al. [24], but on a small desktop CPU cluster with shared memory, of the solution of a mixed boundary condition Laplace problem over the domain of Fig. 15; the domain was discretized with $N_\Gamma = 54,000$ nodes, and the problem solved with 1,2,4,8 or 16 CPUs. In

N_Γ	MAX with CC	RMS($\frac{\partial\phi}{\partial n}$) with CC	RMS(ϕ) with CC	MAX without CC	RMS($\frac{\partial\phi}{\partial n}$) without CC	RMS(ϕ) without CC
54	5.2984e-07	5.2938e-07	5.7738e-07	1.8131e-05	8.3901e-06	5.2273e-07
150	8.2993e-06	5.4940e-06	4.4905e-07	4.8857e-05	2.0582e-05	4.8828e-07
726	6.8341e-06	1.51491r-06	2.7939e-07	1.0558e-05	1.0558e-05	3.5162e-07
2,646	4.3483e-06	1.1496e-06	2.6854e-07	6.9098e-05	1.9098e-05	3.4782e-07
10,086	1.7760e-06	1.1326e-06	2.3885e-07	3.1012e-05	1.3773e-05	3.2742e-07

Table 4: Numerical errors (maximum (MAX); and root-mean-square (RMS) of the 3D-NWT solution over a unit size cube domain, with and without multiple-node compatibility conditions (CC), as a function of the number of nodes N_Γ.

the FMM, the grid was partitioned into 32 sub-domains, and 10 integration points were used on each element. Fig. 12 shows the speed-up of the system matrix assembly, total 3D-FMM-BEM solution, and internal velocity, computational time as a function of the CPU time on a single core. We see that on this small system, while a significant speed up, almost optimal, of the complete solution is achieved up to 4 CPUs, the marginal gain in speed-up is much smaller when further increasing the number of CPUs. This is related to the internal architecture and CPU to CPU communications within the small desktop cluster.

Next, on the same system and for the same Laplace problem, we studied the scalability of the 3D-FMM-BEM complete solution for 1 and 8 CPUs, as a function of the number of nodes $N_\Gamma = 5,000$ to 100,500. Results in Fig. 13 show an $O(N^{1.05})$ scaling for 1 and $O(N_\Gamma^{1.09})$ scaling for 8 CPUs, which both are quite close to the optimal theoretical scaling $O(N_\Gamma)$.

2.3.2 Compatibility conditions at multiple nodes

To assess the accuracy of the new velocity compatibility conditions (CC) implemented at multiple nodes in the 3D-NWT, we performed a convergence test of the solution of a mixed boundary value problem over a unit size cube, which has a simple analytical solution, as a function of the number nodes, $N_\Gamma = 54$ to 10,086 (note, 54 nodes is the minimum number for a cube to contain both double and triple nodes).
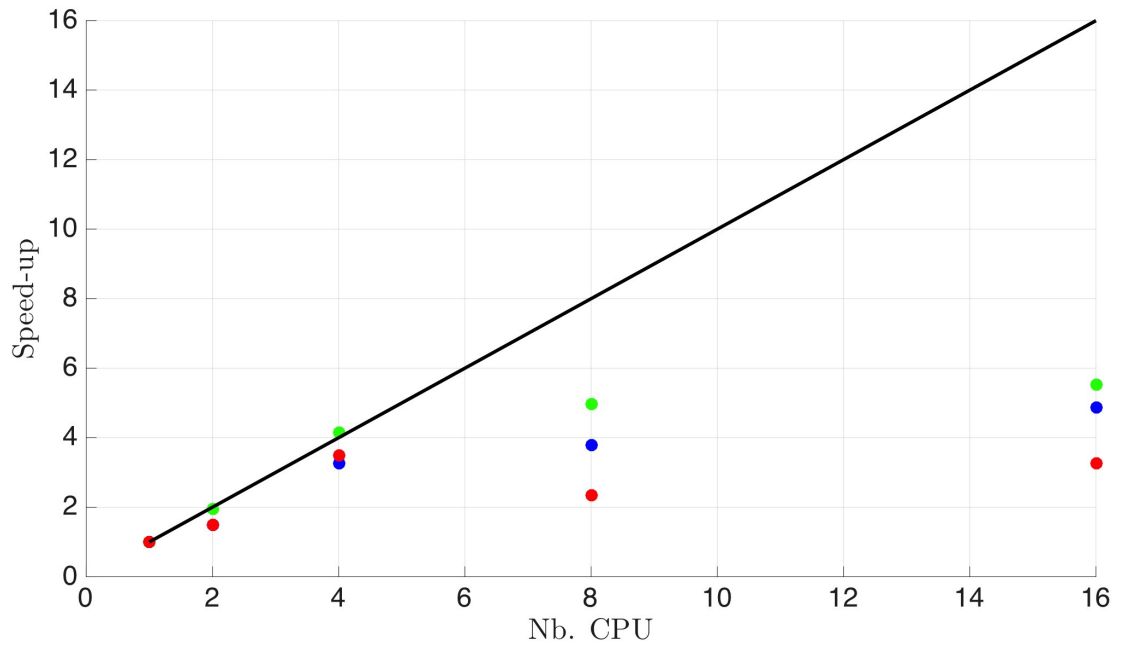
Figure 12: Speed-up of the 3D-FMM-BEM solution of a mixed-boundary condition Laplace problem over the domain of Fig. 28, as a function of the number of CPUs on a small desktop cluster, for: (i) matrix assembling (•); (ii) internal velocity calculation (as a vector product sample) (•); and (iii) complete solution (•). A grid of quadrangular linear elements is used with $N_\Gamma = 54,000$ collocation points.
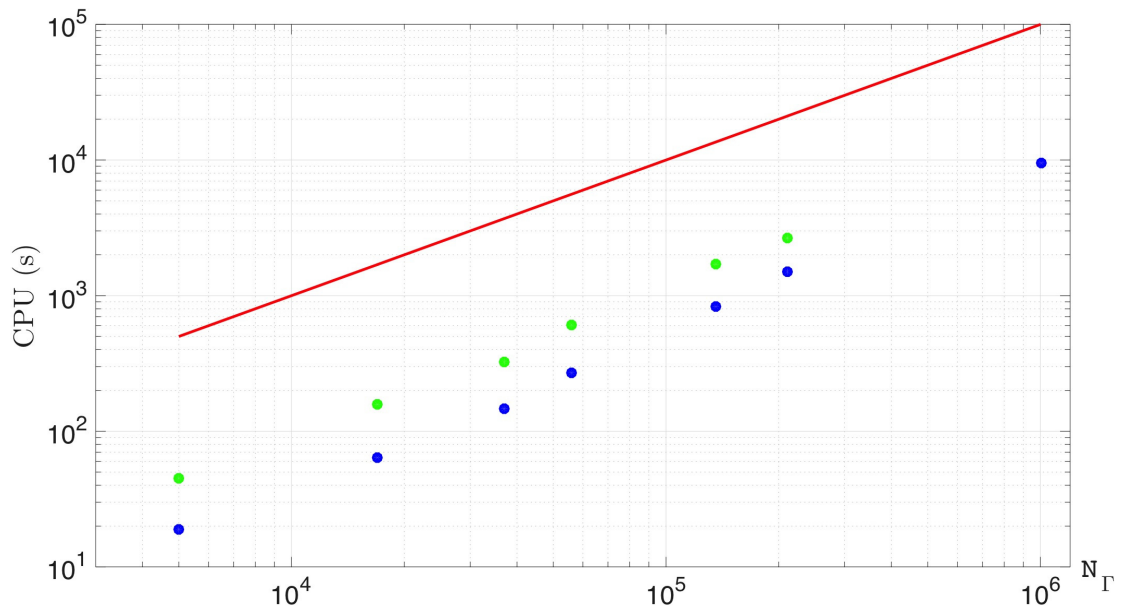
Figure 13: Same case as 12. CPU time of the 3D-FMM-BEM solution for $N_\Gamma = 5,000$ to 100,500 nodes, using 1 (•) and 8 (•) CPUs on a small desktop cluster. The red line shows an $O(N_\Gamma)$ scalability, whereas it is $O(N_\Gamma^{1.05})$ for 1 CPU.

Both maximum (MAX) and root-mean-square (RMS) errors (over the entire grid) of the solution were computed, with and without compatibility conditions, based on values of the normal velocity $\partial\phi/\partial n$ or potential ϕ. These are listed in Table 1. In all cases, the potential continuity conditions were specified at multiple nodes. Although RMS errors are only slight smaller with compatibility conditions than without, the maximum errors on normal velocity, which occur at multiple nodes, are much reduced when specifying compatibility conditions, particularly for the larger discretization. We verified that differences are much larger between the two methods for a domain with complex geometry and, based on earlier work (Grilli and Subramanya [20]), we expect these to be even larger once we will be updating the free surface geometry and or the position of wavemaker/maritime structures as a function of time, since this will cause cumulative error effects.

2.3.3   Computation of internal velocities

As discussed in introduction, this work is part of broader project to develop a hybrid solver for naval hydrodynamics problem, based on an coupling an efficient BEM-FNPF model, i.e., the 3D-BEM-FMM NWT discussed here, and a LBM solution of Navier-Stokes (NS) equations, through a perturbation approach. In the hybrid solver, the potential flow solution is used to force the LBM-NS solution for the viscous perturbation flow (see, Harris and Grilli (2012) and O'Reilly et al. (2017), in this conference). This requires computing the internal velocity field at many points within the NWT domain, at each time step.

Here, we validate the computation of the internal velocity field in the 3D-NWT by computing the flow around a symmetric Karman-Trefftz foil (see Abbot and Von Doenhoff,[28]), for a free flow velocity U in the x-direction. Specifying the 3D-NWT boundary conditions to solve a 2D problem (using no-flow conditions on the sidewalls in the y-direction and upper and bottom boundaries in the z-direction),
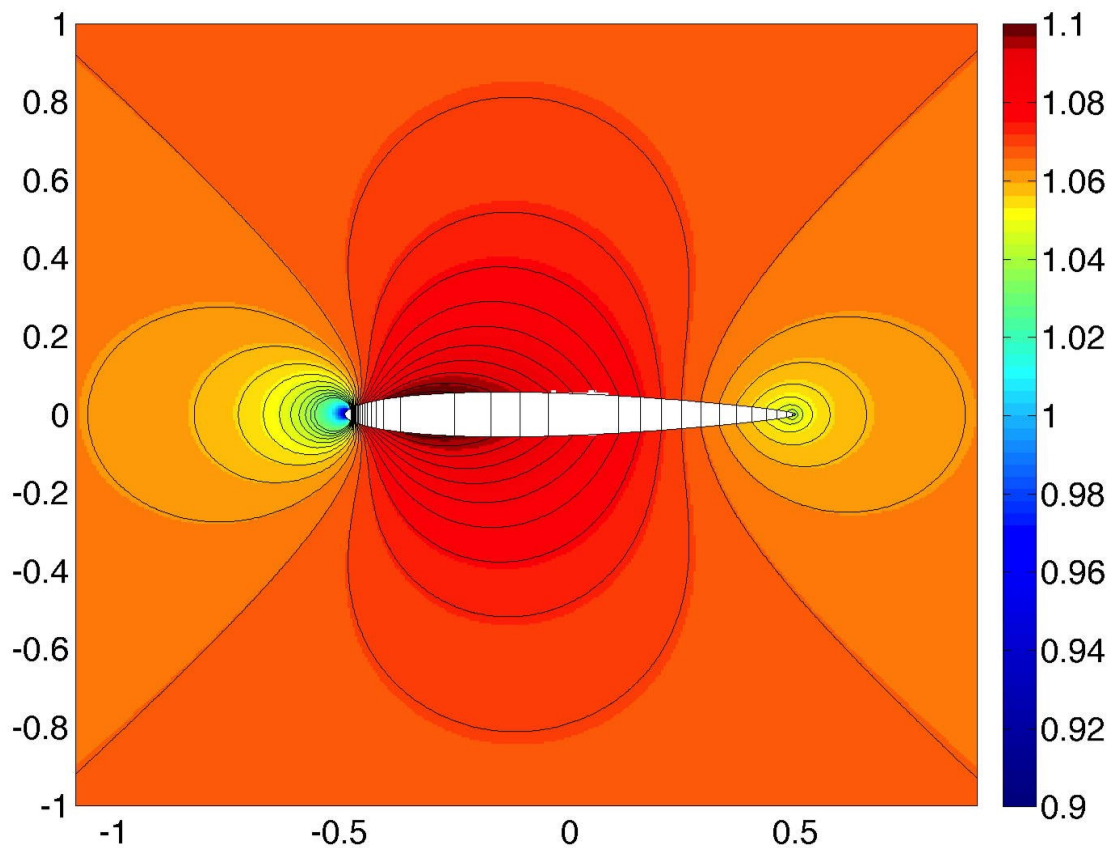
Figure 14: Analytical solution for the scaled module of velocity $\mathbf{u}/U$ of the (uniform) flow around a symmetric Karman-Trefftz foil.
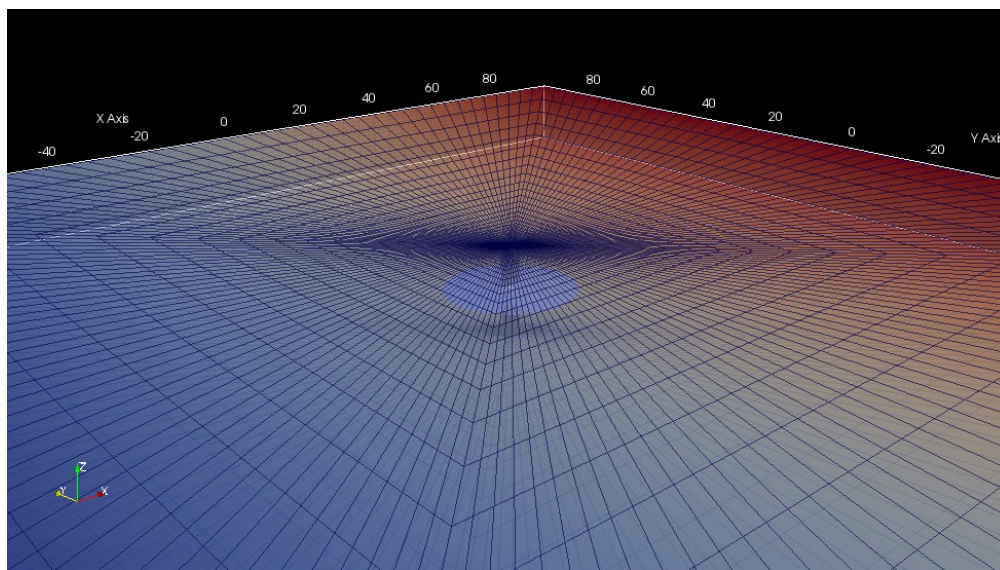
Figure 15: Computational domain for the computation of the (uniform) flow around a symmetric Karman-Trefftz foil, using $M_\Gamma = 15,488$ linear quadrangular elements.

(a)

(b)
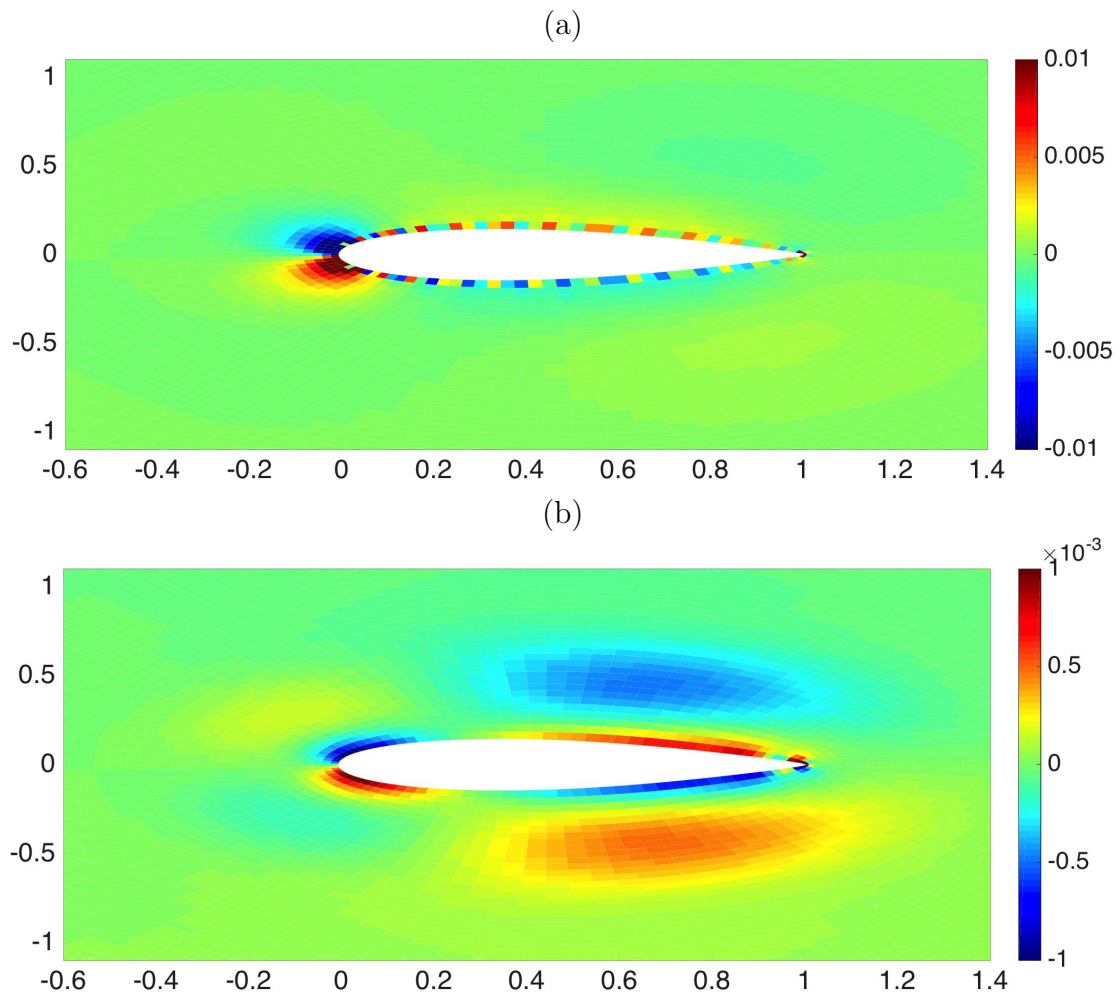
Figure 16: Case of Fig. 15. Zoom-in on relative errors of velocity module computed using: (a) linear, or (b) B-spline quadrilateral elements.

an analytical solution of the flow around the foil can be expressed based on a conformal mapping in the complex plane $\zeta = x + iy$,

$$Z(\zeta) = n\lambda\frac{(1 + \frac{\lambda}{\zeta})^n + (1 - \frac{\lambda}{\zeta})^n}{(1 + \frac{\lambda}{\zeta})^n - (1 - \frac{\lambda}{\zeta})^n} \tag{40}$$

which maps a cylinder of radius R centered at $\zeta = x = s$, for which the complex potential is the trivial superposition of a uniform flow of velocity U and a dipole: $W(\zeta) = U(\zeta + R^2/\zeta)$, to the symmetric foil, where $n = 2 - \beta/\pi$, with β the angle at the foil trailing edge, and $\lambda = R + s$. Selecting $R = 1$ and the foil center at $s = -0.045$ we find $\beta = 8^o$. The 2D analytical solution for the scaled module of velocity $\mathbf{u}/U$ around this foil is shown in Fig. 14.

We consider a rectangular domain, with extension $-100 < x < 100$, $-100 < z < 100$, and solve this 2D flow in 3D using a transverse direction y extending from, $-15 < z < 0$. The computational domain boundary is discretized with $M_\Gamma = 15,488$ quadrangular elements with increasing resolution towards the foil (Fig. 15), which are either: (i) linear isoparametric; or (ii) cubic B-spline elements; in the FMM, 15th-order expansions are used in the BEM solution of Eq. (2). Compatibility conditions are specified here at all multiple nodes. We then compute the velocity field with Eq. (22) at 10,000 internal points $\mathbf{x}_i$, most of these being located near the foil surface, and compare it with the analytical solution. In Fig. 16a, we find that for case (i), maximum errors in velocity reach 0.45% near the foil leading and trailing edges, while the L^2-error is 10^{-6} over the entire set of internal points. For case (ii), however, in Fig. 16b, these errors are about 10 times smaller confirming the well known property and importance of using higher-order elements in the BEM.

2.4 Conclusion

In this paper, we reported on recent improvements in the implementation of a 3D-NWT solving FNPF with a free surface. The NWT is based on a BEM, using

linear or cubic B-spline elements, and the solution is accelerated with an efficient FMM, showing nearly linear scaling in both scalar and parallel computations. The NWT is a component of a hybrid model, in combination with a Navier-Stokes LBM model with Large eddy simulation, aimed at solving naval hydrodynamic problems (e.g., ship sea-keeping).

We showed, in particular, a good scaling of the FMM-BEM numerical solution with problem size N_Γ near the theoretical optimal ($O(N_\Gamma)$) and reasonable additional speed-up with the number of processors in a parallel implementation. Well-posed velocity compatibility conditions were developed and implemented for multiple nodes at the corners and edges of the 3D domain, which extend earlier 2D formulations by Grilli and Svendsen (1990), Grilli and Subramanya (1996), and Grilli et al. (2001). These were shown to reduce errors in the numerical solution for various discretizations and cases.

We presented results for a uniform flow past a submerged symmetric foil and showed that internal velocities could be both efficiently and accurately computed by applying the same FMM-BEM approach. Such internal velocity fields are used in the hybrid model to force the viscous perturbation LBM solution based on the inviscid flow results in the NWT (e.g., O'Reilly et al., 2016, 2017, the latter paper at this conference).

By extending the NWT formulation to a moving coordinate systems and (later) to arbitrary geometries, we will be able to handle a broader range of more complex applications of particular interest to Naval Hydrodynamics and ocean engineering. The extension of the BEM to higher-order B-spline elements (e.g., Maestre et al.[29] 2016; Harris et al. paper at this conference), which was achieved without fundamental changes in the FMM-NWT formulation, already demonstrated for the foil that numerical errors can be significantly reduced. This will be

very important in naval hydrodynamics applications, when modeling submerged or floating bodies of complex geometry.

2.5   Acknowledgements

List of References

[1] C. O'Reilly, S. Grilli, J. Harris, A. Mivehchi, C. Janssen, J. Dahl, *et al.*, "A hybrid solver based on efficient bem-potential and lbm-ns models: Recent lbm developments and applications to naval hydrodynamics," in *The 27th International Ocean and Polar Engineering Conference.* International Society of Offshore and Polar Engineers, 2017.

[2] D. Kring, F. Korsmeyer, J. Singer, D. Danmeier, and J. White, "Accelerated nonlinear wave simulations for large structures," in *7th International Conference on Numerical Ship Hydrodynamics, Nantes, France*, 1999, pp. 1–16.

[3] B. Alessandrini, "These dhabilitation en vue de diriger les recherches," *Ecole Centrale de Nantes, Nantes*, 2007.

[4] S. T. Grilli, "On the development and application of hybrid numerical models in nonlinear free surface hydrodynamics," in *Proc. 8th Int. Conf. on Hydrodynamics*, 2008, pp. 21–50.

[5] D. d'Humières, "Multiple–relaxation–time lattice boltzmann models in three dimensions," *Philosophical Transactions of the Royal Society of London A: Mathematical, Physical and Engineering Sciences*, vol. 360, no. 1792, pp. 437–451, 2002.

[6] C. F. Janssen, M. Krafczyk, S. Grilli, *et al.*, "Modeling of wave breaking andwave-structure interactions by coupling of fully nonlinear potential flow and lattice-boltzmann models," in *The Twentieth International Offshore and Polar Engineering Conference.* International Society of Offshore and Polar Engineers, 2010.

[7] C. Janssen, "Kinetic approaches for the simulation of non-linear free surface flow problems in civil and environmental engng," Ph.D. dissertation, PhD thesis, Technical Univ. Braunschweig, 2010.

[8] M. Krafczyk, J. Tölke, and L.-S. Luo, "Large-eddy simulations with a multiple-relaxation-time lbe model," *International Journal of Modern Physics B*, vol. 17, no. 01n02, pp. 33–39, 2003.

[9] S. T. Grilli, P. Guyenne, and F. Dias, "A fully non-linear model for three-dimensional overturning waves over an arbitrary bottom," *International Journal for Numerical Methods in Fluids*, vol. 35, no. 7, pp. 829–867, 2001.

[10] C. OREILLY, S. GRILLI, J. HARRIS, A. MIVEHCHI, C. JANSSEN, and J. DAHL, "Development of a hybrid lbm-potential flow model for naval hydrodynamics."

[11] G. Reliquet, A. Drouet, P. Guillerm, L. Gentaz, and P. Ferrant, "Simulation of wave-ship interaction in regular and irregular seas under viscous flow theory using the swense method," in *Proc. 30th Symp. Naval Hydrod.(Tasmania, 11/2014)*, 2014.

[12] A. Banari, C. F. Janßen, and S. T. Grilli, "An efficient lattice boltzmann multiphase model for 3d flows with large density ratios at high reynolds numbers," *Computers & Mathematics with Applications*, vol. 68, no. 12, pp. 1819–1843, 2014.

[13] C. F. Janßen, D. Mierke, M. Überrück, S. Gralher, and T. Rung, "Validation of the gpu-accelerated cfd solver elbe for free surface flow problems in civil and environmental engineering," *Computation*, vol. 3, no. 3, pp. 354–385, 2015.

[14] S. T. Grilli, F. Dias, P. Guyenne, C. Fochesato, and F. Enet, "Progress in fully nonlinear potential flow modeling of 3d extreme ocean waves," in *Advances in numerical simulation of nonlinear water waves*. World Scientific, 2010, pp. 75–128.

[15] J. Harris, E. Dombre, M. Benoit, and S. Grilli, "A comparison of methods in fully nonlinear boundary element numerical wave tank development," *14émes Journées de lHydrodynamique*, 2014.

[16] L. Greengard and V. Rokhlin, "A fast algorithm for particle simulations," *J. Comput. Phys.*, vol. 73, pp. 325–348, 1987.

[17] S. T. Grilli and R. Subramanya, "Quasi-singular integrals in the modeling of nonlinear water waves in shallow water," *Engineering Analysis with Boundary Elements*, vol. 13, no. 2, pp. 181–191, 1994.

[18] P. Guyenne and S. Grilli, "Numerical study of three-dimensional overturning waves in shallow water," *Journal of Fluid Mechanics*, vol. 547, pp. 361–388, 2006.

[19] S. Grilli and I. Svendsen, "Corner problems and global accuracy in the boundary element solution of nonlinear wave flows," *Engineering Analysis with Boundary Elements*, vol. 7, no. 4, pp. 178–195, 1990.

[20] S. T. Grilli and R. Subramanya, "Numerical modeling of wave breaking induced by fixed or moving boundaries," *Computational Mechanics*, vol. 17, no. 6, pp. 374–391, 1996.

[21] S. T. Grilli and J. Horrillo, "Numerical generation and absorption of fully nonlinear periodic waves," *Journal of Engineering Mechanics*, vol. 123, no. 10, pp. 1060–1069, 1997.

[22] D. Dunavant, "High degree efficient symmetrical gaussian quadrature rules for the triangle," *International journal for numerical methods in engineering*, vol. 21, no. 6, pp. 1129–1148, 1985.

[23] S. T. Grilli, J. Skourup, and I. A. Svendsen, "An efficient boundary element method for nonlinear water waves," *Engineering Analysis with Boundary Elements*, vol. 6, no. 2, pp. 97–107, 1989.

[24] J. Harris, E. Dombre, A. Mivehchi, M. Benoit, S. Grilli, and C. Peyrard, "Progress in fully nonlinear wave modeling for wave-structure interaction," *Proceedings of the 15th Journée de lHydrodynamique*, p. 12, 2016.

[25] R. Yokota, J. P. Bardhan, M. G. Knepley, L. A. Barba, and T. Hamada, "Biomolecular electrostatics using a fast multipole BEM on up to 512 GPUs and a billion unknowns," *Computer Physics Communications*, vol. 182, pp. 1272–1283, 2011.

[26] R. Yokota, "An FMM based on dual tree traversal for many-core architectures," *J. Algorithms and Computational Tech.*, vol. 7, pp. 301–324, 2013.

[27] C. Fochesato, S. Grilli, and P. Guyenne, "Note on non-orthogonality of local curvilinear co-ordinates in a three-dimensional boundary element method," *International journal for numerical methods in fluids*, vol. 48, no. 3, pp. 305–324, 2005.

[28] I. H. Abbott and A. E. Von Doenhoff, *Theory of wing sections, including a summary of airfoil data.* Courier Corporation, 1959.

[29] J. Maestre, I. Cuesta, and J. Pallares, "An unsteady 3d isogeometrical boundary element analysis applied to nonlinear gravity waves," *Computer Methods in Applied Mechanics and Engineering*, vol. 310, pp. 112–133, 2016.

MANUSCRIPT 3

Identification and individual energy absorption of breaking waves in 3D fully nonlinear BEM simulations

by
A.Mivehchi[1],S.T. Grilli[1],J.M. Dahl[1],
J. C. Harris[2], K. Kuznetsov[2], C.M. O'Reilly[1]

(1) Dept. of Ocean Engineering, University of Rhode Island, Narragansett, RI 02882,

USA
(2) LHSV, Ecole des Ponts, CEREMA, EDF R&D, Université Paris-Est, Chatou, France

Abstract

A 3D fully nonlinear Numerical Wave Tank (NWT), accelerated with Fast Multipole Method (FMM), is extended to include spilling breaker model, which utilize an absorbing surface pressure that is specified over region where breaking wave exist. A spilling breaker generated due to an advancing submerged hydrofoil is modelled to to demonstrate the method. The instantaneous power dissipated for each breaking wave by the absorbing pressure is specified proportional to the average dissipation of steady spilling breakers found by Duncan [1, 2]. The method is implemented by applying a wave tracking algorithm to the free surface. A geometrical breaking criteria of maximum surface slope (for long low frequency waves) and maximum curvature (for short high frequency waves) is used to identify breaking waves on the surface. Computations for a wave breaking induced by towed foil is compared with experiment with the goal of stabilizing the simulation of NWT. The agreement with experiments is good, and model is extended to demonstrate applications with more complex free surface breaking.

3.1 Introduction

In the past few decades, numerical models based on irrotational (and thus kinematically inviscid) potential flow theory, with fully nonlinear free surface boundary conditions, have proved very accurate (as compared to experiments) for simulating steep waves in two- or three-dimensions (2D/3D) and in deep/intermediate or shallow water, up to the point of breaking, without or in the presence of fixed or moving surface-piercing structures. When using an Eulerian-Lagrangian (EL) free surface time updating, these models could also accurately simulate wave overturning up to the time a breaker jet impacted the free surface [3, 4, 5, 6, 7, 8, 9, 10, 11, 12, 13, 14, 15, 16, 17, 18]. In most of these studies, the so-called Fully Nonlinear Potential Flow (FNPF) equations were solved using a

higher-order Boundary Element Method (BEM), combined with a high-order time updating algorithm (EL or Eulerian). A BEM was deemed more accurate and efficient to use for this problem than domain discretization methods, particularly since the main results of interest often were located on boundaries. For 3D problems, however, to overcome the penalizing numerical complexity of standard BEM methods–usually N^2, for N boundary nodes–*fast multipole methods* (FMM) were introduced that yielded a nearly order N solution [19, 20, 13, 14, 15, 21, 22, 23].

Despite their accuracy and efficiency, FNPF-BEM simulations have the important limitation that both the modeled physics and computations break down whenever a wave reaches the breaking point and/or overturns, which can happen anywhere in the domain for complex/irregular sea states, due to wave-wave interactions or the bathymetry, as well as around surface piercing fixed or moving structures (e.g., breaking bow waves of advancing ships). Nevertheless, many important properties of waves near and at the onset of breaking were and are still studied with such models [24, 9, 10, 12, 18], as they often provide more accurate and efficient results near and at the free surface (both geometry and flow fields) than full Navier-Stokes (NS) CFD codes. However, the occurrence of breaking prevents performing longer term or practical engineering FNPF simulations, which requires implementing a method for identifying and suppressing wave breaking in these models. The latter can be achieved by removing energy from waves that are deemed to be at the onset of breaking, but as there is no physical dissipation mechanism in potential flow theory, this can only be achieved by specifying dissipation terms in the free surface boundary conditions, which govern the wave kinematics and dynamics. Such methods have been extensively applied in earlier studies to specify so-called *absorbing beaches* (AB; or sponge layers), for instance to dissipate all waves at the end or on the sides of a *Numerical Wave Tank* (NWT) [25, 26].

NWTs, which are equipped with the same functionality as physical wave tanks, i.e., wave generation by a variety of wavemakers or other methods and wave absorption in ABs [26, 27], have increasingly become standard design tools in ocean/offshore engineering and naval hydrodynamics, to study wave-structure interactions (see [15] for a review of NWT).

In earlier work the authors implemented an AB in their 2D- and 3D-NWT, by specifying a *damping surface pressure* p_{AB} in the dynamic free surface boundary condition, which they defined as proportional and opposite to the local normal particle velocity; it can be shown that this always yields a negative work against waves and thus causes energy absorption (see details in [26]). To better absorb long wave energy they also modeled an active piston absorber at the end of the AB, as suggested in [28]. This *ad hoc* approach works well when the physics of the problem (e.g, nearshore wave shoaling) makes it clear in which area wave breaking will occur (e.g., a well-delimited surfzone), and one is not seeking to accurately model the physics of steep wave trains, within which some individual waves could break. By contrast, to study individual shoaling and breaking surfzone waves, Guignard and Grilli [29] implemented a local *spilling breaker* (SB) model in their 2D-NWT, based on the same principle as the AB, in which impending breaking waves were first identified based on a maximum front slope criterion (37 deg in this case), and then had their energy gradually absorbed by specifying a Gaussian distributed absorbing pressure in the area of the wave crest. Assuming a roller model, the rate of energy dissipation was adjusted to match that of an inverted hydraulic jump having the same height and crest celerity, which other work has shown is a good proxy for energy dissipation in spilling breaking waves [30, 31, 32]. With this approach, Guignard and Grilli (2001) were able to simulate the decay of periodic wave elevations and the related wave set-up in a surfzone, in good

agreement with laboratory experiments.

Here we report on the development, implementation, and validation of a similar local wave breaking identification and absorption method, in the 3D-FNPF-FMM-BEM NWT developed in our earlier work [11, 33, 15, 22, 23, 17]. Although this method is general, in this paper, we target ocean and naval engineering applications, in which one seeks to accurately compute motions and induced forces on structures due to steep waves, as a function of time, without simulations being interrupted by wave breaking in the wake or near structures. As we are not interested in estimating near breaking wave properties, although the amount of energy absorbed in the model to prevent breaking should be calibrated to be physically meaningful, the details of energy absorption and in particular of its distribution around wave crests are not key to the result accuracy. An algorithm is first applied to identify areas of impending breaking waves in instantaneous free surface elevations. For complex sea states that are possibly strongly affected by the presence of structures, this is not a trivial problem. The algorithm works in three stages: (i) A Hilbert transform method first identifies wave crest and trough locations [34]; then, (ii) based on local wave properties, breaking criteria are applied, based on maximum slope and/or curvature thresholds to identify near breaking wave areas [29, 35]; finally, (iii) absorbing pressure patches are distributed over these areas.For the later stage, calibration of the dissipation rate is necessary to be physically meaningful.

Perlin et al. [36] gave a review to date of breaking criteria for waves in deep to intermediate depth. Deep water breaking criteria have typically been based on maximum wave steepness thresholds, such as Miche's criterion for 2D periodic waves, $S = ka > 0.443$ (with a the wave amplitude, $k = 2\pi/\lambda$ the wavenumber, and λ the wavelength), which corresponds to the wave crest having a 120 deg.

angle. Such criteria have been adapted to irregular sea states by using the total steepness, $S_t = \sum_i k_i a_i$ (in which a large number of wave harmonics i are used). As S or S_t increases, so does nonlinearity, causing the geometry of individual waves to become increasingly horizontally asymmetric, with narrower and steeper crests and longer shallower troughs; additionally waves exhibit an increasing fore-aft asymmetry, which can be enhanced by the presence of a sloping bottom. In the latter case, as depth decreases, breaking criteria have more typically been of the form of a maximum breaker index, $\gamma = a/h$ whose value is usually function of the wave incident steepness in deep water S_0 and the local bottom slope [9]. In deep water, maximum steepness values used in breaking criteria have typically been in the 0.31-0.7 range, depending on wave type, with 0.35 being most often selected [36]. Hence, there does not seem to be a unique limiting wave steepness.

This fact was confirmed in recent studies, which showed that single S, S_t, or γ threshold values do not uniquely separate breaking and non-breaking waves [37, 38, 18]. In an attempt to unify these approaches, these studies proposed a kinematic breaking criterion, a function of the local particle velocity at the crest u_c and celerity c, of the form $B = u_c/c > 0.85 - 0.86$, which they showed appeared to be universal for many different types of waves, in 2D or 3D and for a variety of depth regimes [37, 38, 18]. More specifically, unlike the traditional breaking criteria, waves do not break when reaching this threshold B value, but instead, any wave that crosses it will end up breaking, whereas those that do not, while first steepening, will recover without breaking. Additionally, using a NS model, the same work showed that the total energy dissipation in breaking waves is proportional to dB/dt calculated for the threshold value and to a relevant time scale. Hence, the steeper the rise of B towards its threshold, the larger the eventual wave dissipation.

As indicated before, it is not our purpose here to investigate the physics of near-breaking waves, but instead to develop and apply the *ad hoc* algorithm introduced above for wave breaking suppression in FNPF-NWT simulations. However, we still want the absorbed breaking wave energy to be physically realistic. Kinematic breaking criteria, such as those based on B, while being most accurate, require computing instantaneous values of the horizontal particle velocity at the crest u_c as well as the crest phase speed, c. While the horizontal particle velocity on the free surface $U = (u, v)$ is locally computed in the NWT, and can then be projected in the direction normal to a wave crest that has been identified in the algorithm, the crest celerity is non local and requires tracking crest trajectories as a function of time for long enough to be able to accurately compute the local phase velocity by time differentiation. In their 2D-FNPF-NWT, Grilli and Guignard [29] tracked the motion of individual waves in their simulations of shoaling periodic waves. Based on these wave kinematics, they could apply a simple shallow water breaking criterion–in their case a maximum front slope reaching 37 deg–to detect impending breaking waves. Using the individual wave properties, such as c, and crest/trough elevation, the energy dissipation for each individual breaking wave was estimated and an absorbing pressure p_d was accordingly applied in the BEM code.

In the more complex 3D situations considered in present paper, we elected to apply simpler local breaking criteria in our *ad hoc* algorithm, based on the wave crest front slope and/or curvature reaching a maximum value. Details will be provided later, but in past work, Subramani et al. [35] had demonstrated using a breaking criterion in their 3D-FNPF model based on the local wave curvature κ of the form $\kappa_b a > 0.35$. Surface curvature can easily be computed in curvilinear BEM elements [33]. Regarding energy dissipation rates, the energy extracted by

the damping pressure from waves identified to break in the model will be calibrated based on the parameterization derived by Duncan [1, 2] from results of experiments for steady breaking waves induced by a submerged towed hydrofoil. He found that the energy dissipation rate per unit width of crest in each breaking wave varied as, $\epsilon_b = b\rho\, c_b^5/g$ (in Watts), where ρ is water density, g is the gravitational acceleration, and c_b is the breaking wave crest celerity. Based on these experiments, Duncan derived values of the non-dimensional breaking parameter $b \in [0.036 - 0.052]$, as a function of the front slope of breaking waves in the range [10-14.7] deg.

In the following, in section 2 we briefly describe the FNPF model governing equations and boundary conditions, and the mathematical formulations associated with the breaking suppression model, including breaking criteria, wave energy absorption, and wave crest/track identification and tracking algorithms. In section 3, we briefly summarize the numerical model implementation and methods, which have all been detailed elsewhere, in Section 4, we present results of numerical simulations and their validation with Duncan's experiments for steady breakers, and we conclude with a discussion and conclusions in Section 5.

3.2   Model equations
3.2.1   Governing Equation and Boundary Conditions

We model irrotational flows of an incompressible and inviscid fluid, for which flow velocity is given by $\mathbf{u} = \boldsymbol{\nabla}\phi$, with $\phi(\mathbf{x}, t)$ the velocity potential. In Cartesian coordinates, the position vector is defined as $\mathbf{x} = (x, y, z)$, in which z is pointing vertically upwards and gravity is pointing downward, with acceleration g. Such *potential flows* are governed by mass conservation, which yields a Laplace's equation for the velocity potential,

$$\nabla^2\phi = 0 \quad \text{in} \quad \Omega(t) \tag{41}$$

over domain $\Omega(t)$ with boundary $\Gamma(t)$. In the context of the BEM, using Green's second identity, this governing equation is transformed into a Boundary Integral Equation (BIE),

$$\alpha(\mathbf{x}_l)\phi(\mathbf{x}_l) = \int_{\Gamma(\mathbf{x}(t))} \left\{ \frac{\partial \phi}{\partial n}(\mathbf{x})G(\mathbf{x}, \mathbf{x}_l) - \phi(\mathbf{x})\frac{\partial G}{\partial n}(\mathbf{x}, \mathbf{x}_l) \right\} d\Gamma(\mathbf{x}(t)) \qquad (42)$$

in which $\mathbf{x}$ and $\mathbf{x}_l = (x_l, y_l, z_l)$ are points on boundary $\Gamma(t)$, $\mathbf{n} = (n_x, n_y, n_z)$ is the unit outward normal vector on the boundary, and $\alpha(\mathbf{x}_l)$ is a geometric coefficient function of the interior angle of the boundary at $\mathbf{x}_l$. The 3D free space Green's function and its normal derivative are defined in the BIE as,

$$G(\mathbf{x}, \mathbf{x}_l) = \frac{1}{4\pi r} \quad \text{and} \quad \frac{\partial G}{\partial n} = -\frac{\mathbf{r} \cdot \mathbf{n}}{4\pi r^3} \qquad (43)$$

in which $\mathbf{r} = \mathbf{x} - \mathbf{x}_l$ and $r = |\mathbf{r}|$.

On the free surface $\Gamma_f(t)$, ϕ satisfies the nonlinear kinematic and dynamic boundary conditions,

$$\frac{\delta \zeta}{\delta t} = \frac{\partial \phi}{\partial z} - \mathbf{\nabla}_H \phi \cdot \mathbf{\nabla}_H \zeta - \mathbf{U}(t) \cdot \mathbf{\nabla}_H \zeta \qquad \text{on} \qquad \Gamma_f \qquad (44)$$

$$\frac{\delta \phi}{\delta t} = -g\zeta - \frac{1}{2}\mathbf{\nabla}\phi \cdot \mathbf{\nabla}\phi - \frac{p_a}{\rho} + \frac{\partial \zeta}{\partial t}\frac{\partial \phi}{\partial z} - \mathbf{U}(t) \cdot \mathbf{\nabla}_H \phi \quad \text{on} \qquad \Gamma_f \qquad (45)$$
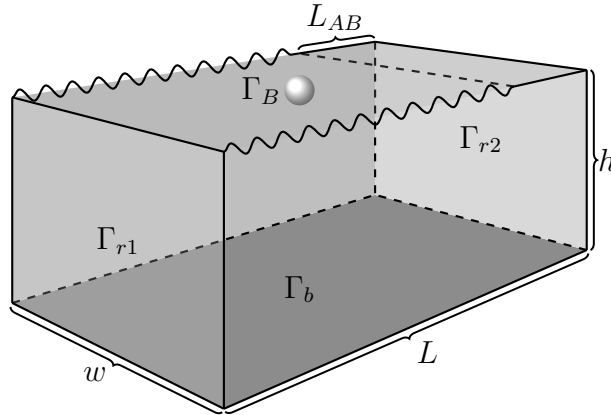
Figure 17: NWT computational domain. Waves, if any, are generated on Γ_{r1} and damped in the absorbing beach (AB) over length L_{AB}, and on Γ_{r2} using an absorbing piston.

respectively, with ζ the vertical position vector of nodes on the free surface (referred to $z = 0$ and measured upward), p_a the atmospheric pressure, ρ the fluid density, and the horizontal derivative, $\boldsymbol{\nabla}_H = \frac{\partial}{\partial x}\mathbf{i} + \frac{\partial}{\partial y}\mathbf{j}$ ($\mathbf{i}$ and $\mathbf{j}$ are unit vector in directions x and y, respectively).

Eqs. 79 and 80 have been expressed in a semi-Lagrangian form [39, 40, 14], assuming that the coordinate system advances at velocity $\mathbf{U}(t)$, and the semi-Lagrangian derivative is defined as,

$$\frac{\delta}{\delta t} = \frac{\partial}{\partial t} + \frac{\partial \zeta}{\partial t}\frac{\partial}{\partial z} - \mathbf{U}(t) \cdot \boldsymbol{\nabla}_H \tag{46}$$

In the NWT, waves can be generated by simulating a wavemaker motion or incident wave kinematics on boundary $\Gamma_{r1}(t)$ and damped in an absorbing beach (AB) over length L_{AB}, and/or on Γ_{r2} using an absorbing piston (Fig. 28) [26]. For instance, a simple piston wavemaker motion could be specified by its time dependent stroke and velocity (x_p, u_p) as,

$$\overline{x} = x_p(t); \qquad u_p(t) = -\boldsymbol{\nabla}\phi \cdot \mathbf{n} = -\overline{\frac{\partial \phi}{\partial n}} \qquad \text{on} \quad \Gamma_{r1}(t) \tag{47}$$

respectively, where the overlines denote specified values. Along the stationary bottom Γ_b and on other fixed boundaries, a no-flow condition is prescribed as (Fig. 28),

$$\overline{\frac{\partial \phi}{\partial n}} = 0 \qquad \text{on} \quad \Gamma_b, \ \Gamma_{r2} \tag{48}$$

The boundary condition along a rigid submerged or surface piercing ocean/naval structure, moving with velocity $\mathbf{V}_B$, would be specified as,

$$\overline{\frac{\partial \phi}{\partial n}} = \mathbf{V}_B \cdot \mathbf{n} \qquad \text{on} \quad \Gamma_B \tag{49}$$

As indicated before, incident waves are damped at the far end of the NWT by dissipating their energy in an *absorbing beach* (AB) of length L_{AB} (Fig. 28), over which a damping pressure term p_d is added to the dynamic free surface boundary

73
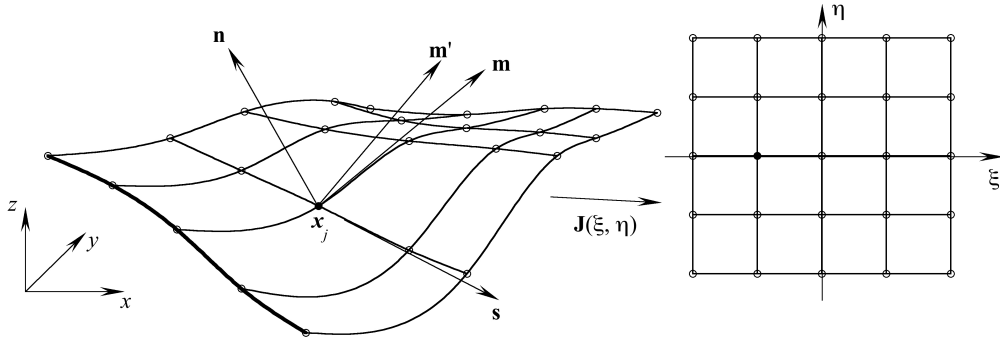
Figure 18: Definition of local non-orthogonal $(\mathbf{s}, \mathbf{m}, \mathbf{n})$ and orthogonal $(\mathbf{s}, \mathbf{m}', \mathbf{n})$ curvilinear coordinate systems used to compute tangential derivatives at collocation node $\mathbf{x}_j$ on the domain boundary; the transformation to intrinsic coordinates (ξ, η) by way of Jacobian $\mathbf{J}(\xi, \eta)$ is illustrated. The boundary is interpolated piecwise by cubic quadrilateral B-spline boundary elements. Symbols (o) mark collocation nodes and the thicker line a domain edge.

conditions; for long waves, an absorbing piston can also be specified over boundary Γ_{r2} [26, 28]. A similar damping pressure approach is used to absorb energy in individual waves that are identified to be near breaking. Details of the AB and local absorption methods are provided in a following section. Finally, small free surface oscillations that could appear upstream of a structure, as a result of the semi-Lagrangian time updating, are damped in a sponge layer specified near boundary Γ_{r1}, over which $-\nu(x)\zeta$ and $-\nu(x)\phi$ terms are added to the right hand side of the kinematic and dynamic boundary conditions, respectively [25]; within the sponge layer, the shape function $\nu(x)$ gradually increases with distance squared.

3.2.2 Boundary representation and curvilinear coordinate transformation

As will be detailed later, given N collocation nodes on the 3D-NWT boundary where problem unknowns are computed, the boundary geometry and field

variables are piecewise-interpolated in between those using cubic B-spline bound-ary elements, which ensure inter-element continuity of the surface slope. For the purpose of numerical integration in the BIE, these elements, whose shape functions are defined in the physical space (x, y, z) are each locally expressed using intrinsic coordinates (ξ, η), by way of a curvilinear coordinate transformation with Jacobian $\mathbf{J}(\xi, \eta)$ (Fig. 29).

Additionally, to apply some boundary conditions and specify energy absorp-tion in the model, tangential derivatives and curvature need to be computed at collocation points. This is done in a local curvilinear coordinate system $(\mathbf{s}, \mathbf{m}, \mathbf{n})$, which is not necessarily orthogonal and whose tangential vectors are defined as [11, 33] (Fig. 29),

$$\mathbf{s} = \frac{1}{h_1} \frac{\partial \mathbf{x}}{\partial \xi} \quad \text{and} \quad \mathbf{m} = \frac{1}{h_2} \frac{\partial \mathbf{x}}{\partial \eta}, \tag{50}$$

with,

$$h_1 = \left| \frac{\partial \mathbf{x}}{\partial \xi} \right|, \quad h_2 = \left| \frac{\partial \mathbf{x}}{\partial \eta} \right|. \tag{51}$$

Following Fochesato et al. [33] orthogonal tangential vectors $(\mathbf{s}, \mathbf{m}')$ are de-fined (Fig. 29) and used to compute both tangential derivatives. We have,

$$\mathbf{m}' = \frac{1}{\sqrt{1 - \chi^2}} \mathbf{m} - \frac{\chi}{\sqrt{1 - \chi^2}} \mathbf{s}, \tag{52}$$

with $\chi = \mathbf{s} \cdot \mathbf{m} \in [-1, 1]$, so that $\mathbf{s} \cdot \mathbf{m}' = 0$. With these definitions, the unit normal vector is defined as (Fig. 29),

$$\mathbf{n} = \mathbf{s} \times \mathbf{m}' = \frac{1}{\sqrt{1 - \chi^2}} \mathbf{s} \times \mathbf{m}, \tag{53}$$

and the Jacobian of the curvilinear coordinate transformation $(x, y, z) \rightarrow (\xi, \eta)$ as,

$$\mathbf{J}(\xi, \eta) = \left\{ \frac{\partial \mathbf{x}}{\partial \xi}, \frac{\partial \mathbf{x}}{\partial \eta}, \mathbf{n} \right\}^{\mathrm{T}}, \tag{54}$$

with $| \mathbf{J}(\xi, \eta) | = h_1 h_2$.

In this local orthogonal curvilinear system, the gradient operator is given by,

$$\boldsymbol{\nabla} \equiv \frac{\partial}{\partial s}\mathbf{s} + \frac{\partial}{\partial m'}\mathbf{m'} + \frac{\partial}{\partial n}\mathbf{n} \tag{55}$$

with,

$$\frac{\partial}{\partial s} = \frac{1}{h_1}\frac{\partial}{\partial \xi} \quad ; \quad \frac{\partial}{\partial m} = \frac{1}{h_2}\frac{\partial}{\partial \eta} \tag{56}$$

and

$$\frac{\partial}{\partial m'} = \frac{1}{\sqrt{1-\chi^2}}\frac{\partial}{\partial m} - \frac{\chi}{\sqrt{1-\chi^2}}\frac{\partial}{\partial s} \tag{57}$$

Hence,

$$\boldsymbol{\nabla} \equiv \left(\frac{\partial}{\partial s} - \chi\frac{\partial}{\partial m}\right)\mathbf{s} + \left(\frac{\partial}{\partial m} - \chi\frac{\partial}{\partial s}\right)\mathbf{m} + \frac{\partial}{\partial n}\mathbf{n} \tag{58}$$

3.2.3   Criteria to trigger wave breaking suppression in the NWT

As detailed in the introduction, many breaking criteria have been proposed in past studies, with most of these focusing on identifying wave characteristics at the breaking point. For the purpose of suppressing wave breaking in our FNPF-NWT, however, once wave parameters reach values defined in such a criteria, it is usually too late to absorb enough energy in the model to prevent wave breaking. Therefore, we have developed simpler and more conservative, yet physically meaningful, breaking criteria based on geometrical properties of the free surface. As discussed in the introduction these are based on surface slope, curvature, or a combination of both of these. Details are provided in the following.

Curvature-based criteria

Based on the piecewise cubic B-spline representation of the model boundary, the free surface curvatures can be computed at each collocation point in the local orthogonal curvilinear coordinate system defined earlier ($\mathbf{s}$, $\mathbf{m'}$, $\mathbf{n}$) (Fig. 29) as,

$$\kappa_s = \frac{\left|\frac{\partial^2 \mathbf{x}_j}{\partial s^2}\right|}{\left(1 + \left|\frac{\partial \mathbf{x}_j}{\partial s}\right|^2\right)^{\frac{3}{2}}} \quad , \quad \kappa_{m'} = \frac{\left|\frac{\partial^2 \mathbf{x}_j}{\partial m'^2}\right|}{\left(1 + \left|\frac{\partial \mathbf{x}_j}{\partial m'}\right|^2\right)^{\frac{3}{2}}} \tag{59}$$

in which the $s-$ and $m'-$derivatives are expressed based on the transformation introduced above (Eqs. 92 and 93).

Given an arbitrary direction $\mathbf{e}$, for instance orthogonal to an identified wave crest, using Eq. 94 one can compute the directional derivative as $\partial/\partial e \equiv \boldsymbol{\nabla}\cdot\mathbf{e}$ and the second derivative by applying this operator to itself [33]. As they are not defined within the surface, the n-derivative terms in this equation can be eliminated by also selecting $\mathbf{e}$ such that $\mathbf{e}\cdot\mathbf{n} = 0$, with $\mathbf{n}$ given by Eq. 89. The curvature κ_e can then be computed with an equation similar to those in Eq. 59 in which e is subsituted for s or m'. [One would as easily compute the local maximum (principal) curvature.] Estimating the local wave amplitude a, one can then check whether $\kappa_e a > \kappa_b a = 0.35$ and deem the wave to be about to break or not.

While this maximum curvature criterion has been shown to work well for short steep waves [35], for long waves, it may not be sufficiently conservative to allow *enough time* for suppressing wave breaking in the model. In this case, a maximum front slope criterion is more appropriate [29].

Slope-based criteria

Guignard and Grilli [29] used a 37 degree maximum slope criterion on the wave front face to identify whether long shoaling waves were about to break and trigger wave breaking suppression in their 2D-NWT. To apply a similar criterion in the present 3D-NWT, one needs to calculate the free surface slope in an arbitrary direction $\mathbf{e}$ (for instance orthogonal to an identified wave crest).

As detailed above, the surface slope in direction $\mathbf{e}$ can be calculated for any collocation point as, $|\partial\mathbf{x}_j/\partial e| \equiv |\boldsymbol{\nabla}\mathbf{x}_j\cdot\mathbf{e}|$, with the gradient operator given by Eq. 94 and the tangential $s-$ and $m/m'-$derivatives calculated with Eqs. 92 and 93 based on the B-spline basis functions. If $\mathbf{e}$ is further selected within a plane orthogonal to the local normal vector $\mathbf{n}$ (given by Eq. 89), the $n-$derivative terms

cancel and one can easily compute the surface slope $|\partial \mathbf{x}_j/\partial e|$ only based on the surface geometry; the latter can then be corrected with respect to the horizontal plane.

3.2.4   Wave energy absorption

In the model, the same method is used for damping waves in the absorbing beach (AB; Fig. 29) and in local areas where waves are deemed to be about to break, based on the breaking criteria detailed before. This is done by absorbing part of the wave energy by specifying a counteracting or *damping* surface pressure, p_{AB} or p_d, respectively, in the dynamic free surface boundary condition Eq. 80,

$$\frac{\delta\phi}{\delta t} = -g\eta - \frac{1}{2}\boldsymbol{\nabla}\phi \cdot \boldsymbol{\nabla}\phi + \frac{\partial\eta}{\partial t}\frac{\partial\phi}{\partial z} - \mathbf{U}(t) \cdot \boldsymbol{\nabla}_H\phi - \frac{p_a + p_{AB} + p_d}{\rho} \quad \text{on} \quad \Gamma_f \quad (60)$$

proportional to the normal particle velocity on the free surface [26],

$$p_{AB} = \nu_{AB}(\mathbf{x})\frac{\partial\phi}{\partial n} \quad ; \quad p_d = \nu_d(\mathbf{x})\frac{\partial\phi}{\partial n} . \quad (61)$$

In the AB, p_{AB} is smoothly ramped up at the beginning of the beach using the spatially varying function, $\nu_{AB}(\mathbf{x}) = \nu_0((x - x_{AB})/L_{AB})^2$ (Fig. 29), where ν_0 is the AB calibration coefficient, and is zero otherwise [26].

Likewise, in local *wave breaking areas*,

$$\nu_d(\mathbf{x}) = \nu_{b0}\rho\sqrt{gh_0}\,S_b(\mathbf{x}) \quad (62)$$

where h_0 is a reference depth, given a small ε value (e.g., 1%),

$$S_b(\mathbf{x}) = \frac{\text{sech}^2(\mu|\mathbf{x} - \mathbf{x}_b|) - \varepsilon}{1 - \varepsilon} \quad ; \quad \mu = \text{acosh}\sqrt{1/\varepsilon} \quad (63)$$

is an axisymmetric Gaussian-like function [29] smoothly decreasing from 1 to 0 over distance $|\mathbf{x} - \mathbf{x}_b|$, from the location where breaking is identified $\mathbf{x}_b$ (where the wave curvature/slope exceeds the defined threshold), and $S_b = 0$ beyond distance l_b.

Coefficient ν_{b0} is a calibration constant, which is calculated piecewise (i.e., for each breaking wave) based on matching the power dissipated over a single breaking wave area with that computed in Duncan's experiments for steady breakers, $\epsilon_b = b\rho\, c_b^5/g$ [1, 2] (see introduction). Thus, using Eqs. 62 and 63, the power dissipated by the damping pressure in a single breaking wave can be calculated as [26],

$$P_d = \int_{A_b(\mathbf{x})} p_d \frac{\partial \phi}{\partial n} \mathrm{d}A = \nu_{b0}\rho\sqrt{gh_0} \int_{A_b(\mathbf{x})} S_b(\mathbf{x}) \frac{\partial \phi}{\partial n} \mathrm{d}A = \epsilon_b \tag{64}$$

where $A_b(\mathbf{x})$ denotes the area where the damping pressure is specified around location $\mathbf{x}_b$ and the breaking wave crest celerity c_b in the expression of ϵ_b is found from model results (details are provided later). Hence,

$$\nu_{b0} = \frac{b\, c_b^5}{g\sqrt{gh_0}} \frac{1}{\mathcal{I}_b} \tag{65}$$

where $\mathcal{I}_b$ denotes the last integral in Eq. 64. Note, in practice, there are typically multiple neighboring collocation nodes where the breaking criterion is met for a given wave and, hence, this integral is computed over the sum of these areas and for the sum of the corresponding pressure shape functions S_b. Additionally, once the breaking criterion is met and a given area is identified to be applied the damping pressure p_d, calculated based on Eqs. 61 to 65, to prevent triggering numerical instabilities the pressure is ramped up over 5 time steps, from 0 to its target value using a tanh function.

In these experiments for steady breakers, based on measured dissipation, Duncan [1, 2] parameterized, $b = 0.009/\sin(\beta_b)$, with $\beta_b \in [10^o, 14.7^o]$ the average angle of the breaking wave front face. Hence, in these results $b \in [0.036-0.052]$, an interval which will be the basis for calibrating ν_{b0} with Eqs. (64) and 65 in the present applications.

3.2.5 Wave crest/trough identification and tracking algorithm

At each time t, an algorithm is applied to identify areas of impending breaking from instantaneous free surface elevations, which works in three stages: (i) a Hilbert transform method is applied to identify wave crest and trough locations, as well as compute crest celerity [34]; (ii) near breaking wave areas are identified based on local wave properties: maximum slope and/or curvature criteria (as detailed above); and (iii) absorbing pressure patches are distributed over these areas (as also detailed above). In the following, we detail stage (i) of this algorithm.

Stansell et al. [34] used spatial and temporal Hilbert transforms to calculate local wave phase speeds, based on computed wavenumbers k and frequencies ω. In the present algorithm, at each time t, locations of wave crests and troughs are identified by applying a spatial Hilbert transform to instantaneous surface elevations $\zeta(\mathbf{x}, t)$. A temporal Hilbert transform is also applied over the last τ time step (here 30 time steps) of nodes on the free surface which has been saved during the simulation. This allows computing wave crest celerity at the determined crest location over the free surface.It should be noted that for the non-global extrema, this value will be negative, resulting in negative phase speed which is not physical. For avoiding such abnormalities, only global exterma have been considered for calculating the temporal Hilbert transform. In 1D, both of these Hilbert transforms, in direction x and time t are defined as,

$$\mathcal{H}_x[\zeta(x,t)] = \frac{1}{\pi} P \int_{-\infty}^{\infty} \frac{\zeta(x',t)}{x-x'} \, \mathrm{d}x' \quad ; \quad \mathcal{H}_t[\zeta(x,t)] = \frac{1}{\pi} P \int_{-\infty}^{\infty} \frac{\zeta(x,t')}{t-t'} \, \mathrm{d}t' \qquad (66)$$

in which, P stands for the Cauchy principal value of the integral. [Note that small local extrema that occur above and below the still water level are filtered out.] Wave phases are then expressed as,

$$\varphi_x(x,t) = \mathrm{atan}\left\{\frac{\mathcal{H}_x[\zeta(x,t)]}{\zeta(x,t)}\right\} \quad ; \quad \varphi_t(x,t) = \mathrm{atan}\left\{\frac{\mathcal{H}_t[\zeta(x,t)]}{\zeta(x,t)}\right\}, \qquad (67)$$

for the spatial and temporal transformations, respectively. The roots of φ_x will yield locations of wave crests (or troughs), while crest celerity will be found as,

$$c_c = \frac{\partial \varphi_t}{\partial t} \left\{ \frac{\partial \varphi_x}{\partial x} \right\}^{-1} \tag{68}$$

which can be expressed as a function of ζ, $\mathcal{H}_x$, $\mathcal{H}_t$, and their spatial and time derivatives, respectively [34].

Eqs. 66 are equivalent to convolutions of functions $1/(\pi x)$ or $1/(\pi t)$ and $\zeta(x,t)$, which provides an efficient means of computing Hilbert transforms. For instance, considering the spatial Hilbert transform, the convolution in Eq. 66 is expressed in the wavenumber domain k using a discrete Fast Fourier Transform (FTT),

$$\mathcal{F}\{\mathcal{H}_x[\zeta(x,t)]\} = -i\,\mathcal{F}\{\zeta(x,t)\}\,\mathsf{sgn}(k) \tag{69}$$

where $\mathcal{F}\{1/x\} = -i\,\mathsf{sgn}(k)$ has been used. Then an inverse discrete FFT is applied to calculate the Hilbert transform as,

$$\mathcal{H}_x[\eta(x,t)] = \mathcal{F}^{-1}\{-i\,\mathcal{F}\{\eta(x,t)\}\,\mathsf{sgn}(k)\}. \tag{70}$$

A similar method can be applied to computing $\mathcal{H}_t$. [Note, a Hilbert transform is similar to a low pass filter and, hence, its cutoff frequency must be set to satisfy the Nyquist limit, to avoid aliasing, which would result in the false identification of wave crests. This can be done by zero padding the free surface elevation signal used in the Hilbert transform,which has the effect of increasing the number of frequncy bins in the Fourier transform.] This 1D method is extended to 2D as detailed below.

In the 3D-NWT, since the Hilbert transform is a 1D operator, at each time t the free surface elevation $\zeta(x,y,t)$ is divided into N_s slices (e.g., with N_s the number of nodes in the NWT width direction), to which the Hilbert transforms of Eq. 66 are applied. The roots of the phase function φ_x thus provide locations

81
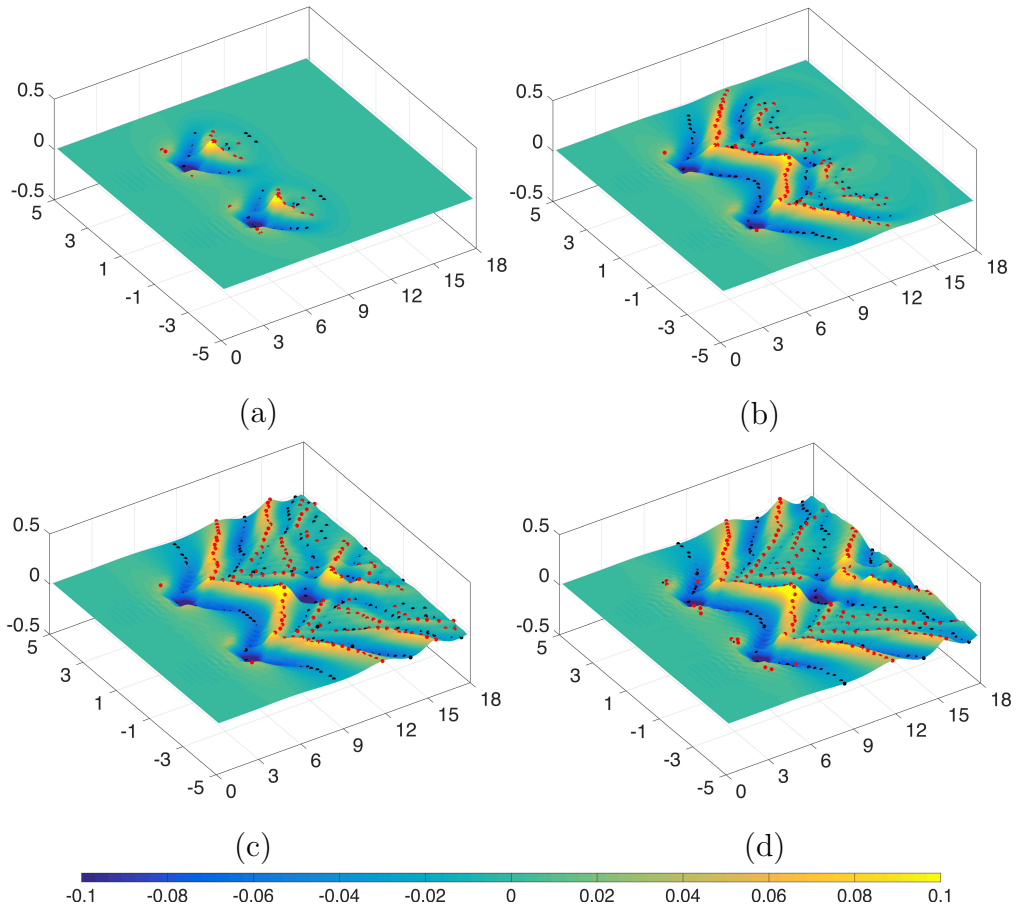
Figure 19: Evolution of Free surface elevation $\zeta(\mathbf{x}, t)$ in the wake of advancing twin pressure patches computed in the 3D-FNPF-NWT at times of $t\sqrt{g/h}$ for (a) 5;(b) 10;(c) 15 and (d) 20; location of extrema in wave free surface elevation identified using Hilbert transform method. The crests are marked by ($\bullet$) and the troughs are marked by ($\bullet$).
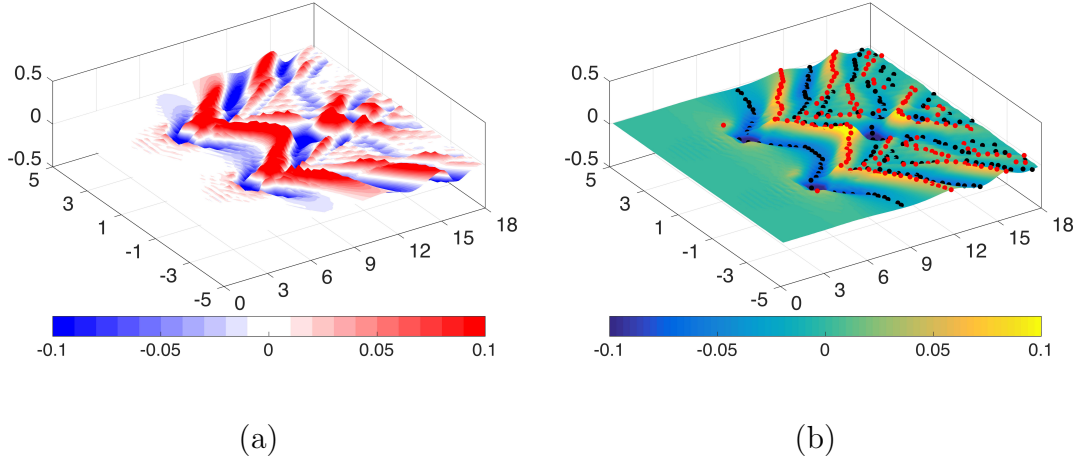
Figure 20: Application of the wave tracking CDS algorithm to the computed wake of advancing twin pressure patches. (a) Normal velocity $\partial\phi/\partial n$; and (b) identified wave crests ($\bullet$) and troughs ($\bullet$). As expected at the location of extrema in the wake the values of $\partial\phi/\partial n = 0$

of troughs (zero up-crossing) and crest (down-crossing) in each free surface slice. [Note, besides identifying locations of free surface extrema, this method allows computing local values of the wave crest and trough elevations.] Figs. 19 and 20 show an example of applying this method to identifying wave crests and troughs in the computed wake of advancing twin pressure patches, an application that is detailed later in the paper. In Fig. 20b, the identified locations of crests and troughs are consistent with the areas where $\partial\phi/\partial n = 0$ shown in Fig. 20a (white areas in between red and blue areas), which is to be expected [29].

The phase speed of breaking wave crests c_b, which is required to quantify the dissipated energy (Eq. 65), is first computed in the direction of each slice using Eq. 68 and then projected in the direction normal to the local wave crest. To do so, wave crests are identified in the 2D free surfaces with an algorithm based on a divide and conquer strategy (DCS). When the breaking criteria is met at a given location $\mathbf{x}_b$, the algorithm first identifies other nodes that are also breaking on or near the same crest in the computational grid, which allows defining the

spatial variation of the damping pressure p_d (i.e., the shape functions $S_b(\mathbf{x})$ used for energy absorption; Eq. 63), and the local breaking area to be integrated over to compute $\mathcal{I}_b$ (Eq. 64). Then, neighboring crest points $\mathbf{x}_c^i$ ($i = 1, ...$) that are close to $\mathbf{x}_b$ are located by applying the DCS algorithm to results of the spatial Hilbert transform (e.g., Fig. 19b), allowing identification of the normal direction to the local crest and computation of c_b.

In the application of the damping pressure, when the damping regions of neighboring points overlap, the absorbing pressure patch of the closest breaking point is used. A given absorbing patch is then kept active until the breaking criteria is no longer locally met.

3.3   Numerical methods

In the 3D-NWT, Eq. (77) is solved by a higher-order Boundary Element Method (BEM) [11], in which N collocation nodes are defined on the boundary and M boundary elements are used to interpolate in between these nodes. In the present model, cubic quadrilateral B-spline elements are used on each part of the boundary [41, 42, 43, 44, 45, 23, 17], which ensures continuity of the inter-element slope (Fig. 29); this property is key to accurately simulate steep nonlinear waves on the free surface [8, 12]. In B-spline elements, both geometry and field variables are interpolated for each quadrilateral using the bi-linear combination of two one-dimensional 4-node cubic B-splines, defined around each pair of nodes along each horizontal direction. Expressions of BEM integrals for higher-order elements (regular, singular, quasi-singular) and details of their numerical integration can be found in [11]. Multiple nodes (double, triple) are specified at corners and edges of the computational domain (Fig. 28) [46], over which the velocity potential and the uniqueness of the velocity vector is specified. Grilli and Subramanya [8] introduced and validated this method in their 2D-NWT and showed it was important

to ensure a good accuracy of the FNPF solution as well as prevent sawtooth in-stabilities near solid boundaries. Mivehchi et al. [47] extended this method to 3D in the context of the B-spline representation of the geometry.

The 3D-NWT solution is accelerated by using an efficiently parallelized Fast Multipole Method (FMM) that allows achieving a numerical complexity $\simeq \mathcal{O}(N)$ and a good scalability on medium or large multi-CPU computer clusters. With the FMM, when assembling the BEM algebraic system [11], the Green's functions in BIE integrals performed over boundary elements that are "distant enough" from the considered collocation point are approximated by polynomial functions, of decreasing order with distance, that only depend on an average distance to the element. Hence, this both simplifies integrations and contributions of boundary parts beyond some cutoff distance yielding a sparse algebraic system matrix. With the FMM, the full system matrix of the BIE does not have to be assembled, which is typically one of the most time consuming parts of the BEM solution, as it has $\mathcal{O}(N^2)$ numerical complexity similar to that of the best iterative solvers. More specifically, to decide how to approximate (or even neglect) contributions of specific elements, the FMM uses a DCS based on the distance between two points. Importantly, by assigning intermediate points (e.g., the centers of groups of nodes or elements of the boundary mesh) and applying the binomial theorem, one is able to manipulate multipole coefficients that only need to be computed once, instead of directly evaluating the BIE between each element and node (see Harris et al. [22, 23, 17]). Theoretically, if efficiently implemented and assuming N is more than a few thousand, the computational time of the FMM scales with $\simeq \mathcal{O}(N)$ [48],[49].

At any given time, the BEM solution provides both the velocity potential and its normal derivative on the computational domain boundary, as discrete values at

the N collocation points. This solution (both geometry and boundary condition) is then advanced in time on the free surface by integrating the two free surface boundary conditions, Eqs. (79) and (80). Here, a semi-Lagrangian approach is used on the free surface [39, 14], in which points are fixed in the horizontal direction and, although more complex schemes have been used in past work [11], a simple third-order Runge-Kutta scheme is used for time updating of ϕ and ζ, which can be written compactly as,

$$
\begin{aligned}
f^{(1)} &= f^{(n)} + \Delta t(\delta_t f^{(n)}) \\
f^{(2)} &= \frac{3}{4} f^{(n)} + \frac{1}{4} \left(f^{(1)} + \Delta t(\delta_t f^{(1)}) \right) \\
f^{(n+1)} &= \frac{1}{3} f^{(n)} + \frac{2}{3} \left(f^{(2)} + \Delta t(\delta_t f^{(2)}) \right)
\end{aligned}
\tag{71}
$$

with Δt the time step. One advantage of this semi-Lagrangian approach is that for vertical walled structures (e.g., cylindrical), there is no complex remeshing required as the free surface is updated (see [17] for details).

At each time step, global accuracy of computations can be assessed by computing errors in total volume and, in some case, energy for the generated wave train. In their Eulerian-Lagrangian time updating method, Grilli and Subramanya [8] in 2D and Grilli et al. [11] in 3D showed that these errors are function of both the size (i.e., distance between nodes) and the degree (i.e., quadratic, cubic,...) of boundary elements used in the spatial discretization, and of the size of the selected time step. They proposed a method for adaptively selecting the optimal time step, based on a mesh Courant number $C_o(t)$. For the MII(Mid Interval Interpolation) elements, they showed that the optimum value of C_o is around 0.45. This value is also used in the present applications and, since nodes are not free to move horizontally, this value is essentially maintained constant throughout computations.
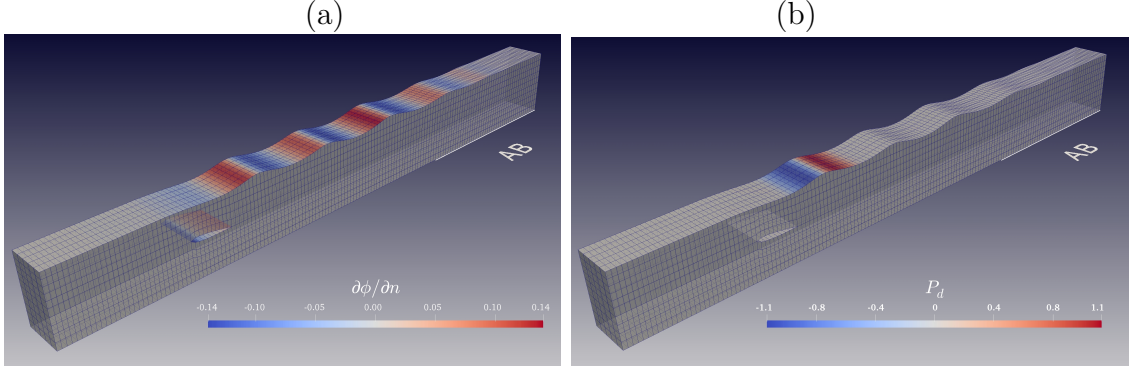
Figure 21: Simulation of Duncan experiment in the 3D-NWT for $d = 0.159$ m, which causes steady breaking of the first (largest) wave in the train. (a) Boundary grid with values of $\partial\phi/\partial n$ plotted on the free surface as color scale (red positive and blue negative); (b) Same grid with values of damping pressure p_d plotted on the free surface as color scale (red negative and blue positive).

3.4 Applications
3.4.1 2D breaking induced by an advancing submerged hydrofoil

The breaker model is first validated by comparing numerical simulations to results of Duncan's [1, 2] laboratory experiments. In these quasi-2D experiments a NACA 0012 hydrofoil (of chord length $C = 0.203$ m) was submerged at depth d, angled at 5 deg, and towed from rest up to a maximum speed $V_{Bm} = 0.8$ m/s in a tow tank, 24 m long, 0.61 m deep and 0.61 m wide (Fig. 21). Upon reaching steady state, the hydrofoil caused the generation of a stationary decaying wave train. For small enough submergence d, the first (larger) wave broke as a stationary spilling breaker.

For simplicity in the numerical simulations, the geometry was scaled with characteristic length C, yielding the dimensional and non-dimensional (primed) variables [14],

$$x' = \tfrac{x}{C}, \quad y' = \tfrac{y}{C}, \quad z' = \tfrac{z}{C}, \quad t' = t\sqrt{\tfrac{g}{C}}, \quad g' = 1$$

$$\mathrm{Fr} = \tfrac{V_{Bm}}{\sqrt{gC}}, \quad \phi' = \phi\tfrac{\phi}{C\sqrt{gC}}, \quad p' = \tfrac{p}{\rho g C}, \quad \rho' = 1 \tag{72}$$

where Fr denotes the Froude number. Based on the problem parameters, Fr =

0.567. Two foil submergences were tested using this value, one non-breaking with $d = 0.261$ m ($d' = 1.2857$) and one breaking with $d = 0.159$ m ($d' = 0.7832$).

Computations are performed in a coordinate system moving with the foil speed $\mathbf{U}(t) = V_B(t)\,\mathbf{i}$ (see Eqs. 79 and 80), which is ramped up from 0 to V_{Bm} over 2 s, using a tanh function. In relative axes, the computational domain length and NWT width can be significantly reduced as compared to that of the physical tank; as these are quasi-2D simulations. Thus,the NWT dimensions were $15C \times C \times h$ in length, width and height, respectively, with the foil submergence d' varying for the two different test cases (Fig. 21). The coordinate system is positioned on the free surface, on the NWT axis above the foil center of mass; based on this, the NWT extends from $x' = [-3, 12]$, $y' \in [-0.5, 0.5]$ and $z' \in [0, -h']$ and the foil center is positioned at $(0, -d', 0)$.

A $L'_{AB} = 3.5$ long AB is specified for $x' \in [8.5, 13]$ onward (see Eqs. 61 and 65, with h'_0 set to 1). A sponge layer was also specified upstream in the domain for $x' \in [-3, 1.2]$ with a tanh like shape function, to absorb small instabilities associated with the semi-Lagrangian time updating. In the local breaker model, waves are assumed to break when their maximum front slope on the free surface $\beta > \beta_b = 14$ deg or $\kappa_x a > 0.35$, with κ_x the axial curvature.

The boundary discretization has $6,092$ nodes uniformly distributed on the boundary, with a free surface spacing such that there are at least 20 points per wavelength in the generated wave train, to accurately simulate properties of the downstream wake (Fig. 21). The time step is initially set to $\Delta t' = 0.05$ and, as simulations proceeded, based on 0.45 Courant number, Δt gradually reduces to an average $\Delta t' = 0.039$ value. Quasi-steady state is reached in simulations after about 800 time steps. Fig. 21 shows, for the breaking wave case ($d = 0.159$), that a well developed decaying oscillatory wave train has been generated downstream
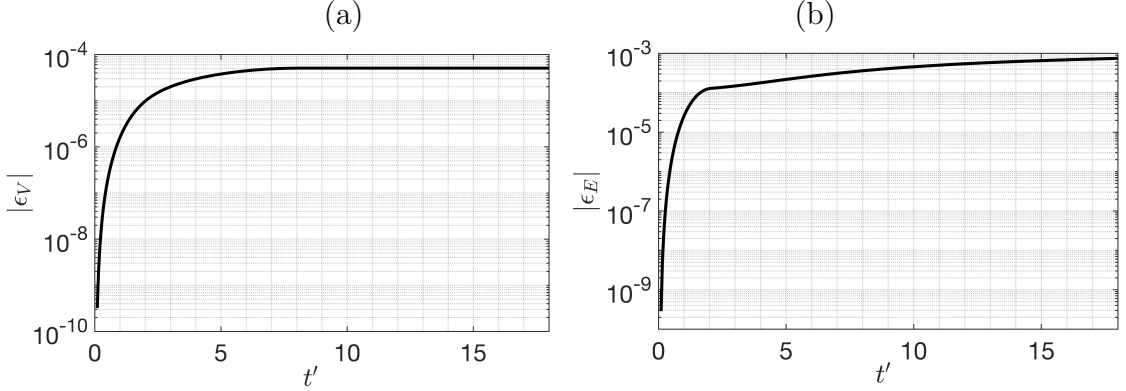
Figure 22: Relative errors in volume with respect to the foil volume (a) and total energy with respect to the maximum kinetic energy of the foil (b), in the 3D-NWT simulation of Duncan's towed hydrofoil experiment (Fig. 21) for the non-breaking test case ($d = 0.261$). The volume error stabilizes after 250 time steps. The energy error reaches 8×10^{-4} after 800 time steps.

of the foil, with the expected alternating outwards and inwards normal velocity (Fig. 21a). Fig. 21b also shows the damping pressure distribution around the first "breaking" wave, based on using a maximum front slope criterion with critical angle $\beta_b = 14$ deg, slightly below that measured in experiments (14.7 deg).

With these grid parameters, Fig. 22a shows, in the non-breaking case ($d = 0.261$), the relative error on 3D-NWT volume with respect to the volume of the foil $|\epsilon_V|$ stabilizes to 4×10^{-5} after 250 time steps, which is quite small considering the fairly coarse discretization of the foil (Fig. 21). As is typical in such simulations [11], Fig. 22b shows that the relative error on total energy $|\epsilon_E|$, scaled by the maximum kinetic energy of the foil , is about 10-20 times larger than $|\epsilon_V|$ and never quite stabilizes, reaching 8×10^{-4} after 800 time steps. Both of these maximum errors are small enough to allow for a comparison with experiments.

Figure 23 shows the quasi-steady free surface elevations simulated in the 3D-NWT (Fig. 21) for the non-breaking ($d = 0.261$ m) and breaking ($d = 0.159$ m) cases, as compared to results of Duncan's towed hydrofoil experiments. In the non-breaking case, Fig. 23a shows that numerical results agree well with experiments in
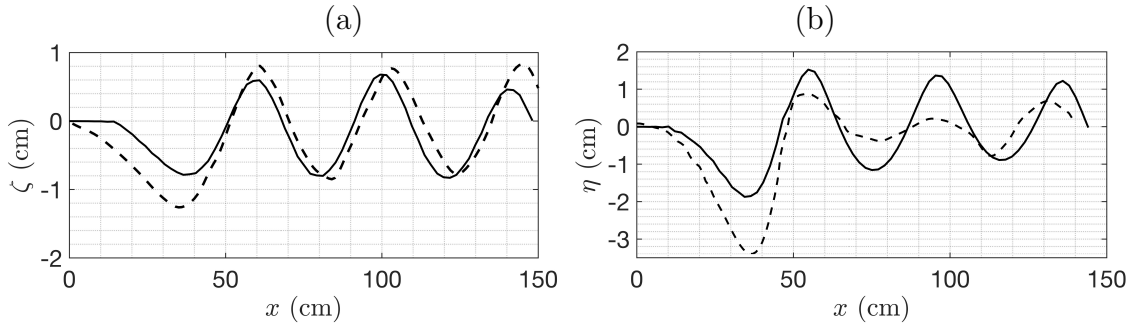
Figure 23: Quasi-steady free surface elevations simulated in the 3D-NWT (solid lines; Fig. 21) for the non-breaking (a) ($d = 0.261$ m) and breaking (b) ($d = 0.159$ m) cases in Duncan's towed hydrofoil experiments (dashed line).

the central part of the measurement area, from $x = 40 - 140$ cm downstream of the foil; the agreement is less good upstream and downstream of this area. In Duncan's experiments [1, 2], however, the free surface elevation was measured by a camera with a 10 mm lens centered on the first wave (at about $x = 70$ cm), located 0.15 m above still water level and 1.1 m out to the tank side, moving at the same speed as the foil and looking slightly downward through the transparent side of the tank. With this set-up, it is expected that the measured surface elevations would be increasingly distorted as one looks away from the camera axis on either side of the camera. Note, in their recent 2D-FNPF-BEM simulations of Duncan's experiments for non-breaking waves, Hu et al. [50] also observed a similarly reduced agreement of measured and simulated surface elevations upstream and downstream of the camera axis.

In the breaking case, Fig. 23b shows that the simulation does not quite match the experiments although the predicted wavelengths, the locations of troughs and crests, and the first wave height are in fairly good agreement. Again considering Duncan's experimental results, one sees that the breaking wave case is a very turbulent undular bore, with many irregularities, foam, and bubbles on and near the free surface, whose precise elevation should be even harder to estimate with this
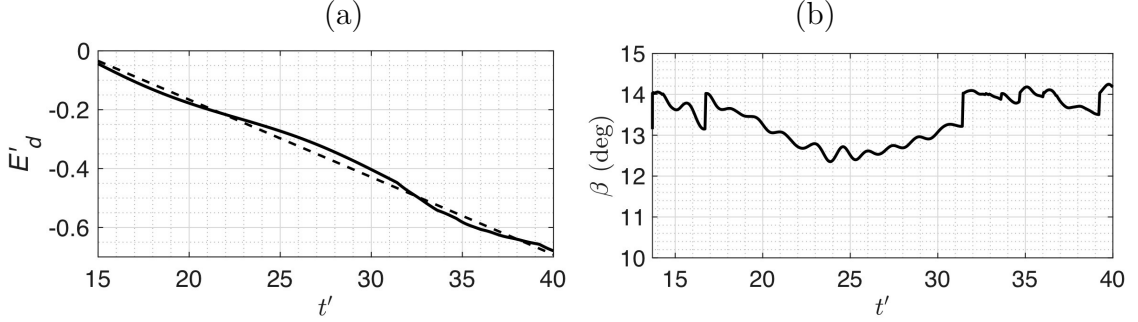
Figure 24: Simulation in the 3D-NWT of Duncan's breaking case ($d = 0.159$ m): (a) time evolution of cumulative energy dissipated during wave breaking suppression (solid line; integral of $E_d = P_d \Delta t$ from Eq. 64), compared to Duncan's parameterization (dashed line) (integral of $\epsilon_b \Delta t$, with $b = 0.0372$, for $\beta_b = 14$ deg, used in Eq. 65), both in non-dimensional form; (b) time evolution of breaking wave front slope angle β after the breaking criterion is first met.

experimental set-up than in the non-breaking case. Additionally, the first "breaking" wave in simulations appears to be higher on the surface than in experiments, which could result from the lack of circulation on the foil and, hence, incorrect lift. With circulation, the increased negative pressure on the upper part of the foil would force the free surface downward. This is confirmed in Hu et al.'s [50] work; as they were performing 2D-FNPF simulations, they could introduce a circulation around the foil that yielded results in better agreement for the first wave mean vertical location (i.e., the wave was pulled downward), for a barely breaking case with $d = 0.193$; Hu et al. however, did not use a breaker model but simply applied smoothing and regridding to eliminate numerical instabilities. Note that circulation is a 2D concept and could not be introduced in the 3D-FNPF model.

In simulations of the breaking case, the slope breaking criterion was set slightly smaller at $\beta_b = 14$ deg, than the experimental value of the steady breaker front face of 14.7 deg. Using this value, the dissipation constant was computed at $b = 0.0372$, and used to compute the damping pressure calibration constant with Eq. 65. In this equation, the characteristic velocity c_b was chosen to be that of the location where the breaking criterion $\beta > \beta_b$ was met. With these parameters,

91

Fig. 24a shows that the time history of the cumulative energy dissipated by the pressure patch matches Duncan's experimental value well. When the damping pressure patch has absorbed enough energy in the breaking wave, the front slope angle decreases to below β_b and the pressure is gradually reduced, down to zero, using a temporal decrease similar to the tanh ramp-up. This on-off process causes small fluctuations in both the breaking wave and its front slope angle around the threshold $\beta_b = 14$ deg, which can be seen in Fig. 24b.

3.4.2   3D breaking in the wake of advancing twin pressure patches

The same approach as applied above to the quasi-2D breaking case of Duncan's experiments is now used to suppress breaking waves in the complex 3D wake generated by advancing twin pressure patches accelerated from a state of rest to a constant velocity U_0 (Fig. 20). As before, the problem is solved with the semi-Lagrangian updating formalism, in a system of axis moving with the advancing pressure patches velocity $U(t)$. Non-breaking wakes generated by a single advancing pressure patch had been modeled by Sung and Grilli [39, 40, 14]. As in the latter study, the pressure distribution in each patch has an approximate footprint a by b, in the x and y directions, respectively, and a smooth Gaussian-like shape given by [51],

$$
\begin{aligned}
p_a(x, y) \;=\; & M(t)\frac{p_0}{4}\{\tanh \alpha(x - x_i + a) - \tanh \alpha(x - x_i - a)\} \\
& \{\tanh \gamma(y - y_i + b) - \tanh \gamma(y - y_i - b)\} \qquad (73)
\end{aligned}
$$

in witch (x_i, y_i) is the central position of the pressure patch and $M(t)$ is a tanh time ramping up function, to avoid triggering instabilities in the NWT. Here, non-dimensional variables are scaled using the reference length $C = 2a$ in Eqs. 72.

Here, For validating the proposed BEM-FMM model, the corresponding wave resistance of non breaking nonlinear wave, caused by a pressure patch of Eq. 73

(a)   (b)
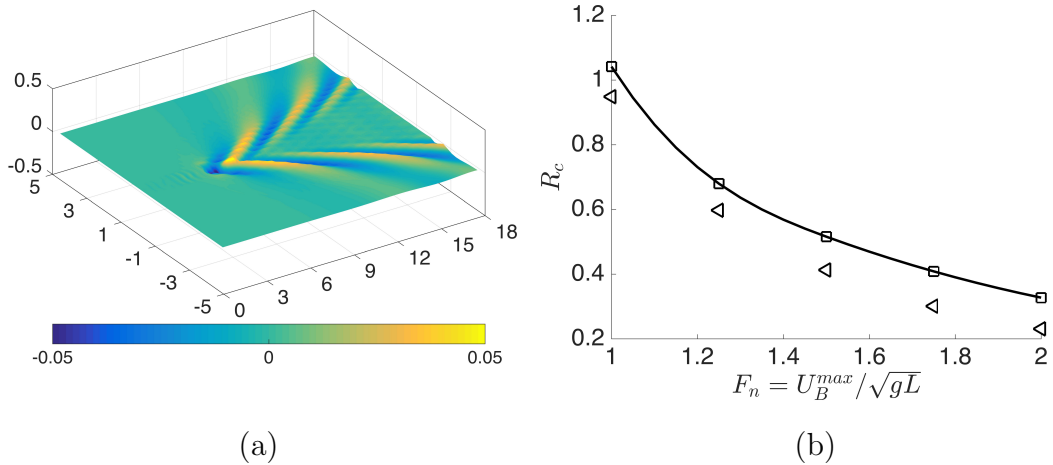
Figure 25: The wave making Resistance of the single surface air cushion in compare to linear theory. a) the wake of the SAC with $p'_o = 0.025, a = b = 0.5$ and $Fr = U_B^{max}/\sqrt{2ga} = 1$;b) the linear theory by Doctor and Sharma[51]($\square$) and current result($\triangleleft$). the new model slightly under predict the values of wave making resistant.

specified on the free surface and accelerating from a state of rest to a steady state has been studied. Wave resistance due to the motion of the disturbance is obtained as the pressure force on the disturbed free surface within the cushion,

$$R_w = - \int_{S_{AC}} p n_x ds \qquad (74)$$

where S_{AC} denotes the air-cushion surface area. This physical quantity is made dimensionless as $Rc = (R_w/W)(\rho ga/p_o)$ where $W = 4\rho gap$ is the weight supported by the pressure patch. For correct comparison to [51] the parameters of Eq. 73, $b/a = 0.5, \alpha a = \beta a = 5$. The computational domain is 18 dimensionless units long and 10 wide, and there are 81 and 15 node points in the x and y directions, respectively, yielding an initial grid size of about 0.22 unit in each direction. The water depth is d = 1. Throughout the simulations, the time step keep constant $\delta t = 0.05$ The non-dimensional wave making force R_c in different Froud numbers has been shown in Figure 25 in compare to the analytic result of
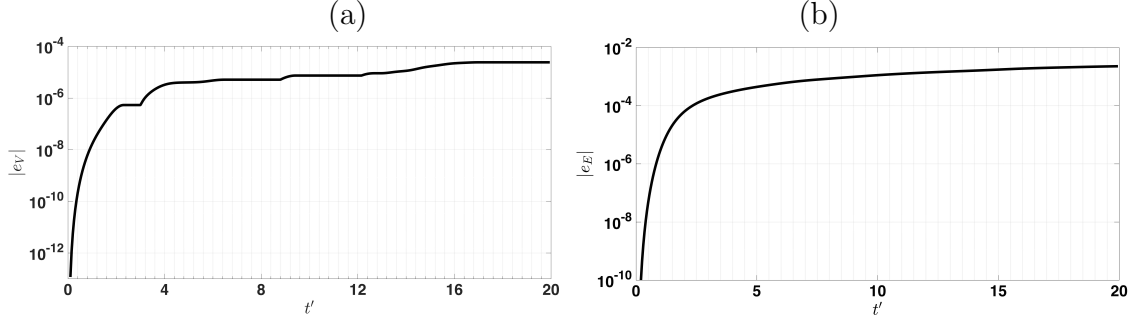
Figure 26: Relative errors in volume with respect to the displacement volume of the twin pressure patch (a) and total energy with respect to the maximum kinetic energy of moving pressure patch (b), in the 3D-NWT simulation of breaking suppression in the wake of twin surface pressure patch. The energy error reaches 2.2×10^{-3} after 400 time steps.

Doctors and Sharma [51].The Values of the wave making resistance are slightly under-predicted due to limitation of vertical updating scheme of free surface which cause oscillations in the values of the measured wave making force. This also has been observed in other literature (see [39]).

For the Twin pressure patch simulations, the computational domain spans $x' \in [0, 20]$, $y' \in [-5, 5]$ and $z' \in [0, -2]$ in each direction, respectively. With an initial grid size of 0.2 units in each direction, the time step is kept constant at $\Delta t' = 0.05$, since with vertical updating nodes, the size of boundary elements stays nearly constant. No flow boundary condition conditions are applied on the downstream, upstream and sidewall boundaries, which are all moving with the same velocity as the pressure patch. On the upstream part of the free surface, as before, an artificial absorbing patch is specified with a tanh shape to absorb unwanted sawtooth oscillations due to the semi-Lagrangian time updating. The twin pressure patches are positioned at $(x_1, y_1) = (4.5, -2)$ and $(x_2, y_2) = (4.5, 2)$, and for both $a = 0.5$, $b = 0.5$, $\alpha a = \gamma b = 5$, and $Fr = 1.0$. After 320 time steps, the numerical error on the computation domain volume is $\epsilon_V = 6.36 \times 10^{-5}$, showing that the solution is accurately computed.

94

The algorithm described above is applied to dynamically identify the crests and troughs, and compute the wave phase velocity over the free surface rest points (Fig. 20). By tuning the combination of strength and velocity of the pressure patch to $p'_0 = 0.075$ for $Fr = 1.0$, as steady state is reached, a single breaking wave forms along the middle axis of the two interacting single patch wakes. The breaking criterion ($\beta_b > 37^o$, $\kappa_b a > 0.35$) is met approximately at $(x_b, y_b) = (9.5, 0)$, which allows defining the area of the absorbing pressure patches and absorb energy in the breaking wave to suppress breaking and stabilize it. When the breaking detected, an algorithm based on divide and conqueror strategy will search the closest neighboring crest and troughs of the breaking point in two ortogonal direction (e.g. x and y) for defining the damping region between to consecutive crest surrounding the breaking point $\mathbf{x}_b$. For defining the damping pressure of Eq.61. The final damping region would be defined based on multiplying the two 1D Gaussian like function similar to Eq. 62.

$$S_b(x, y) = S_b(x)S_b(y) \tag{75}$$

which in this form and based on type of breaker the shape function can be modified accordingly.

3.5   Discussion and conclusions

Results reported in this paper on the detection and suppression of wave breaking in a 3D-FNPF-NWT, indicate that the spilling breaker model implemented by way of a distribution of absorbing pressure, calibrated based on a physical criterion, is an effective method for allowing to pursue long-term simulations of nonlinear wave-structure interactions, in ocean or naval engineering. Although the two applications presented above were for steady breakers in the permanent surface wake of advancing disturbances, the method could be extended to suppressing unsteady
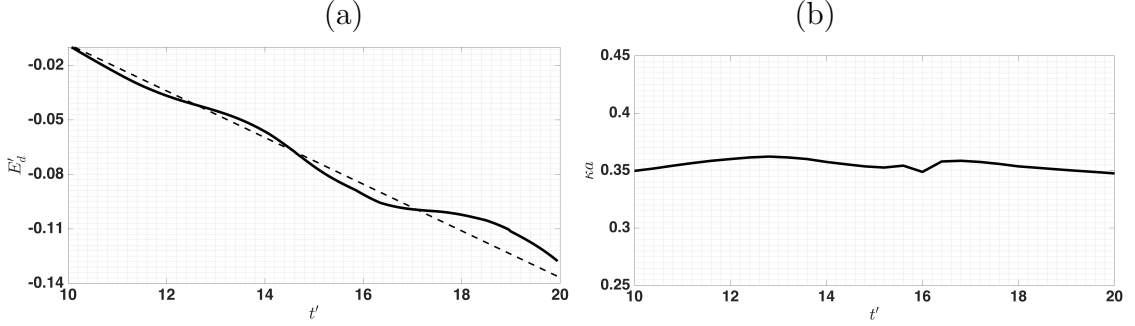
Figure 27: Simulation in the 3D-NWT of twin pressure patch breaking case: (a) time evolution of cumulative energy dissipated during wave breaking suppression (solid line; integral of $E_d = P_d \Delta t$ from Eq. 64), compared to Duncan's parameterization (dashed line) (integral of $\epsilon_b \Delta t$, with $b = 0.0149$, for $\beta_b = 37$ deg, used in Eq. 65), both in non-dimensional form; (b) time evolution of breaking wave maximum curvature κa after the breaking criterion is first met.

breakers [52, 36] provided a relevant energy dissipation value is used. Some recent numerical work could be used to this effect, that parameterizes the amount of energy dissipated in individual breakers [37, 38, 18]. Alternately, in the context of the hybrid model that motivated this work, the energy dissipation could be provided from the viscous part o the solution [47, 53].

An efficient wave tracking algorithm based on a Hilbert transform was developed to identify the locations of wave crests and troughs in simulation results, to verify the breaking criterion and specify both the area and strength of the damping (absorbing) pressure p_d. This algorithm also allowed calculating the characteristic breaking velocity c_b, the breaking crest phase speed, which is needed to compute the energy dissipation rate ϵ_b. As this required storing some of the history of the breaking wave crest location, instead, c_b was set equal to the particle velocity at the crest, assuming both are equal at breaking.

With this spilling breaker model, simulation results were found in good agreement with Duncan's experimental results for a submerged towed hydrofoil [1, 2]. As a semi-Lagrangian time updating is used in the NWT, wave overturning is not observed, but in any case this would be too late to allow for the wave dissipation

by the absorbing pressure. Hence, instead, a conservative breaking criterion based on a maximum wave front face angle β_b was used as a breaking criteria to simulate Duncan's experiments, based on the observed experimental value (about 14 deg). Nevertheless, for the reported case, breaking may still occur too soon and it may be of interest to try and increase β_b further. A limitation however is that, with too large a β_b value, it may not be possible to absorb the wave energy and suppress the occurrence of breaking fast enough. Clearly more work needs to be done on the sensitivity of results to this important parameter. Likewise, for the twin cushion wake, an additional criterion based on surface curvature was successfully used, which also would require some additional calibration and verification.

Additional future work will concentrate on setting the correct b value for the energy dissipation rate. Numerical simulation showed that the values defined by Duncan slightly underpredict the amount of dissipation. Perhaps the new parameterization proposed in recent work could be adopted [37, 38, 18].

In conclusion, the 3D-FNPF-NWT, with the addition of a simple breaker model, can be used as an efficient and accurate tool to perform realistic simulations of strongly nonlinear wave generation by an advancing surface disturbance, such as a submerged or emerged structure (or ship), or a surface pressure patch (cushion or SES vehicle). One should, however, keep in mind the limitations of this *ad hoc* method of breaking wave detection and suppression, for modeling details of the flow in breaking waves.

3.6   acknowledgements

List of References

[1] J. H. Duncan, "An experimental investigation of breaking waves produced by a towed hydrofoil," *Proc. R. Soc. Lond. A*, vol. 377, no. 1770, pp. 331–348, 1981.

[2] J. H. Duncan, "The breaking and non-breaking wave resistance of a two-dimensional hydrofoil," *J. Fluid Mech.*, vol. 126, pp. 507–520, 1983.

[3] M. S. Longuet-Higgins and E. D. Cokelet, "The deformation of steep surface waves on water-i. a numerical method of computation," *Proc. R. Soc. Lond. A*, vol. 350, no. 1660, pp. 1–26, 1976.

[4] J. W. Dold and D. H. Peregrine, "An efficient boundary-integral method for steep unsteady water waves," *Numerical methods for fluid dynamics II*, vol. 671, p. 679, 1986.

[5] D. G. Dommermuth, D. K. P. Yue, W. M. Lin, R. J. Rapp, E. S. Chan, and W. K. Melville, "Deep-water plunging breakers: a comparison between potential theory and experiments," *J. of Fluid Mech.*, vol. 189, pp. 423–442, 1988.

[6] S. T. Grilli, J. Skourup, and I. A. Svendsen, "An efficient boundary element method for nonlinear water waves," *Engineering Analysis with Boundary Elements*, vol. 6, no. 2, pp. 97–107, 1989.

[7] S. T. Grilli, R. Subramanya, I. A. Svendsen, and J. Veeramony, "Shoaling of solitary waves on plane beaches," *J. Waterway, Port, Coastal, and Ocean Engng.*, vol. 120, no. 6, pp. 609–628, 1994.

[8] S. T. Grilli and R. Subramanya, "Numerical modeling of wave breaking induced by fixed or moving boundaries," *Computational Mechanics*, vol. 17, no. 6, pp. 374–391, 1996.

[9] S. T. Grilli, I. A. Svendsen, and R. Subramanya, "Breaking criterion and characteristics for solitary waves on slopes," *J. Waterway, port, Coastal, and Ocean Engng.*, vol. 123, no. 3, pp. 102–112, 1997.

[10] F. E. Camfield, Y. Li, F. Raichlen, S. T. Grilli, I. A. Svendsen, and R. Subramanya, "Discussions and closure: Breaking criterion and characteristics for solitary waves on slopes," *J. Waterway, Port, Coastal, and Ocean Engng.*, vol. 124, no. 6, pp. 329–335, 1998.

[11] S. T. Grilli, P. Guyenne, and F. Dias, "A fully non-linear model for three-dimensional overturning waves over an arbitrary bottom," *International Journal for Numerical Methods in Fluids*, vol. 35, no. 7, pp. 829–867, 2001.

[12] P. Guyenne and S. Grilli, "Numerical study of three-dimensional overturning waves in shallow water," *Journal of Fluid Mechanics*, vol. 547, pp. 361–388, 2006.

[13] C. Fochesato, S. Grilli, and F. Dias, "Numerical modeling of extreme rogue waves generated by directional energy focusing," *Wave Motion*, vol. 44, no. 5, pp. 395–416, 2007.

[14] H. G. Sung and S. T. Grilli, "BEM computations of 3D fully nonlinear free-surface flows caused by advancing surface disturbances," *Intl. J. Offshore and Polar Engng.*, vol. 18, no. 04, pp. 292–301, 2008.

[15] S. T. Grilli, F. Dias, P. Guyenne, C. Fochesato, and F. Enet, "Progress in fully nonlinear potential flow modeling of 3d extreme ocean waves," in *Advances in numerical simulation of nonlinear water waves.* World Scientific, 2010, pp. 75–128.

[16] E. Guerber, M. Benoit, S. T. Grilli, and C. Buvat, "A fully nonlinear implicit model for wave interactions with submerged structures in forced or free motion," *Engineering Analysis with Boundary Elements*, vol. 36, no. 7, pp. 1151–1163, 2012.

[17] J. C. Harris, K. Kuznetsov, C. Peyrard, S. Saviot, A. Mivehchi, S. T. Grilli, M. Benoit, *et al.*, "Simulation of wave forces on a gravity based foundation by a bem based on fully nonlinear potential flow," in *The 27th International Ocean and Polar Engineering Conference.* International Society of Offshore and Polar Engineers, 2017.

[18] X. Barthelemy, M. L. Banner, W. L. Peirson, F. Fedele, M. Allis, and F. Dias, "On a unified breaking onset threshold for gravity waves in deep and intermediate depth water," *J. Fluid Mech.*, vol. 841, pp. 463–488, 2018.

[19] L. Greengard and V. Rokhlin, "A fast algorithm for particle simulations," *J. Comput. Phys.*, vol. 73, pp. 325–348, 1987.

[20] C. Fochesato and F. Dias, "A fast method for nonlinear three-dimensional free-surface waves," in *Proc. Royal Soc. London A*, vol. 462, no. 2073. The Royal Society, 2006, pp. 2715–2735.

[21] S. B. Nimmala, S. C. Yim, and S. T. Grilli, "An efficient three-dimensional FNPF numerical wave tank for large-scale wave basin experiment simulation," *J. Offshore Mech. and Arctic Engng.*, vol. 135, no. 2, p. 021104, 2013.

[22] J. C. Harris, E. Dombre, M. Benoit, and S. T. Grilli, "Fast integral equation methods for fully nonlinear water wave modeling," in *Proc. 24th Intl. Ocean and Polar Engng. Conf.* International Society of Offshore and Polar Engineers, 2014, pp. 583–590.

[23] J. Harris, E. Dombre, A. Mivehchi, M. Benoit, S. Grilli, and C. Peyrard, "Progress in fully nonlinear wave modeling for wave-structure interaction," *Proceedings of the 15th Journée de lHydrodynamique*, p. 12, 2016.

[24] M. S. Longuet-Higgins, "Parametric solutions for breaking waves," *J. Fluid Mech.*, vol. 121, pp. 403–424, 1982.

[25] R. Cointe, "Numerical simulation of a wave channel," *Engineering Analysis with Boundary Elements*, vol. 7, no. 4, pp. 167–177, 1990.

[26] S. T. Grilli and J. Horrillo, "Numerical generation and absorption of fully nonlinear periodic waves," *Journal of Engineering Mechanics*, vol. 123, no. 10, pp. 1060–1069, 1997.

[27] S. T. Grilli and J. Horrillo, "Shoaling of periodic waves over barred-beaches in a fully nonlinear numerical wave tank," *Intl. J. Offshore and Polar Engng.*, vol. 9, no. 4, pp. 257–263, 1999.

[28] A. Clément, "Coupling of two absorbing boundary conditions for 2D time-domain simulations of free surface gravity waves," *J. Comput. Phys.*, vol. 126, no. 1, pp. 139–151, 1996.

[29] S. Guignard, S. T. Grilli, *et al.*, "Modeling of wave shoaling in a 2D-NWT using a spilling breaker model," in *Proc. 11th Intl. Offshore and Polar Engng. Conf.*, vol. 3. International Society of Offshore and Polar Engineers, 2001, pp. 116–123.

[30] I. A. Svendsen, P. Madsen, and J. B. Hansen, "Wave characteristics in the surf zone," in *Proc. Intl. Coastal Engineering Conf.*, 1978, pp. 520–539.

[31] I. A. Svendsen and P. A. Madsen, "A turbulent bore on a beach," *J. Fluid Mech.*, vol. 148, pp. 73–96, 1984.

[32] R. Cointe and M. P. Tulin, "A theory of steady breakers," *J. Fluid Mech.*, vol. 276, pp. 1–20, 1994.

[33] C. Fochesato, S. Grilli, and P. Guyenne, "Note on non-orthogonality of local curvilinear co-ordinates in a three-dimensional boundary element method," *International journal for numerical methods in fluids*, vol. 48, no. 3, pp. 305–324, 2005.

[34] P. Stansell and C. MacFarlane, "Experimental investigation of wave breaking criteria based on wave phase speeds," *J. Phys. Oceanography*, vol. 32, no. 5, pp. 1269–1283, 2002.

[35] A. K. Subramani, R. F. Beck, and W. W. Schultz, "Suppression of wave-breaking in nonlinear water wave computations," in *Proc. 13th Intl. Workshop Water Waves and Floating Bodies*, 1998, pp. 139–142.

[36] M. Perlin, W. Choi, and Z. Tian, "Breaking waves in deep and intermediate waters," *Annual Review Fluid Mech.*, vol. 45, pp. 115–145, 2013.

[37] M. Derakhti and J. T. Kirby, "Breaking-onset, energy and momentum flux in unsteady focused wave packets," *J. Fluid Mech.*, vol. 790, pp. 553–581, 2016.

[38] M. Derakhti, M. L. Banner, and J. T. Kirby, "Predicting the breaking strength of gravity water waves in deep and intermediate depth," *J. Fluid Mech.*, vol. 848, 2018.

[39] H. G. Sung and S. T. Grilli, "Numerical modeling of nonlinear surfacewaves caused by surface effect ships dynamics and kinematics," in *Proc. 15th Intl. Offshore and Polar Engng. Conf.* International Society of Offshore and Polar Engineers, 2005, pp. 124–131.

[40] H. G. Sung and S. T. Grilli, "Combined eulerian-lagrangian or pseudo-lagrangian descriptions of waves caused by an advancing free surface disturbance," in *Proc. 16th Intl. Offshore and Polar Engng. Conf.*, vol. 3. International Society of Offshore and Polar Engineers, 2006, pp. 487–494.

[41] J. Cabral, L. Wrobel, and C. Brebbia, "A BEM formulation using B-splines: I-uniform blending functions," *Engineering analysis with boundary elements*, vol. 7, no. 3, pp. 136–144, 1990.

[42] J. Cabral, L. Wrobel, and C. Brebbia, "A BEM formulation using B-splines: II-multiple knots and non-uniform blending functions," *Engineering Analysis with Boundary Elements*, vol. 8, no. 1, pp. 51–55, 1991.

[43] R. Ushatov, H. Power, and J. R. Silva, "Uniform bicubic b-splines applied to boundary element formulation for 3-d scalar problems," *Engineering analysis with boundary elements*, vol. 13, no. 4, pp. 371–381, 1994.

[44] E. V. Shikin and A. I. Plis, *Handbook on Splines for the User.* CRC Press, 1995.

[45] B. Büchmann, "Accuracy and stability of a set of free-surface time-domain boundary element models based on B-splines," *Intl. J. Numerical Methods in Fluids*, vol. 33, pp. 125–155, 2000.

[46] S. Grilli and I. Svendsen, "Corner problems and global accuracy in the boundary element solution of nonlinear wave flows," *Engineering Analysis with Boundary Elements*, vol. 7, no. 4, pp. 178–195, 1990.

[47] A. Mivehchi, J. C. Harris, S. T. Grilli, J. M. Dahl, C. M. O'Reilly, K. Kuznetsov, and C. F. Janssen, "A hybrid solver based on efficient BEM-potential and LBM-NS models: recent BEM developments and applications to naval hydrodynamics," in *Proc. 27th Intl. Ocean and Polar Engng. Conf.* International Society of Offshore and Polar Engineers, 2017, pp. 721–728.

[48] R. Yokota, J. P. Bardhan, M. G. Knepley, L. A. Barba, and T. Hamada, "Biomolecular electrostatics using a fast multipole BEM on up to 512 GPUs and a billion unknowns," *Computer Physics Communications*, vol. 182, pp. 1272–1283, 2011.

[49] R. Yokota, "An FMM based on dual tree traversal for many-core architectures," *J. Algorithms and Computational Tech.*, vol. 7, pp. 301–324, 2013.

[50] J. Hu, L. Guo, and S. Sun, "Numerical simulation of the potential flow around a submerged hydrofoil with fully nonlinear free-surface conditions," *J. Coastal Res.*, vol. 34, no. 1, pp. 238–252, 2017.

[51] L. J. Doctors and S. D. Sharma, "The wave resistance of an air-cushion vehicle in steady and accelerated motion," *J Ship Res.*, vol. 16, pp. 248–260, 1972.

[52] R. Muscari and A. Di Mascio, "Numerical modeling of breaking waves generated by a ship hull," *J. Marine Science and Technology*, vol. 9, no. 4, pp. 158–170, 2004.

[53] C. M. O'Reilly, S. T. Grilli, J. C. Harris, A. Mivehchi, C. F. Janssen, and J. M. Dahl, "A Hybrid Solver Based on Efficient BEM-potential and LBM-NS Models: Recent LBM Developments and Applications to Naval Hydrodynamics," in *Proc. 27th Intl. Ocean and Polar Engng. Conf.* International Society of Offshore and Polar Engineers, 2017, p. 713 720.

MANUSCRIPT 4

Three Dimensional Boundary Element Solution of Nonlinear Wave Flow with Uniform Cubic B-Spline Elements and Corner Treatments.

by
A.Mivehchi[1],S.T. Grilli[1],J.M. Dahl[1],
J. C. Harris[2], K. Kuznetsov[2]

(1) Dept. of Ocean Engineering, University of Rhode Island, Narragansett, RI 02882,

USA

(2) LHSV, Ecole des Ponts, CEREMA, EDF R&D, Université Paris-Est, Chatou, France

Abstract

A 3D fully nonlinear Numerical Wave Tank (NWT) accelerated with the Fast Multipole Method (FMM) with Semi-Lagrangian (SL) free surface updating is extended to include compatibility conditions at corners, to improve the numerical accuracy and avoid numerical instabilities that can propagate due to the nonlinear free surface boundary condition. The corners and edges of the fluid domain are modeled with a double node representation [1] and an additional constraint including a velocity compatibility condition is defined at these double nodes [2] at each time step. Nonlinear wave generation, propagation, reflection and absorption is demonstrated with this model, showing a stable solution with these corner treatments and non-physical instabilities at the free surface without the corner treatments. Additionally, the global accuracy of the NWT is improved by the addition of a stable geometry representation at the free surface using cubic B-splines and integrating the velocity compatibility condition to provide auxiliary equations required to update the surface geometries . The treatment of the intersection of an arbitrary three dimensional surface piercing object is discussed in the context of semi-Lagrangian time updating. Global accuracy of computations with the new corner treatment is evaluated by modeling a non-linear propagating wave in a 3-D domain. Applications with known exact numerical shapes (solitary and stream function waves) are shown, demonstrating good agreement with the theoretical values and literature.

4.1   Introduction

In the past few decades, numerical models based on irrotational (and thus kinematically inviscid) potential flow theory, with fully nonlinear free surface boundary conditions, have proven to be very accurate (as compared to experiments) for simulating steep waves in two- or three-dimensions (2D/3D) in deep,

inter- mediate or shallow water, up to the point of breaking, without or in the presence of fixed or moving surface-piercing structures. When using an Eulerian-Lagrangian (EL) free surface time updating, these models can also accurately simulate wave overturning up to the time a breaker jet impacts the free surface [3, 4, 5, 6, 7, 2, 8, 9, 10, 11, 12, 13, 14, 15, 16, 17]. In most of these studies, the so-called Fully Nonlinear Potential Flow (FNPF) equations were solved using a higher-order Boundary Element Method (BEM), combined with a high-order EL time updating algorithm. In 3D problems, the BEM method suffers from numerical complexity with order N^2 computational time due to the construct of the method. The Fast multipole Method (FMM) has been developed to alleviate this problem to help speed up computations, yielding a nearly order N solution [18, 19, 12, 13, 14, 20, 21, 22].

A well known and common problem in solution to the boundary element method is the loss of accuracy at the corners (in 2D) and edges (in 3D). Due to the intersection of nodes or surfaces at these locations, special treatment is required. A corner or edge is defined where the tangent to the boundary has a sharp discontinuity (e.g. intersecting walls of a numerical wave tank). This loss of accuracy is due to the existence of two or more normal potential derivatives over the corners edges which result in an under-constrained system . Special treatment is required to achieve a stable numerical result. Without proper treatment of corners and edges, the BEM solution can exhibit large errors that propagate through the solution domain from the problematic corners and edges. In the context of waves generated by a wavemaker or rapidly moving body, a poor numerical solution at the corner will have the appearance of a singularity, and over time, it will lead to instability of the numerical solution [2]. This is critically important in the solution of non-linear phenomena, such a solving the fully non-linear potential flow (FNPF)

105

dynamic free surface conditions, where even small errors in the solution at these corners can propagate and magnify throughout the domain.

There have been many solutions to this mathematical problem for 2D-BEM in solid mechanics, electrostatics and acoustics involving physics that often don't involve large movement at corners[23, 24, 25, 26, 27, 28, 29]. In wave mechanics applications, Grilli et al.[1] proposed specific numerical treatments to eliminate numerical errors using double-nodes at corners and defining continuity conditions for the potential. They specified the uniqueness of the fluid velocity at corners using compatibility conditions between the normal and tangential derivatives of the potential. They also improved accuracy of (non-singular but potentially quasi-singular) numerical integration at corners, using adaptive numerical integration techniques. Using such treatments, they calculated the solution of various mixed boundary value problems, in computational domains with sharp corners, with extremely small errors [30, 31, 7, 8, 32]. Based on the same methods, Grilli and Subramanya [2] developed extended corner compatibility conditions which provided further improvements of the corner solution in the case of rapidly moving boundaries (e.g. a wave making paddle, heaving or pitching floating body, etc.).

In the following, we briefly describe the FNPF model governing equations and boundary conditions, and the mathematical formulations associated with discritization of the boundary using a cubic uniform B-Spline, auxiliary equations as end conditions for such B-splines, and corner treatment and briefly summarize the numerical model implementation and methods, which have all been detailed elsewhere[1, 14, 22, 16]. Finally, we present results of numerical simulations and their validation with earlier works on solitary wave propagation, reflection, wave generation and wave absorption in a numerical wave tank.

4.2 Model equations
4.2.1 Governing Equation and Boundary Conditions

We model irrotational flows of an incompressible and inviscid fluid, for which the flow velocity is given by $\mathbf{u} = \boldsymbol{\nabla}\phi$, with $\phi(\mathbf{x}, t)$ the velocity potential. In Cartesian coordinates, the position vector is defined as $\mathbf{x} = (x, y, z)$, in which z is pointing vertically upwards and gravity is pointing downward, with acceleration g. Such *potential flows* are governed by mass conservation, which yields the Laplace equation for the velocity potential,

$$\nabla^2 \phi = 0 \quad \text{in} \quad \Omega(t) \tag{76}$$

over domain $\Omega(t)$ with boundary $\Gamma(t)$. In the context of the BEM, using Green's second identity, this governing equation is transformed into a Boundary Integral Equation (BIE),

$$\alpha(\mathbf{x}_l)\phi(\mathbf{x}_l) = \int_{\Gamma(\mathbf{x}(t))} \left\{ \frac{\partial \phi}{\partial n}(\mathbf{x})G(\mathbf{x}, \mathbf{x}_l) - \phi(\mathbf{x})\frac{\partial G}{\partial n}(\mathbf{x}, \mathbf{x}_l) \right\} d\Gamma(\mathbf{x}(t)) \tag{77}$$

in which $\mathbf{x}$ and $\mathbf{x}_l = (x_l, y_l, z_l)$ are points on boundary $\Gamma(t)$, $\mathbf{n} = (n_x, n_y, n_z)$ is the unit outward normal vector on the boundary, and $\alpha(\mathbf{x}_l)$ is a geometric coefficient function of the interior angle of the boundary at $\mathbf{x}_l$. The 3D free space Green's function and its normal derivative are defined in the BIE as,

$$G(\mathbf{x}, \mathbf{x}_l) = \frac{1}{4\pi r} \quad \text{and} \quad \frac{\partial G}{\partial n} = -\frac{\mathbf{r} \cdot \mathbf{n}}{4\pi r^3} \tag{78}$$

in which $\mathbf{r} = \mathbf{x} - \mathbf{x}_l$ and $r = |\mathbf{r}|$.

On the free surface $\Gamma_f(t)$, ϕ satisfies the nonlinear kinematic and dynamic boundary conditions,

$$\frac{\delta \zeta}{\delta t} = \frac{\partial \phi}{\partial z} - \boldsymbol{\nabla}_H \phi \cdot \boldsymbol{\nabla}_H \zeta - \mathbf{U}(t) \cdot \boldsymbol{\nabla}_H \zeta \qquad \qquad \text{on} \qquad \Gamma_f \tag{79}$$

$$\frac{\delta \phi}{\delta t} = -g\zeta - \frac{1}{2}\boldsymbol{\nabla}\phi \cdot \boldsymbol{\nabla}\phi - \frac{p_a}{\rho} + \frac{\partial \zeta}{\partial t}\frac{\partial \phi}{\partial z} - \mathbf{U}(t) \cdot \boldsymbol{\nabla}_H \phi \quad \text{on} \qquad \Gamma_f \tag{80}$$

respectively, with $\zeta = \mathbf{r} \cdot \mathbf{k}$ the vertical position vector of nodes on the free surface (referred to $z = 0$ and measured upward), p_a the atmospheric pressure, ρ the fluid density, $\boldsymbol{\nabla}_H = \frac{\partial}{\partial x}\mathbf{i} + \frac{\partial}{\partial y}\mathbf{j}$ the horizontal derivative ($\mathbf{i}$ and $\mathbf{j}$ are unit vector in directions x and y, respectively) and $(\partial\zeta/\partial x, \partial\zeta/\partial y)$ can be expressed as a function of the outward normal vector on the boundary, $\mathbf{n} = (n_x, n_y, n_z)$, as $(-n_x/n_z, -n_y/n_z)$.

Eqs. 79 and 80 have been expressed in a semi-Lagrangian form [33, 34, 13], assuming that the coordinate system advances at velocity $\mathbf{U}(t)$, and the semi-Lagrangian derivative is defined as,

$$\frac{\delta}{\delta t} = \frac{\partial}{\partial t} + \frac{\partial\zeta}{\partial t}\frac{\partial}{\partial z} - \mathbf{U}(t) \cdot \boldsymbol{\nabla}_H \tag{81}$$

In the NWT, waves are generated by simulating a wavemaker motion or incident wave kinematics on boundary $\Gamma_{r1}(t)$ and damped in an absorbing beach (AB) over length L_{AB}, and/or on Γ_{r2} using an absorbing piston (Fig. 28) [30]. For instance, a simple piston wavemaker motion is specified by its time dependent stroke and velocity (x_p, u_p) as,

$$\overline{x} = x_p(t); \qquad u_p(t) = -\boldsymbol{\nabla}\phi \cdot \mathbf{n} = -\frac{\overline{\partial\phi}}{\partial n} \qquad \text{on} \quad \Gamma_{r1}(t) \tag{82}$$
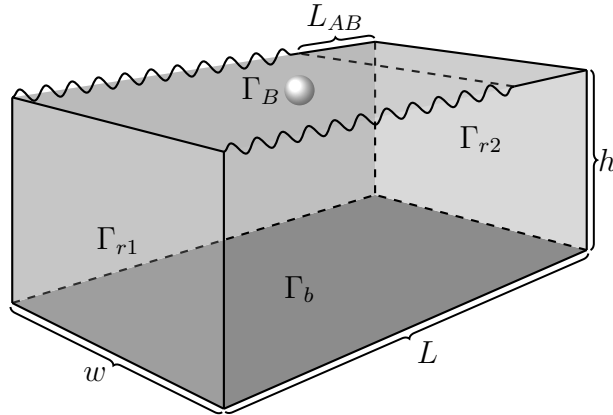
Figure 28: NWT computational domain. Waves, if any, are generated on Γ_{r1} and damped in the absorbing beach (AB) over length L_{AB}, and on Γ_{r2} using an absorbing piston.

respectively, where the overlines denote specified values. Along the stationary bottom Γ_b and on other fixed boundaries, a no-flow condition is prescribed as (Fig. 28),

$$\overline{\frac{\partial \phi}{\partial n}} = 0 \qquad \text{on} \quad \Gamma_b, \ \Gamma_{r2} \tag{83}$$

The boundary condition along a rigid submerged or surface piercing ocean/naval structure, moving with velocity $\mathbf{V}_B$, can be specified as,

$$\overline{\frac{\partial \phi}{\partial n}} = \mathbf{V}_B \cdot \mathbf{n} \qquad \text{on} \quad \Gamma_B \tag{84}$$

As indicated before, incident waves are damped at the far end of the NWT by dissipating their energy in an *absorbing beach* (AB) of length L_{AB} (Fig. 28), over which a damping pressure term p_d is added to the dynamic free surface boundary conditions; for long waves, an absorbing piston can also be specified over boundary Γ_{r2} [30, 35]. Finally, small free surface oscillations can appear upstream in simulation as a result of the semi-Lagrangian time updating. These simulations are damped in a sponge layer specified near boundary Γ_{r1}, over which $-\nu(x)\zeta$ and $-\nu(x)\phi$ terms are added to the right hand side of the kinematic and dynamic boundary conditions, respectively [36]. Within the sponge layer, the shape function $\nu(x)$ gradually increases with distance square.

4.2.2   Time integration in the NWT

At any time t, given well-posed boundary conditions, the BEM solution provides both the velocity potential and its normal derivative on the computational domain boundary, as discrete values at the N collocation points. This solution (both geometry and boundary condition) is then advanced in time on the free surface by integrating the two free surface boundary conditions, Eqs. (79) and (80). Here, a semi-Lagrangian approach is used on the free surface [33, 13], in which points are fixed in the horizontal direction and, although more complex schemes
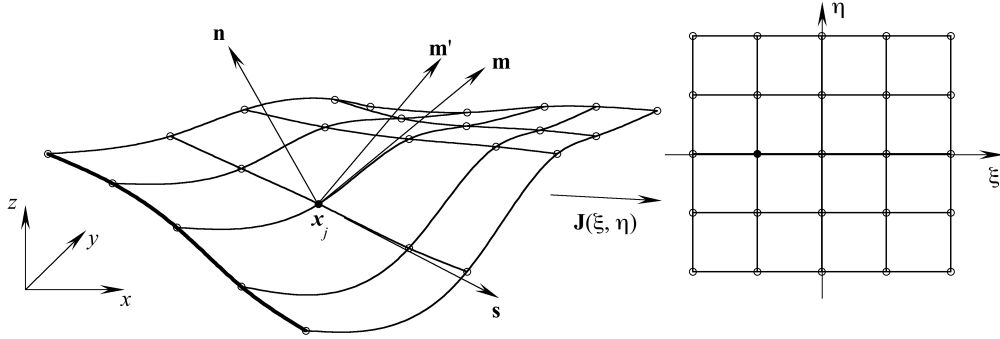
Figure 29: Definition of local non-orthogonal $(\mathbf{s}, \mathbf{m}, \mathbf{n})$ and orthogonal $(\mathbf{s}, \mathbf{m}', \mathbf{n})$ curvilinear coordinate systems used to compute tangential derivatives at collocation node $\mathbf{x}_j$ on the domain boundary; the transformation to intrinsic coordinates (ξ, η) by way of Jacobian $\mathbf{J}(\xi, \eta)$ is illustrated. The boundary is interpolated piecwise by cubic quadrilateral B-spline boundary elements. Symbols (o) mark collocation nodes and the thicker line a domain edge.

have been used in past work [10], a simple third-order Runge-Kutta scheme is used for time updating of ϕ and ζ, which can be written compactly as,

$$f^{(1)} = f^{(n)} + \Delta t(\delta_t f^{(n)})$$

$$f^{(2)} = \frac{3}{4} f^{(n)} + \frac{1}{4} \left(f^{(1)} + \Delta t(\delta_t f^{(1)}) \right)$$

$$f^{(n+1)} = \frac{1}{3} f^{(n)} + \frac{2}{3} \left(f^{(2)} + \Delta t(\delta_t f^{(2)}) \right) \tag{85}$$

with Δt the time step. One advantage of this semi-Lagrangian approach is that for vertical walled structures (e.g., cylindrical), there is no complex remeshing required as the free surface is updated (see [16] for details). For structures with curved walls (e.g. Wigley hull), however, both a different material derivative and remeshing should be used [13, 37](detailed later).

Evaluating the various terms in Eqs. 85 requires, in addition to having the potential function and its normal derivatives, also knowing time derivative of the

potential. As indicated before, in the NWT, the latter are obtained by solving a second Laplace equation for the time derivative of the potential $\partial \phi / \partial t$, as a BIE similar to Eq. 77. Additionally, values of the first- and second-order tangential derivatives of most of these fields must be computed on the moving parts of the boundary (i.e., the free surface and moving rigid bodies if any). As indicated in earlier work [10], the accurate computation of these derivatives is as important as that of the BEM solution, to reduce overall numerical errors (e.g., on mass and energy conservation). Details of the higher-order free surface representation used in the NWT are given in the next section, as well as expressions of tangential derivatives.

4.2.3 Boundary representation and curvilinear coordinate transformation

A standard approach in many ocean and naval engineering applications has been to use B-spline elements to represent boundary surfaces [38, 39] The boundary geometry and field variables are piecewise-interpolated in betweencollacation nodes using cubic B-spline boundary elements, which ensure inter-element continuity of the surface slope. For the purpose of numerical integration in the BIE, these elements, whose shape functions are defined in the physical space (x, y, z) are each locally expressed using intrinsic coordinates (ξ, η), by way of a curvilinear coordinate transformation with Jacobian $\mathbf{J}(\xi, \eta)$ (Fig. 29).

Additionally, to apply boundary conditions and specify corner conditions in the model, tangential derivatives and curvature must be computed at collocation points. This is done in a local curvilinear coordinate system $(\mathbf{s}, \mathbf{m}, \mathbf{n})$, which is not necessarily orthogonal and whose tangential vectors are defined as [10, 40] (Fig. 29),

$$\mathbf{s} = \frac{1}{h_1} \frac{\partial \mathbf{x}}{\partial \xi} \quad \text{and} \quad \mathbf{m} = \frac{1}{h_2} \frac{\partial \mathbf{x}}{\partial \eta}, \tag{86}$$

with,

$$h_1 = \left|\frac{\partial \mathbf{x}}{\partial \xi}\right|, \quad h_2 = \left|\frac{\partial \mathbf{x}}{\partial \eta}\right|. \tag{87}$$

Following Fochesato et al. [40] orthogonal tangential vectors $(\mathbf{s}, \mathbf{m}')$ are defined (Fig. 29) and used to compute both tangential derivatives. We have,

$$\mathbf{m}' = \frac{1}{\sqrt{1-\kappa^2}}\mathbf{m} - \frac{\kappa}{\sqrt{1-\kappa^2}}\mathbf{s}, \tag{88}$$

with $\chi = \mathbf{s}\cdot\mathbf{m} \in [-1,1]$, so that $\mathbf{s}\cdot\mathbf{m}' = 0$. With these definitions, the unit normal vector is defined as (Fig. 29),

$$\mathbf{n} = \mathbf{s} \times \mathbf{m}' = \frac{1}{\sqrt{1-\kappa^2}}\mathbf{s} \times \mathbf{m}, \tag{89}$$

and the Jacobian of the curvilinear coordinate transformation $(x,y,z) \to (\xi,\eta)$ as,

$$\mathbf{J}(\xi,\eta) = \left\{\frac{\partial \mathbf{x}}{\partial \xi}, \frac{\partial \mathbf{x}}{\partial \eta}, \mathbf{n}\right\}^{\mathrm{T}}, \tag{90}$$

with $\mid \mathbf{J}(\xi,\eta) \mid = h_1 h_2$.

In this local orthogonal curvilinear system, the gradient operator is given by,

$$\nabla \equiv \frac{\partial}{\partial s}\mathbf{s} + \frac{\partial}{\partial m'}\mathbf{m}' + \frac{\partial}{\partial n}\mathbf{n} \tag{91}$$

$$\frac{\partial}{\partial s} = \frac{1}{h_1}\frac{\partial}{\partial \xi} \quad ; \quad \frac{\partial}{\partial m} = \frac{1}{h_2}\frac{\partial}{\partial \eta} \tag{92}$$

$$\frac{\partial}{\partial m'} = \frac{1}{\sqrt{1-\kappa^2}}\frac{\partial}{\partial m} - \frac{\chi}{\sqrt{1-\kappa^2}}\frac{\partial}{\partial s} \tag{93}$$

$$\nabla \equiv \left(\frac{\partial}{\partial s} - \kappa\frac{\partial}{\partial m}\right)\mathbf{s} + \left(\frac{\partial}{\partial m} - \kappa\frac{\partial}{\partial s}\right)\mathbf{m} + \frac{\partial}{\partial n}\mathbf{n} \tag{94}$$

4.2.4 Cubic B-spline representation of BEM

In the present NWT, bi-cubic B-spline are used to interpolate all the field variables on the boundary (coordinates,velocity potential and it's normal derivative). The goal of this interpolation is to obtain a smooth representation with continuous first- and second-derivatives, both on the surface of each element Γ_e^k and at each
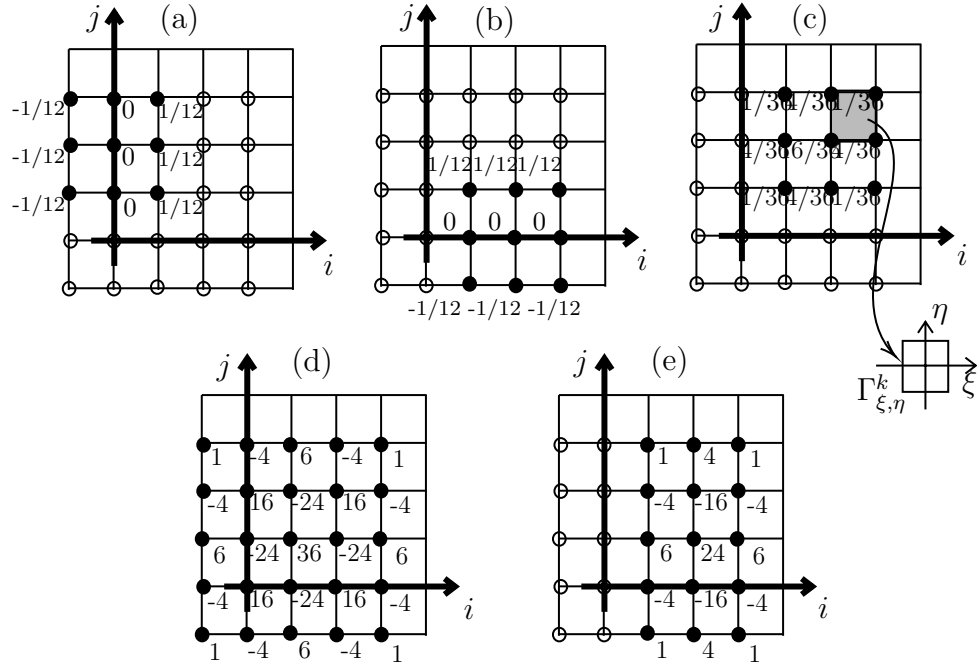
Figure 30: Tabulated coefficients of 2D B-Splines for a variety of cases and end conditions as input to the matrix of control point coefficients $M_{ij}^{p,m}$. The numeric set is defined in a way in which one of the corners of the 2D plane is in the center of the $i-j$ axis and activated patch control point coefficients are marked by $\bullet$; (a) with assumption of partial derivative known in the direction of "i"; (b) with assumption of partial derivative known in the direction of "j"; (c) regular element coefficients (d) not-a-knot condition at the corners (e) not-a-knot condition at edges. For the physical parameters $\partial\phi/\partial n$ and $\mathbf{x}$, not-a-knot condition has been set as auxiliary equations, while for the field variable ϕ, the values of the tangential derivatives are known in the corners and edges of the boundary (Specifically on Dirichlet/Neumann boundaries) and the end known derivative conditions has been used as Auxiliary equations.

collocation node $\mathbf{x}_j$. This approach was first used in a 2D-BEM-NWT by Liu et al. [41].

For structured curvilinear grids made of quadrilateral elements, a bi-cubic B-spline interpolation can be defined over each element based on the product of two 1D cubic B-splines specified in directions ξ (p) and η (m), respectively In 1D, a B-spline patch [39], $B_m(\mu)$ ($n = 1, \ldots, 4$) is defined, e.g., along grid line m connecting N_m nodes in between two grid edges of boundaries, as

$$
B_n(\mu) = \sum_{l=-1}^{2} C_{nl}\,\mu^{2-l} \quad \text{with,} \quad C_{nl} = \begin{bmatrix} -1 & 3 & -3 & 1 \\ 3 & -6 & 3 & 0 \\ -3 & 0 & 3 & 0 \\ 1 & 4 & 1 & 0 \end{bmatrix} \quad \text{and} \quad \mu \in [-1, 2].
\tag{95}
$$

The spline approximation of each property is expressed within each two-node segment of grid line m, $i = 1, ..., N_m - 1$ (marked as superscript i) as,

$$
f^i(\mu) = \sum_{m=-1}^{2} B_m(\mu)\,q_{i+m} \quad \text{with} \quad \mu \in [0, 1] ,
\tag{96}
$$

where q_i denote $N_m + 2$ control point values (i.e., spline coefficients). [It is easy to verify that the definition of 1D B-splines in Eq. 95 enforces, by construction, the continuity of the first-derivative of the property in between each two-node segment, i.e., $f'^{i-1}(1) = f'^i(0)$.] Expressing N_m Eqs. 96 at each segment extremity (i.e., for $\mu = 0/1$), noting from Eq. 95 that $B_{-1}(0/1) = 1/6$ or 0, $B_0(0/1) = 4/6$ or $1/6$, $B_1(0/1) = 1/6$ or $4/6$, $B_2(0/1) = 0$ or $1/6$, and assembling the resulting equations into a matrix form yields (subscript $i = 1, ...N_m$ now denoting nodes on the considered grid line m),

$$
f_i = \sum_{j=0}^{N_m+1} M_{ij}^m q_j \quad \text{with} \quad M_{ij}^m = \frac{1}{6} \begin{bmatrix} 1 & 4 & 1 & & & & \cdots & 0 \\ & 1 & 4 & 1 & & & & \vdots \\ & & \ddots & \ddots & \ddots & & & \\ \vdots & & & & 1 & 4 & 1 \\ 0 & \cdots & & & & 1 & 4 & 1 \end{bmatrix}
\tag{97}
$$

where M_{ij}^m is of size $N_m \times (N_m + 2)$.

Hence, given nodal values of property f_i $(i = 1, ..., N_m)$ along grid line m, two additional equations are needed to solve this system of equations for coefficients q_j $(j = 0, ..., N_m+1)$, to specify values of q_0 and q_{N_m+1} and make the matrix square with dimension $(N_m + 2)$. As detailed later, these will be provided by boundary conditions prescribed at each extremity of the considered grid line.

In 2D, each quadrilateral boundary element Γ_e^k, is given its nodal values $f^{i,j}$ $(i = 1, \ldots, N_m; j = 1, \ldots, N_p)$ over a 2D regular grid. Thus we have,

$$f^k(\xi, \eta) = \sum_{p=-1}^{2} \sum_{m=-1}^{2} B_p(\mu(\xi, \xi_0)) B_m(\mu(\eta, \eta_0)) \, q_{i+m,j+p} \tag{98}$$

where $\mu \in [0, 1]$; $\xi, \eta \in [-1, 1]$; $B_m(\mu)$ and $B_p(\mu)$ are 1D B-splines given by Eq. 95, q_{ij} are $(N_m \times N_p)$ control points, element k is defined within a 16-node B-spline patch based on the value of its lower left corner coordinates (ξ_0, η_0) (Figs. 30) and, accordingly, μ is given by,

$$\mu(\chi, \chi_o) = \chi_o + \frac{\chi + 1}{2} \tag{99}$$

with $\chi = \xi$ or η, in each of the curvilinear direction of the reference element $\Gamma_{\xi,\eta}$, and $\chi_o = \xi_o$ or $\eta_o = 1/2$, -1/2 or 3/2, depending on which of the 9 quadrilaterals defined is selected(Figs. 30).

Proceeding as in 1D, we find for the central quadrilateral in the patch and $\mu = 0$ in both directions (i.e., node $(i, j) = (1, 1)$ in Fig. 30c),

$$f_{ij} = \sum_{p=-1}^{2} \sum_{m=-1}^{2} B_p(0) B_m(0) \, q_{i+m,j+p} \quad \text{for} \quad i = 1, \ldots, N_m; j = 1, \ldots, N_p, \tag{100}$$

Combining Eqs. 98 to 100, the 2D shape functions for bi-cubic B-splines to use in Eq. 77 for interpolating property f, of nodal values f_a^k over element k, can formally be expressed as,

$$S_{a(p,m)}(\xi, \eta) = B_p(\mu(\xi, \xi_o)) \, B_m(\mu(\eta, \eta_o)) \, M_{al}^{p,m^{-1}} \tag{101}$$

with $m, p = -1, \dots, 2$; $a(m, p) = 4(m+1) + p + 2 = 1, \dots, N_e = 16$ (see numbering in Fig. 30) , and $M_{al}^{p,m^{-1}}$ denoting the inverse of the matrix of dimension $(N_s \times N_s)$, with $N_s = ((N_m + 2) \times (N_p + 2))$, resulting from applying Eq. 100 to express nodal values of the interpolated property f_l over the 2D grid, as a function of those of the control points q_l, given $l = (j-1)(N_p + 2) + i = 0, \dots, N_s$, for $(i = 0, \dots, N_p + 1)$ and $(j = 0, \dots, N_m + 1)$. Note that, as in 1D, 2 more control points (and property) values are used for each line m or p, $q_0^{m,p}$ and $q_{N_{m,p}+1}^{m,p}$, which are related to the boundary conditions at each extremity of these lines ($2 * N_m + 2 * N_p + 4$ auxiliary equations are needed to solve the system of matrix M).

Finally, to compute the $s-$ and $m-$derivatives of property f over element k (including at grid nodes) using Eq. 95, one needs the $\xi-$ and $\eta-$ derivatives of the shape functions given by Eq. 101, which are proportional to $B_p'(\mu)B_m(\mu)$ and $B_p(\mu)B_m'(\mu)$, respectively, where the dash indicates the derivative of the 1D B-spline of Eq. 95 with respect to μ,

$$\frac{\partial B_n}{\partial \mu}(\mu) = \sum_{l=-1}^{2} (2 - l) \, C_{nl} \, \mu^{1-l} \tag{102}$$

with, based on Eq. 99, $\partial \mu / \partial(\xi, \eta) = 1/2$. Figs. 30 a and b show values of coefficients $B_p'(0)B_m(0)$ and $B_p(0)B_m'(0)$.

4.2.5 Auxiliary equations for matrix of control point coefficients

As mentioned before, the interpolating condition in matrix $M_{ij}^{p,m}$ in Eq. 101 is not sufficient to determine the B-spline Curve(in 2D) or surfaces (in 3D). This usually happen by imposing properties (determined or undetermined) related to $S(\xi, \eta)$, $S'(\xi, \eta)$, $S''(\xi, \eta)$ and $S'''(\xi, \eta)$ at the end points of B-spline curves (surfaces). A detail study of such auxiliary equations are discussed in Behforouz et al. [42] and Barskey [43].

For any type of spline, typically the end tangential value of such a curve is

used for an auxiliary equation. This has been shown to have the most accurate representation of interpolating property f. However in the NWT, the calculation of the tangential derivative of property f (e.g. $\partial\phi/\partial n$ and $\mathbf{x}$) at each time step is not trivial.

An easy and commonly used approach to solve this problem is to consider the second derivatives at the ends points as zero. In wave mechanics, this will not be an ideal condition since the second derivative of the wave profile at boundaries would not necessarily be equal to zero. Another approach is to consider the third derivative at the first or last two end segments of a spline are equal.This is refered to as the *not-a-knot*. This condition reads as

$$f_i = \sum_{j=0}^{N_m+1} M_{ij}^m q_j \quad \text{with} \quad M_{ij}^m = \frac{1}{6} \begin{bmatrix} 1 & -4 & 6 & -4 & 1 & \dots & 0 \\ 1 & 4 & 1 & & & & \vdots \\ & 1 & 4 & 1 & & & \\ & & \ddots & \ddots & \ddots & & \\ \vdots & & & 1 & 4 & 1 & \\ 0 & \dots & & & 1 & 4 & 1 \\ 0 & \dots & 1 & -4 & 6 & -4 & 1 \end{bmatrix} \quad (103)$$

De-Boor shown that cubic spline interpolation with the not-a-knot side condition converges to any C^2 without any mesh-ratio restriction as the mesh size goes to zero [44]. This method is widely used for problems where there are no information about the end points of the B-splines. Most CAD softwares use this method for defining B-Spline segments. The coefficients for *not-a-knot* are shown in Fig. 30 for corners(d) and edges(e). These auxiliary equations are used for interpolating parameter $\mathbf{x}$ and $\partial\phi/\partial n$ where the information of their derivatives are not known prior to solution of the BIE in Eq. 77.

Although, these auxiliary equation definition are required for evaluating some fluid properties at the boundary, where $f = \phi$, the values of the tangential derivatives can be extracted using the definition of the velocity compatibility condition

117

(see Fig. 31 for a simple 2D example) at corners and edges of the 3D domain [1, 2, 45]. This condition reads as known auxiliary equations of end tangential derivatives and can be used to describe the interpolating B-spline ϕ at each time step. In 1D, the matrix of coefficient M_{ij}^m read as

$$f_i = \sum_{j=0}^{N_m+1} M_{ij}^m q_j \qquad \text{with} \quad M_{ij}^m = \frac{1}{6} \begin{bmatrix} -1/2 & 0 & 1/2 & ... & & 0 \\ 1 & 4 & 1 & & & \vdots \\ & 1 & 4 & 1 & & \\ \vdots & & \ddots & \ddots & \ddots & \\ 0 & ... & 1 & 4 & 1 \\ 0 & ... & 1/2 & 0 & -1/2 \end{bmatrix} \tag{104}$$

with f_0 and f_{N_m+1} replaced by tangent values at corresponding ends of the B-spline. The coefficients of end slopes in directions s and m of the local coordinate system, over element k located on edges of domain is shown in Fig. 30a,b.

4.2.6   Treatment of corners and edges in BIE

Following Grilli et al. [1, 2, 10], we define multiple nodes at corners and edges of the BEM discretization, which mark intersections of the boundary region in the computational domain, where the values of normal velocities are discontinuous and the boundary integral equation of 77 in undetermined (see Figure 31). Multiple BIEs are expressed at these locations where multiple nodes are defined, based on different values of the normal derivatives of the potential, but using a single value of potential, which must be unique at these locations. The latter condition is enforced in the BEM solution, by modifying all but one the assembled equations of a multiple node in a way that does not cause a mathematical singularity in the problem.

In a 3D space, there are both double (e.g., between the wavemaker and the free surface) and triple (e.g., where the wavemaker and free surface boundaries meet with a sidewall boundary) nodes. Thus, for double/triple nodes, there are 2/3 discretized BIEs expressed at each multiple node. To ensure uniqueness and

well-posedness of the solution, however, and in particular a single potential at a given location, 1 (in case of a double node) or 2 (in case of a triple node) of these BIEs must be modified in the final algebraic system to ensure that both the global matrix is not singular and the solution yields a single potential.

The multiple nodes can be categorize based on their boundary conditions as (see Figure 28 for reference): (i) Dirichlet-Neumann (DN) double nodes (e.g., wakemaker and free surface boundary); (ii) Neumann-Neumann (NN) double nodes (e.g., bottom and sidewall boundaries); (iii) Neumann-Neumann-Neumann (NNN) triple nodes (e.g., where the wavemaker, bottom and sidewall boundaries meet); and (iv) Dirichlet-Neumann-Neumann (DNN) (e.g., where the wavemaker, free surface and sidewall boundaries meet).

In a NWT with a moving free surface (e.g. paddle wavemaker,forward moving ship, etc.), Grilli and Subramania [2] showed that the velocity vector must be unique at double/triple nodes on the free surface, not only to obtain an accurate solution, but also for free surface multiple nodes to move to an identical location through time updating. These authors showed that if velocity is not explicitly *enforced* to be unique at multiple nodes, by modifying the algebraic BIE system in a proper way, large numerical errors will occur at and near such nodes in the BIE solution, which will grow even larger through time stepping and, eventually, will lead to instability of the solution, particularly close to strongly moving rigid boundaries. Following Grilli and Subramania's work[2], we extend the simple potential continuity condition at multiple nodes, used in earlier work, to also enforce that the numerical solution yield a unique velocity (i.e., gradient of the potential) at multiple node locations. This is done by replacing all but one of the assembled equations of a multiple node in the algebraic system, by so-called *velocity compatibility* conditions, which also include the potential continuity condition.

Following Grilli and Subramania [2], we derive discretized relationships expressing the uniqueness (compatibility) of the velocity at multiple nodes for all cases of mixed boundary conditions (e.g., DN, NN, NNN, DNN). In the following, for brevity, we only present one example of these for a DN double-node case. These relationships make the representation of the solution compatible on both sides of a corner in the sense of the study by Gray and Lutz [27] and effectively eliminate numerical singularities in the discretized solution. When using compatibility conditions at corners for solving mixed boundary value problems in simple rectangular domains, Grilli and Subramaniya [2] showed that numerical errors at corners of their 2D-NWT could be reduced to arbitrarily small values. For instance, let us choose a DN double node, located at the intersection between a piston wavemaker (denoted in BIE 77 by $l = p$) and the free surface($l = f$). the compatibility condition forced the BIE solution to compute a (corrected) value of the tangential velocity on the free surface, $\partial \phi_f / \partial s$, as a function of both the normal velocity $\partial \phi_f / \partial n$, obtained from the solution of the BIE (77) at the current time step, and the (specified) wavemaker velocity on the wavemaker node $l = p$, $\partial \phi_p / \partial n = -u_p$ (see Eq. (82)) (see Figure 31).

In the current BEM, we use this *velocity compatibility condition* to describe the end conditions for B-spline surfaces in 3D BIE. Mivehchi et. al [45] describes the concept of using compatibility conditions for curvilinear coordinates, which can be applied to a variety of discretization models with Lagrangian time updating. However, further investigation on the semi-Lagrangian time updating employed in this model shows, at least in one tangential direction of local coordinate system (s or m), the curvilinearity effect at edges are very small in compare to the computational cost of adding the curvilinear equations to the system of equations 77. We will use the property of Equation 98 to describe the end surface elements in
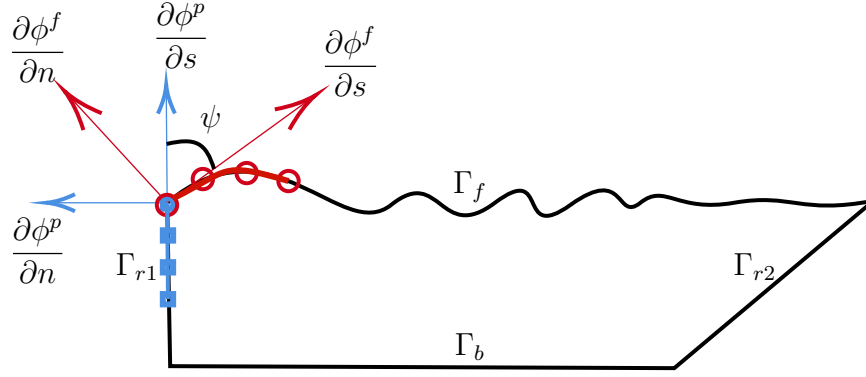
Figure 31: sketch of corner conditions over an arbitrary double nodes between Dirichlet boundary Γ_f at the point $l = f$ (□) and Neumann boundary Γ_{r1} at the point $l = p$(○) in a one dimensional B-spline description of the geometry and field variables, respective elements and local coordinate system. ψ is the angle between the double nodes corresponding elements local coordinate system.

system of matrix (see also Figure 30). Note that only the field variable of ϕ is modified based on the velocity compatibility condition and for other variables, the *not-a-knot* condition is used.

In the BIEs, for imposing the compatibility condition , for double corner nodes, where each node is related to a different B-spline patch, there are 3 sets of B-spline control polygons (in 2D) or surfaces (in 3D) that must be defined.

For calculating the tangential derivatives on each one of these B-spline surfaces, the calculated or predetermined field variables of ϕ are used. For the Neumann boundary conditions , this value is calculated in the BIE, while for a Dirichlet boundary condition, this value has been predefined, thus this predefined value have a large effect on the result of the BIE. Back to out double node example between free surface point $l = f$ and wavemaker point $l = p$, one can define the corner compatibility condition as [1]

$$\nabla \phi^f = \nabla \phi^p \tag{105}$$

Based on Figure (31) , one can define the tangential velocities as

121

$$\phi_s^f = -\frac{\mathbf{n}_f \cdot \mathbf{n}_p}{\mathbf{n}_p \cdot \mathbf{s}_f} \phi_n^f + \frac{1}{\mathbf{n}_p \cdot \mathbf{s}_f} \phi_n^p \tag{106}$$

$$\phi_s^p = \frac{1}{\mathbf{n}_f \cdot \mathbf{s}_p} \phi_n^f - \frac{\mathbf{n}_f \cdot \mathbf{n}_p}{\mathbf{n}_f \cdot \mathbf{s}_p} \phi_n^p \tag{107}$$

these are equivalent to knowing the first derivative of endpoints of B-splines for interpolated field variable ϕ. Therefore, one can use these values in the auxiliary equations used to define the matrix of B-spline coefficients M_{ij}^m (for 2D patch coefficients see Figure30).

$$\frac{-1}{12} f_{-1} + \frac{1}{12} f_1 = \phi_s^f \tag{108}$$

For Surface elements, the number of additional equations for solving the system of matrix similar to 104 is equal to $2N_i + 2N_j + 8$. To do this, an algorithm was developed to reorient all elements over each surface in a way that the local s and m derivatives are set to be initially in the same direction in the global coordinate system. In that way, over the edge of a B-spline surface, the compatibility condition is imposed using Equation 108. Based on the double node implementation of corners, we prescribe $2N_i + 2N_j + 4$ *compatibility conditions*. On the corners, 4 additional equations are required to couple the two directional derivatives is s and m directions. If these local coordinates are orthogonal, using $\frac{\partial^2}{\partial s \partial m} = 0$ is the most suitable case to be used. After solution of system of equation descritized with specified end condition, tangential velocities can be updated using the matrix form of equation (105) at the extremities of the free surface and thereafter, re-griding will be applied to the free surface nodes.

4.2.7 Treatment of intersection with surface piercing object

The BEM-NWT solution for SL time updating is defined in way that nodes on the free surface are restricted to move vertically. This is generally fine if boundaries
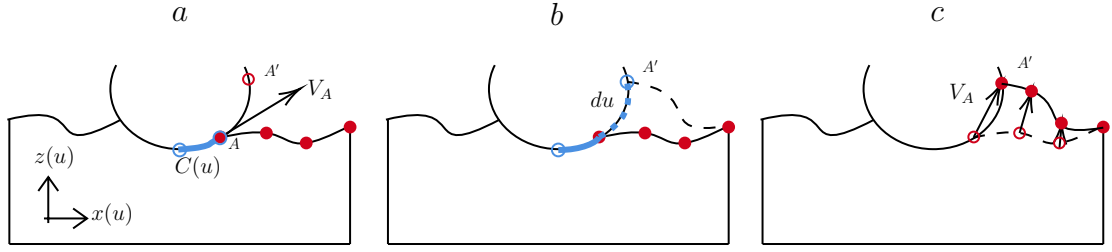
Figure 32: Method of updating intersection node (here node A) with free surface over an arbitrary structure. The nodes over free surface are marked by ($\bullet$) and nodes and curve over structure are marked with ($\bullet$), : (a) node A is moving with velocity V_A to its new location A'; (b) since this node should satisfy kinematic free surface boundary condition, and from Equation 109, the travel length du is calculated; (c) The value of du and it's projection is used for time advancing of free surface nodes.

that pierce the free surface only include vertical walls. In this case, we have the traditional kinematic free surface boundary condition which can be written compactly as Eq. 79. If we have an object with a curved wall however, we no longer want to track $\eta(x, y, t)$, but a point which moves along the hull (i.e., with a changing (x,y) coordinate). To accommodate this requirement we use the Arbitrary Eulerian Lagrangian Method (ALE) [37]. If point A is the intersection point between the free surface and the body , this point must physically always stay on both the body surface and free surface assuming connectivity of the elements does not change. The KFSBC is satisfied with the constraint that the velocity of point A must be parallel with the tangent vector on the body surface (i.e. $V_A \cdot \mathbf{n}_A = 0$). Defining a local coordinate system $\mathbf{e} = (e_x, e_y, e_z)$, on the body, we can define a series of curves with coordinate $\mathbf{x} = C(u)$ over the body, where $u(t)$ is the corresponding parametric instantaneous motion of point A. The corresponding velocity of point A then can be calculated as

$$\mathbf{V}_A = \frac{du}{dt}\mathbf{e} \tag{109}$$

Since the point A should also satisfy kinematic free surface boundary condi-

tions, we substitute Eq. 109 into Eq. 79 and solve for du/dt

$$\frac{du}{dt} = (\frac{\partial \phi}{\partial z} - \nabla \phi \cdot \nabla \eta)/(Z_u - X_u \eta_x - y_u \eta_y) \qquad (110)$$

Solving for u in equation 35 allows one to determine coordinate $\mathbf{x}$. By assuming the unit normal vector at point A is equal to $\phi_n/e \cdot n$ we have

$$\mathbf{V}_A = \frac{du}{dt}\mathbf{e} = \frac{\phi_n}{e \cdot n}\mathbf{e} \qquad (111)$$

substituting this expression into in Eq, 80 yields

$$\frac{\delta \phi}{\delta t} = -g\eta - \frac{1}{2}\boldsymbol{\nabla}\phi \cdot \boldsymbol{\nabla}\phi + \mathbf{e} \cdot \boldsymbol{\nabla}\phi\frac{du}{dt} \qquad (112)$$

and therefore this equation can be used for time advancing the free surface node correspond to point A. The last modification is to find the position of the rest of nodes over free surface. By knowing the value of du/dt and by describing the curve $C(u)$ over the body ,the time derivative position vector $d\mathbf{x}/dt$ in global coordinate can be found and finally, the new position of points over the free surface can be updated by this value. Zhang and Kashiwagi [37] showed a variety of applications of this method.

4.2.8 BEM solution of Laplace's equation with FMM

In the standard BEM discretization, the BIE is transformed into a sum of integrals over each element[10, 6, 46], which are computed by numerical integration after transforming each element k, of boundary Γ_e^k, from the physical space to a standard 2D reference element of domain $\Gamma_{\xi,\eta}$ defined with curvilinear coordinates (ξ,η), by way of a Jacobian matrix $\mathbf{J}^k$. Substituting B-spline shape functions $S_j(\xi,\eta)$, into Equation 77, gives the linear algebraic system of equations (i and

$j = 1, ... N_\Gamma)$,

$$\alpha(\mathbf{x}_i)\,\phi(\mathbf{x}_i) =$$

$$= \sum_{k=1}^{M_\Gamma} \int_{\Gamma_e^k} \left[\frac{\partial \phi}{\partial n}(\mathbf{x}) - \phi(\mathbf{x})\frac{\partial}{\partial n} \right] G(\mathbf{x} - \mathbf{x}_i)\,\mathrm{d}\Gamma \tag{113}$$

$$= \sum_{k=1}^{M_\Gamma} \int_{\Gamma_{\xi,\eta}} \left[S_j^{\phi_n}(\xi,\eta)\frac{\partial \phi_j}{\partial n} - S_j^{\phi}(\xi,\eta)\phi_j\frac{\partial}{\partial n} \right] G(\mathbf{x}(\xi,\eta) - \mathbf{x}_i)\,|\mathbf{J}^k(\xi,\eta)|\,\mathrm{d}\xi\mathrm{d}\eta \tag{114}$$

$$= K_{ij}^d \frac{\partial \phi_j}{\partial n} - K_{ij}^n \phi_j \tag{115}$$

where the summation on repeated indices j is implicit and either the potential or its normal derivatives are specified as Dirichlet (D) or Neumann (N) or complementary boundary conditions. For B-splines, shape functions differ for each property that is interpolated (Eqs. 101), and variation in properties is denoted by the superscript.

The solution of the algebraic system of Eqs. 115 can efficiently be computed using GMRES [47], a Krylov iterative solver with a $\mathcal{O}(N_\Gamma^2)$ numerical complexity. Typically, the most computationally intensive part in such a standard BEM solution is the computation and assembling of the fully populated Neumann and Dirichlet system matrices, $[K_{ij}^n]$ and $[K_{ij}^d]$, respectively, which has a similar numerical complexity.

Using the *Fast Multipole Method* (FMM), the BIE influence coefficients in matrices $[K_{ij}^n]$ and $[K_{ij}^d]$ are only integrated for small r values (based on a FMM distance criterion), these are referred to as local or near-field FMM computations. For larger distances of r, a multipole approximation of the Greens function is applied, which both simplifies and accelerates computations; these are referred to as distant or far-field FMM computations [18, 48]. The Green's function in the multipole expansion is defined as

$$G(\mathbf{x}_i - \mathbf{x}_j) =$$

$$\sum_{m_x=0}^{P-1} \sum_{m_y=0}^{P-m_x-1} \sum_{m_z=0}^{P-m_x-m_y-1} ([x_i - x_\Lambda] + [x_M - x_j])^{m_x} ([y_i - y_\Lambda] + [y_M - y_j])^{m_y}$$

$$([z_i - z_\Lambda] + [z_M - z_j])^{m_z} \frac{\partial_x^{(m_x)} \partial_y^{(m_y)} \partial_z^{(m_z)} G(\mathbf{x}_\Lambda - \mathbf{x}_M)}{m_x! m_y! m_z!} + O(\theta^P). \tag{116}$$

in which P is the order of expansion and the distance between to point $\mathbf{x}_i$ and $\mathbf{x}_j$ can be decomposed into $\mathbf{x}_i - \mathbf{x}_j = (\mathbf{x}_i - \mathbf{x}_\Lambda) + (\mathbf{x}_\Lambda - \mathbf{x}_M) + (\mathbf{x}_M - \mathbf{x}_j)$. More specifically, to decide how to approximate (or even neglect) interactions, the FMM uses a divide-and-conquer strategy based on the distance between two points. Importantly, by assigning intermediate points (e.g., the centers of groups of nodes or elements of the boundary mesh) and applying the binomial theorem, one is able to manipulate multipole coefficients that only need to be computed once, instead of directly evaluating the BIE between each element and node (see Harris et al., 2018 [16] for details). By using this method, the BIE Equations of 77(or in matrix form 115) are converted to the form

$$\alpha(\mathbf{x}_i)\phi(\mathbf{x}_i) = \left([K_{ij}^d]_{\text{near}} \frac{\partial\phi}{\partial n}\Big|_j - [K_{ij}^n]_{\text{near}} \phi_j \right) + \left([K_{ij}^d]_{\text{far}} \frac{\partial\phi}{\partial n}\Big|_j - [K_{ij}^n]_{\text{far}} \phi_j \right) \tag{117}$$

in which the near-field BEM influence coefficients are computed the classical way by direct integration of the Green's function and the far-field ones are approximated based on using Eq. 116.

If efficiently implemented and assuming N_Γ is more than a few thousand, the computational time of the FMM should scale with $\mathcal{O}(N_\Gamma)$. This is much faster than the solution of the complete BEM system with the best iterative solvers. Several variations have been proposed of the implementation of the FMM on parallel clusters [48, 49], which generally rely on domain decomposition, whereby the
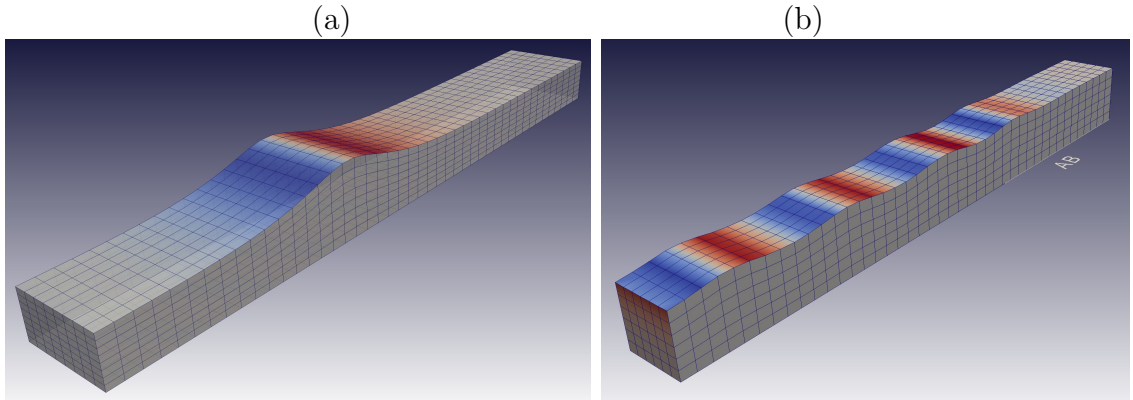
Figure 33: Numerical Wave Tank (NWT) setup for (a) propagation of exact solitary wave; (b) numerically exact stream function wave generated by a paddle wavemaker and absorbing beach (AB). values of $\partial \phi / \partial n$ are plotted on the free surface as color scale with red positive and blue negative values.

FMM is first applied on each processor over some region of space and then results are combined. Here, we make use of the ExaFMM library developed by Yokota and Barba [50], which uses Cartesian multipole expansions of the Green's function, and the dual-tree traversal approach of Dehnen [51] (see Harris et.al. [16]).

Evaluating the BIE of Eq.115 and matrix terms $[K_{ij}^d]_{\text{near}}$ and $[K_{ij}^n]_{\text{near}}$ requires integrating complex kernels over near-field boundary element k, which can become singular when $r_l \to 0$ in the Green's functions. For quadrangular elements, the weakly singular integrals are desingularized by way of a tensor product of Gauss integration.

The coefficients α in the BIE are found by applying the rigid mode method (e.g., Grilli et al. 1989), which expresses that for a Dirichlet problem with a homogeneous $\phi = 1$ value specified over the entire boundary, the discretized BIE solution must yield $\partial \phi / \partial n = 0$; the α coefficients are then found as the residuals of this Dirichlet problem.

4.3 Application
4.3.1 Solitary wave propagation over constant depth: investigating the global accuracy of the solution

To demonstrate and validate our development compatibility conditions, we simulate the generation and propagation of a solitary wave over constant depth h, inside a numerical wave tank (NWT),and comparing result to [10]. To demonstrate convergence, we measure the the values of mass and energy error in the domain over a range if Courant numbers. Such a solitary wave should keep a constant form in celerity, volume m above $z = 0$ and total energy e while propagating. Hence, numerical errors in the computations give a measure of discretization and time step effects on the global numerical accuracy.

Figure 33a shows a nwt domain of the three-dimensional model set-up. The domain length (L') is 15 times the depth h_0 and its width (W') is set to $2h_0$. Two-dimensional solitary waves are generated using the fully non-linear method by Tanaka [52]. These are made three-dimensional by specifying the two-dimensional profiles for each vertical cross-section of domain in width of three-dimentional NWT. Waves are initially defined by their shape η, potential ϕ_f and $\frac{\partial \phi}{\partial n}$ on the free surface, at time $t = 0$. A strongly non-linear wave of height $H_0 = 0.6h$ is initially specified, with its crest located at $\frac{x}{h} = 5.5$, and propagated in various spatio-temporal discretizations. For this wave, Tanakas method provides, $m_0 = 3.87765$ and $e_0 = 1.58547$.

At each time step, the numerical error on the global conservation of mass and total energy of the solitary wave is computed. During propagation, both mass and energy of the solitary wave should theoretically stay constant, as there is no mass or energy input or output into the NWT. Hence, we define the numerical error on wave volume as: $\epsilon_m = |(m(t) - m_0)/m_0|$, with the instantaneous solitary wave
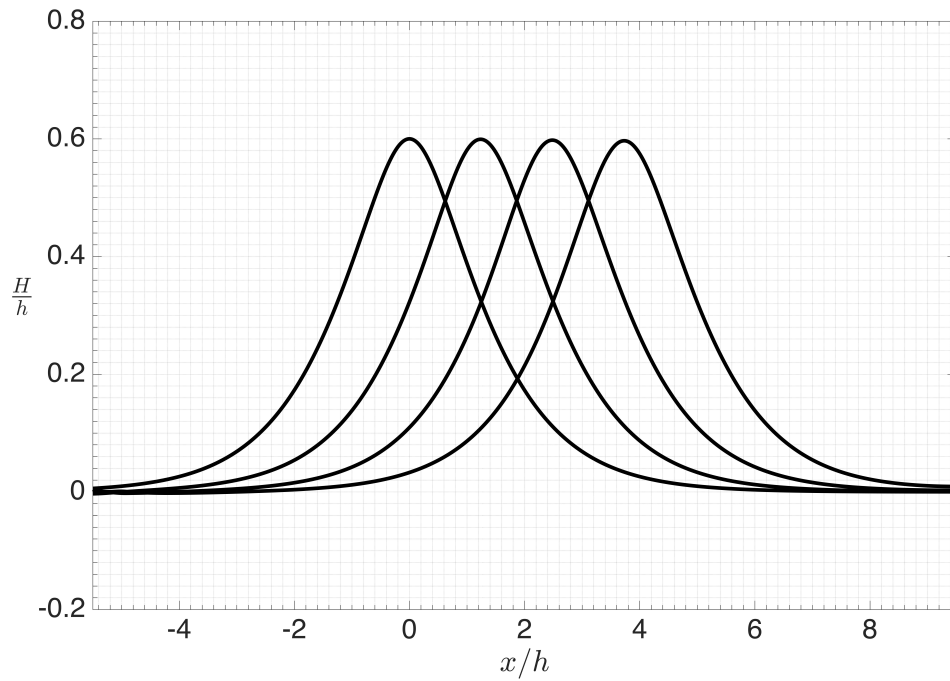
Figure 34: Propagation of a very steep solitary wave. The solitary wave profile and its initial potential and normal velocity on the free-surface are computed using Tanakas method [52]. The crest is initially located at $x' = x/d = 0$ and propagate with celerity $c = \sqrt{gd}$.Similar to Grilli et.al. [10] we asses the convergence of Energy and Mass error for a solitary wave with non-dimensional height of $H' = H/d = 0.6$ and the numerical wave tank dimensions of 15 length to depth and 2 width to depth and for duration of $t' = t\sqrt{g/d} = 4$.

volume being computed in the NWT as:

$$m(t) = \int_{\Gamma_f} z \, n_z \, d\Gamma \tag{118}$$

with Γ_f denoting the free surface boundary, and m_0 the theoretical value obtained with Tanaka's method. Similarly, we define the numerical error on total wave energy as $\epsilon_e = |(e(t) - e_0)/e_0|$, with the instantaneous total energy being computed as the sum of kinetic and potential energy, as:

$$e(t) = \frac{1}{2}\rho \int_{\Gamma} \phi \frac{\partial \phi}{\partial n} \, d\Gamma + \frac{1}{2}\rho g \int_{\Gamma_f} z^2 n_z \, d\Gamma \tag{119}$$

and e_0 being the theoretical value obtained with Tanaka's method. In both equations, integrals are evaluating only over the free surface, which allows computing the part of the volume and potential energy error corresponding to the wave only, which is a stricter condition than computing relative errors with respect to the entire NWT mass and energy and thus avoids underestimating errors for large NWTs in which much of the water is not in motion.

Three different spatial discretizations are used in the computations, with initial distances between nodes $\frac{Dx}{h_0} = 0.25$,0.33 ,and 0.50 respectively ($Mx = 60$,45 , and 30), and $\frac{Dy}{h_0} = 0.50$ ($My = 4$) on the free surface Γ_f and bottom Γ_b; $\frac{Dz}{h_0} = 0.25(Mz = 4)$ on the lateral boundaries $\Gamma_r 1$ and $\Gamma_r 2$. Ten Gauss points are used per direction in the integrations ($NL = 10$) and adaptive integration is specified in corner/edge elements. Then expansion terms are used for the FMM representation of distance functions.

Computational errors on mass and energy conservation: $m(t)$ and $e(t)$ (Equations (118) and (119)) are calculated as a function of time for the propagation of the wave over four time units, $t' = t\sqrt{g/h} = 4$, representing a varying number of time steps in each case based on Courant number. This also corresponds to a horizontal distance about five times the depth.

Computational errors are shown in Figures 35 and 36 and compared with three different discritization methods of MII from Grilli et al.[10], B-spline with only not-a-knot treatment from Harris et al.[16] and a B-spline with treatments of end slope for variables ϕ and not-a-knot for variables $\mathbf{x}$ and $\partial\phi/\partial n$ with velocity compatibility condition (VCC) in this study. Maximum error curves are given as a function of Courant number and for different spatial discretization with the optimized Courant number of 0.5. We first see that the smaller Dx/h_0, the smaller the numerical errors. This indicates the convergence of results in the 3D-NWT with an increased resolution of the discretization (i.e., with N_Γ or M_Γ). More specifically, we see that there is more than one order of magnitude gain in accuracy in energy error when Dx/h_0 is divided by two. The B-spline element is shown to have better representation of the geometry on the free surface, leading to higher accuracy (almost two order of magnitude for treatment of B-spline with only *not-a-knot* and one order of magnitude for treatment of corners with velocity compatibility condition), compared to MII elements used by Grilli et al [10]. However for energy error, there is no significant benefit between MII and B-spline with VCC,but the method shows a better convergence with one one order of magnitude when compared to the B-spline with only *not-a-knot* treatment. Further investigation shown that the not-a-knot method has a weekly convergence in its derivatives values [53]. This will cause lack of accuracy in calculation of local coordinate system (s, m, n), therefore numerical inaccuracy in calculation of $\partial\phi/\partial n$ at edges and corners. It is to believe, this will cause more numerical error in total energy error in compare to total volume error in B-splines.

4.3.2 Solitary wave reflection over the vertical wall

One of the test cases for investigating the effect of *corner conditions* on the accuracy of calculating the tangential derivatives, is the behavior of the numerical
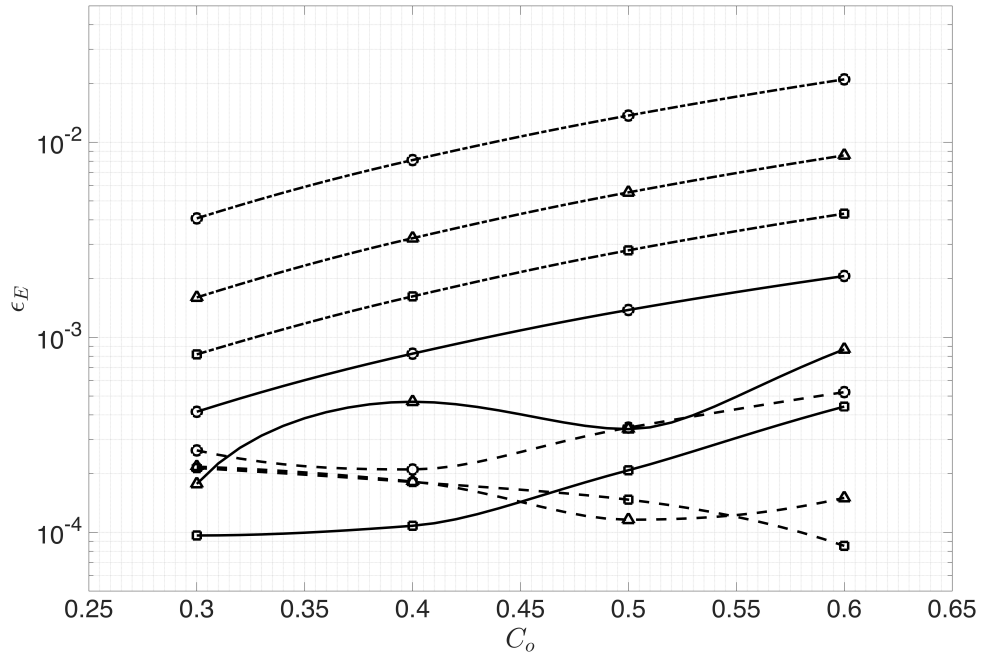
Figure 35: Convergence of Energy error for the three different grid spacing of $dx = 0.50$ (∘) , $dx = 0.33$ (△) and $dx = 0.25$ (▫); The Maximum energy and mass error for 3 different method is presented. Grilli et.al.[10] with (- - -); Harris et.al.[16] with dotted line (⋯⋯); and current simulations with (——); Current method shown better convergence in compare to not-a-knot method used by Harris et al.[16] and no significant improvement in compare to MII [10].
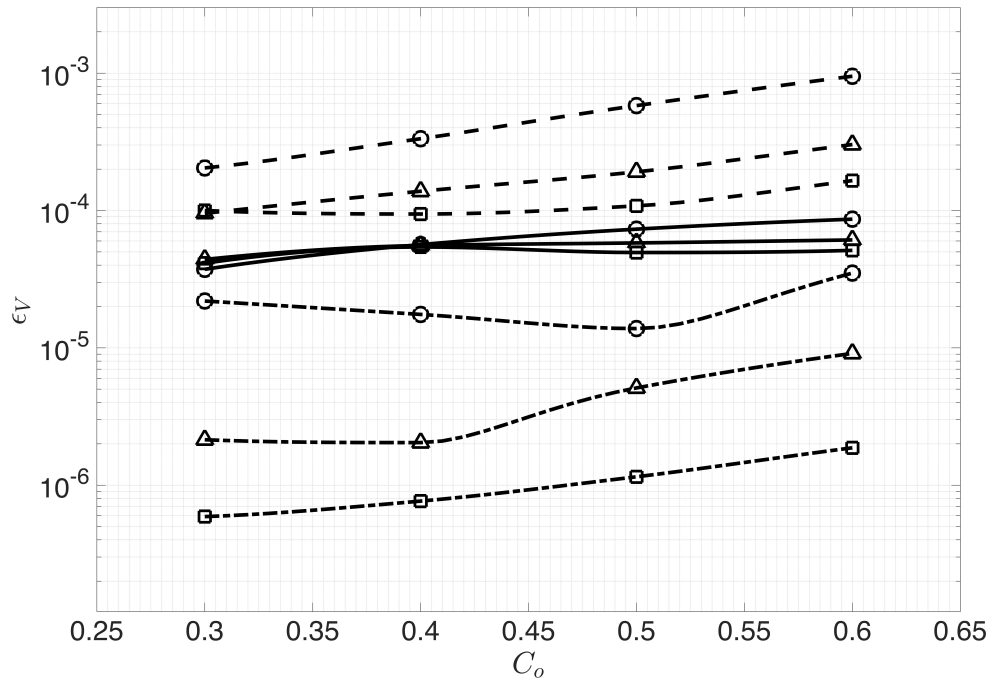
Figure 36: Convergence of Mass error for the three different grid spacing of $dx = 0.50$ (o) , $dx = 0.33$ ($\triangle$) and $dx = 0.25$ ($\square$); The Maximum energy and mass error for 3 different method is presented. Grilli et.al.[10] with (- - -); Harris et.al.[16] with (······) and current simulations with (——); not-a-knot condition despite is poor convergence in Energy error, has better convergence in volume error.

wave tank with reflection of a solitary wave at a vertical wall. There is no way of comparing the treated and untreated B-spline end conditions for the reflection of a solitary wave since the stability of the numerical simulation in corners causes the untreated model to fail with a maximum numerical error of energy equal to 7.61×10^{-1}. This error appears as a very steep , non-physical rise of the wave elevation in corners as seen in Figure 38.

The size of the domain is slightly modified in-order to capture the nonlinear reflection tail of the solitary wave.The exact waves are generated, at the location $x' = -4.0$ of a tank with length $L' = 20$ ($x_L \in [-10, 10]$)and width $W' = 2$ with $dx' = 0.25$. This result is obtained with 1024 elements with 1229 nodes on the boundary. The time step dt' is initially set to be 0.03 and adaptively changed with the Courant number of $C_o = 0.4$. The two non-dimensional wave heights of $H' = 0.2$ and 0.6 is used for comparison with 2D results in Grilli and Svendsen [32]. Similar to the previous example the mass and energy error is used as a check of accuracy for the simulation (see Figure 39). As expected , the volume and energy error changes during the reflection process, but converges almost to the same error value after reflection.

H'_I	H'_R	R_u Current	R_u [32]
0.2	0.1913	0.423	0.42920
0.6	0.5365	1.675	1.67100

Table 5: Comparing the incident wave height with wave height due to reflection. After reflection , due to nonlinearity , the exact solitary wave loose almost 10% of it amplitude.The maximum run-up calculated in current simulation is also compared with Grilli and Svendsen [32]

4.3.3 Periodic wave

A stream function wave (SFW) [54] is a numerically exact periodic solution of a FNPF problem in depth h, in a coordinate system which moves with the speed
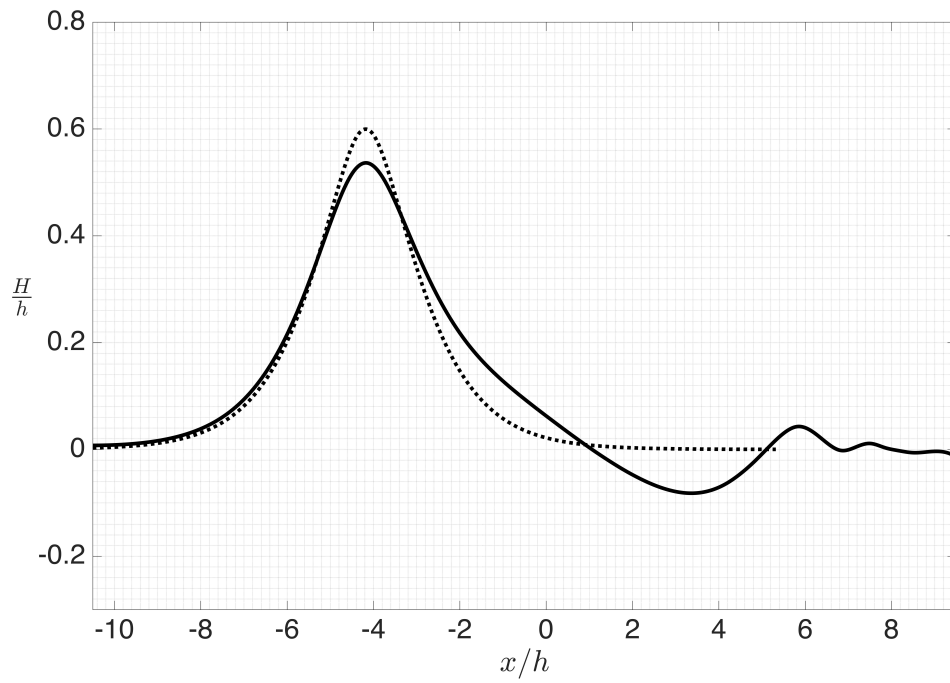
Figure 37: Reflection of Tanaka Solitary wave of the vertical wall in a fully non-linear potential flow regime. After the reflection, the solitary wave looses 10% of its height while generating a trail due to nonlinearities. Dotted line shows the incident wave with $H' = 0.6$ and the solid line shows the reflected wave.
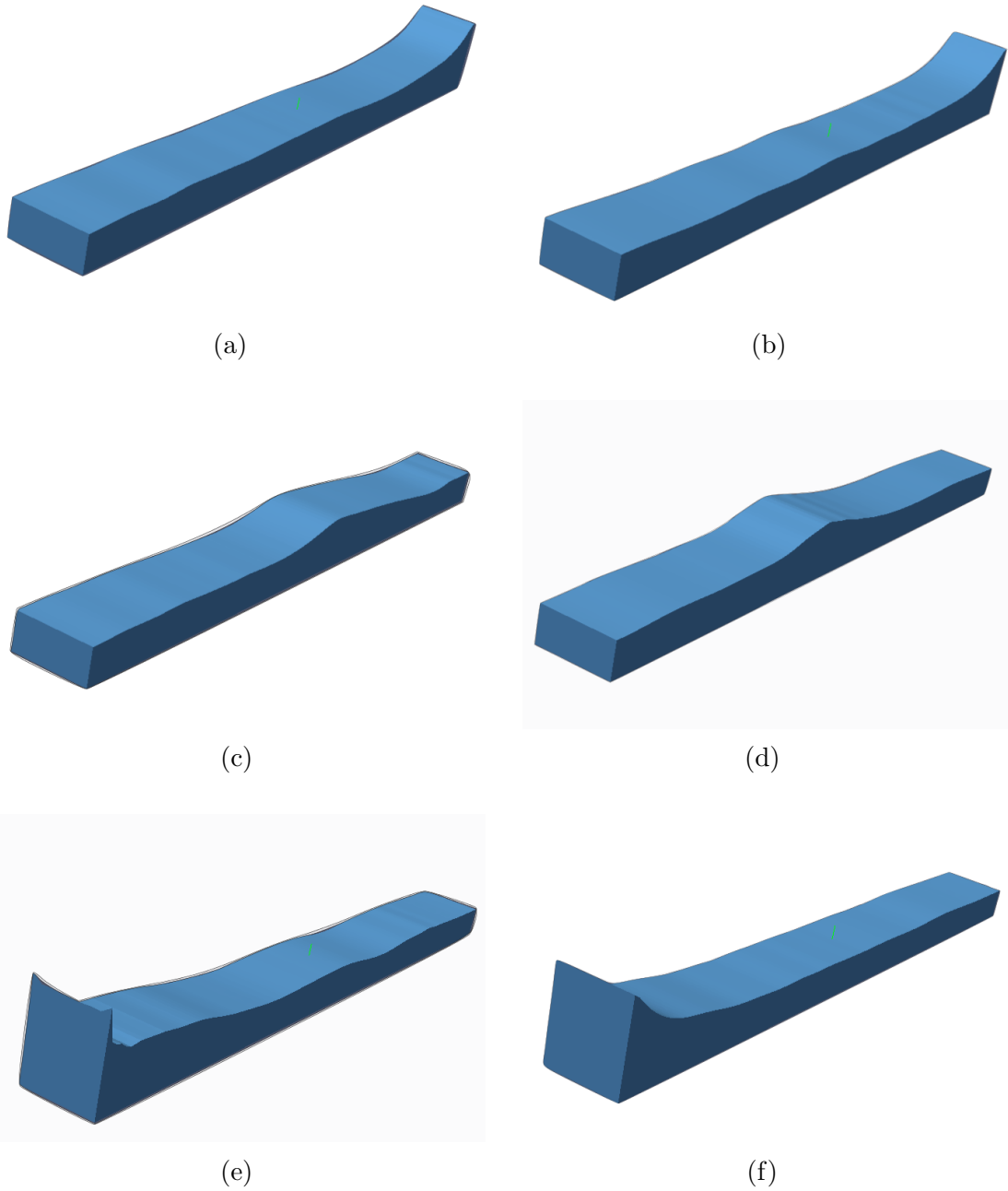
Figure 38: Reflection of solitary wave of vertical wall , with and without the end condition for the second reflection of the solitary wave with wave height of $H' = 0.6$. (a) ,(c) and (e) are the progression of reflection of solitary wave with no *corner Condition* for the values of field variable ϕ, (b),(d) and (f) are for the same numerical simulation with special treatment of the filed variable ϕ based on velocity compatibility condition. as Solitary wave propagate toward the vertical wall the numerical error for the tangential derivatives increases and without proper treatment of edges and corners the simulation will fail.
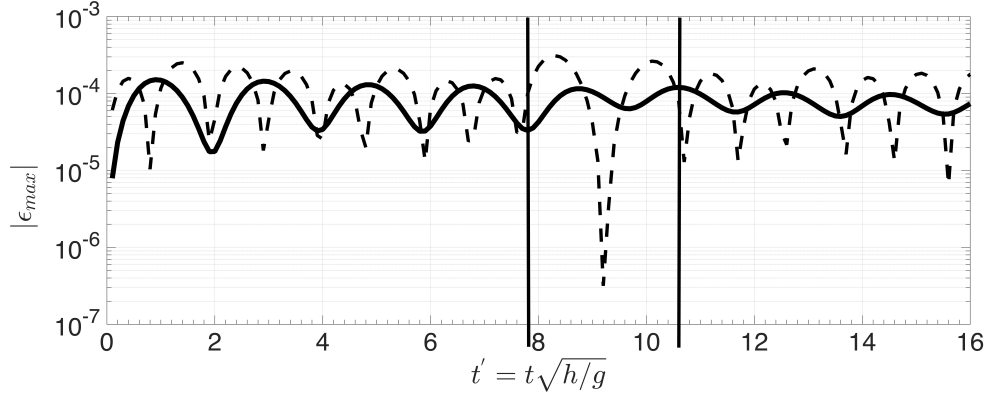
Figure 39: The maximum energy and mass error for a reflection of solitary wave of $H' = 0.6$ with Courant number of $C_o = 0.4$ of a vertical wall. The solitary wave enters the reflection zone at $t' = 7.79$ and exit the reflection zone at $t' = 10.62$. The reflection zone is shown with two vertical black lines. as expected during the reflection process the maximum energy and volume error will change and after the complete reflection, the energy and mass error converge to almost it's incident values.

of the wave $(C = L/T)$. Using the 2D version of Grilli and Horrillo [30] of stream function with zero mass flux, SFW can be modeled as :

$$\Psi(\theta, z) = \sum_{j=1}^{n} (jk)^2 X(j) cosh(jk(h + z)) sin(j\theta) - (U - c)z \qquad (120)$$

in which $\theta = k(x - ct)$ and $X(j)$ is a set of n numerical coefficients calculated iteratively to satisfy the free surface boundary conditions for a specified wave height and period. The horizontal velocity is obtained from Eq.(120)) in the original coordinate system as

$$u(\theta, z) = -\sum_{j=1}^{n} (jk) X(j) cosh(jk(h + z)) cos(j\theta) + U \qquad (121)$$

and knowing that $\frac{\partial \theta}{\partial t} = -ck$, we can calculate the local horizontal acceleration as

$$\frac{\partial u}{\partial t} = -c \sum_{j=1}^{n} (jk)^2 X(j) cosh jk(h + z) sin j\theta \qquad (122)$$

These equations are used to specify the kinematics of an incident SFW over a vertical wave maker boundary at each point through the width of the tank boundary.

137
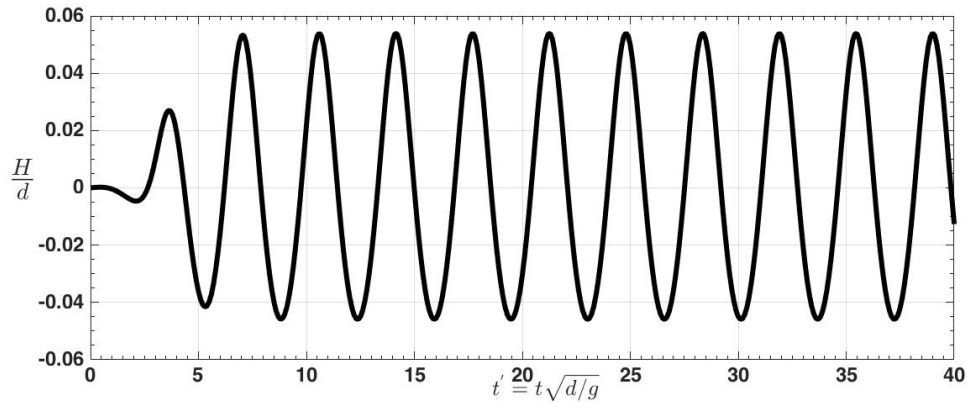
Figure 40: Generation of numerically exact nonlinear periodic wave similar to Grilli et. al. [30]. A ramp up time equal to to two wave period is being use at the beginning of the simulation for avoiding the singularities due to a hard start of the simulations.

The numerical simulation similar to Grilli and Horrillo's [30] in performed in a tank with length 10 times the depth ($L' = 10$) and width 2 times the depth ($W' = 2$). The domain is discretized with $dx' = 0.25$ in length and depth and $dx' = 0.5$ in width. We simulate wave propagation with 832 quadrilateral cubic B-spline elements (1,070 nodes) with the absorbing beach (AB) starting at $x_{AB} = 6.5$, with a strength $\nu = 0.63$.

Incident waves are generated on the leftward boundary of the tank as (zero-mass-flux) streamfunction waves, with height $H' = 0.15$, and period $T' = 3.5515$. With these values, we find a wavelength $L' = 2.07$ and steepness $H'/L' = 0.072$. These are nearly deep water waves with significant nonlinearity. In order to prevent an unstable shock from appearing at the wavemaker boundary at the beginning of the simulation, the velocity field is multiplied by a tanh-like tapering function, $D(t)$, similar to Grilli and Horrillo [30], where we take the startup time, T'_{start} to be two wave period.

In order to test the accuracy of the waves generated, a wave gauge is positioned at $x' = 4.0$, approximately two wavelengths away from the wavemaker, and one

138
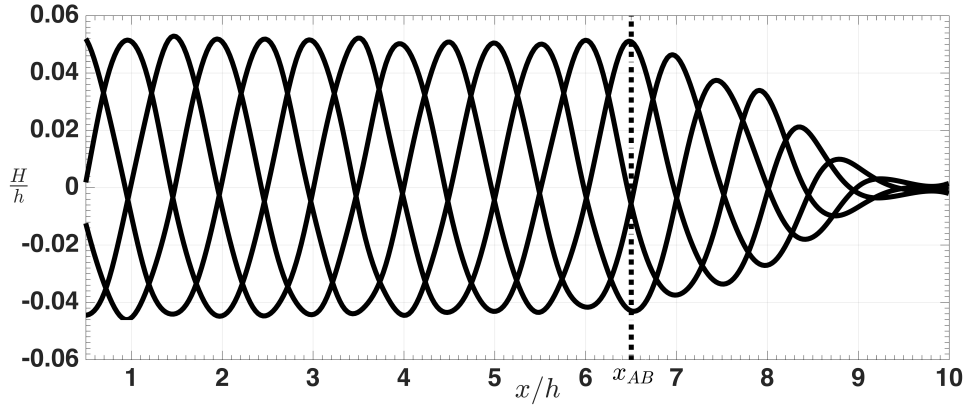
Figure 41: implementation of absorbing beach in Numerical wave tank for avoiding the reflection from the end of the tank into the computational domain.
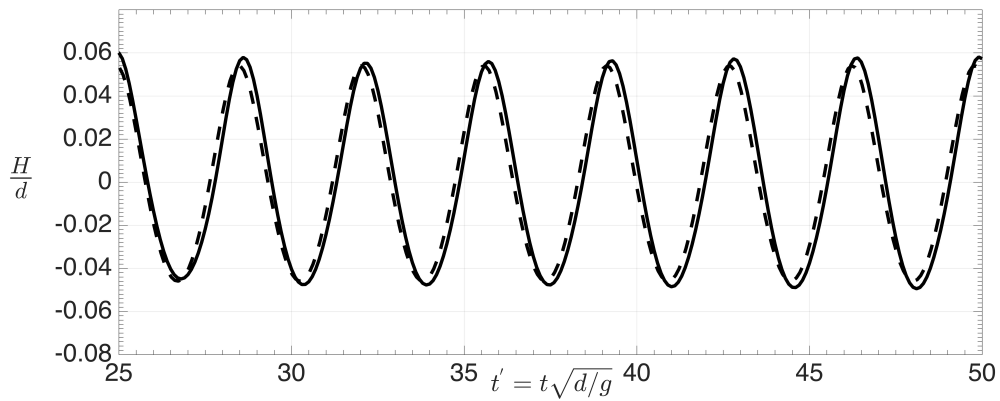
Figure 42: Comparing the theoretical value of stream function wave with the measured wave profile on a wave gauge in the middle of the tank. The cycles average RMSE between the theoretical wave maker and measured wave in the middle of the tank is equal $\bar{e}_{RMSE} = 8.73 \times 10^{-2}$.

wavelength away from the start of the absorbing beach. The time-step is initially set to be $t' = T'/30$ and is adaptive to maintain a constant Courant number ($C_o = 0.4$). The cycle averaged root mean square error between the theory and measurement at the wave gauge measured for $t' > 8T'$ and for 5 wave periods and found to be equal to 8.73×10^{-2}. It is believed that the reflection of long wave from the imperfect absorbing beach, cause this numerical error , while the energy error and volume error are in orders of 10^{-4} and 10^{-5} respectively for $t' = 50$ showing a good numerical accuracy.

4.4 Conclusion

A corner treatment condition was developed for solving BEM problems in fully non-linear potential flow applications at the free surface, where properties at the free surface are defined based on a cubic B-spline element representation. The corner treatment defines multiple nodes at locations where there are intersections of lines or surfaces, which will result in singular values within the matrix system of equations. By applying compatibility conditions at these locations (i.e. forcing the potential to be single valued and forcing velocity conditions to be single valued), these singularities are removed and replaced with compatibility equations that force a single solution at these double or triple nodes. This results in a unique solution and helps to alleviate instabilities in the solution that occur at these corner locations.

The given examples demonstrate how this special treatment of corners improve the solution in a variety of examples focused on wave propagation, with the express purpose of developing a stable, numerical wave tank for use in naval hydrodynamic applications with surface piercing bodies. Future work will include implementation of this NWT with a hybrid decomposition method that involve a simultaneous solution of the BEM system of equations with a Navier-Stokes (NS) solver, hence

the proper treatment of corner conditions will play a critical role in maintaining a stable solution that does not break down due to numerical instabilities over long computational times, which may occur in the case of simulating long time history irregular sea states.

Future work is necessary to demonstrate the method in applications with arbitrarily shaped surface piercing bodies, which may require multiple B-Spline patch definitions for the body geometry and at the free surface. Previous work (cite Grilli et al, [1, 2]) has demonstrated that a multiple patch definition at the free surface also introduces instabilities in non-linear wave problems at the intersection of patches if continuity of the patch properties does not exist, hence treatment using MII is necessary in these applications.

4.5   Acknowledgement

List of References

[1] S. Grilli and I. Svendsen, "Corner problems and global accuracy in the boundary element solution of nonlinear wave flows," *Engineering Analysis with Boundary Elements*, vol. 7, no. 4, pp. 178–195, 1990.

[2] S. T. Grilli and R. Subramanya, "Numerical modeling of wave breaking induced by fixed or moving boundaries," *Computational Mechanics*, vol. 17, no. 6, pp. 374–391, 1996.

[3] M. S. Longuet-Higgins and E. D. Cokelet, "The deformation of steep surface waves on water-i. a numerical method of computation," *Proc. R. Soc. Lond. A*, vol. 350, no. 1660, pp. 1–26, 1976.

[4] J. W. Dold and D. H. Peregrine, "An efficient boundary-integral method for steep unsteady water waves," *Numerical methods for fluid dynamics II*, vol. 671, p. 679, 1986.

[5] D. G. Dommermuth, D. K. P. Yue, W. M. Lin, R. J. Rapp, E. S. Chan, and W. K. Melville, "Deep-water plunging breakers: a comparison between potential theory and experiments," *J. of Fluid Mech.*, vol. 189, pp. 423–442, 1988.

[6] S. T. Grilli, J. Skourup, and I. A. Svendsen, "An efficient boundary element method for nonlinear water waves," *Engineering Analysis with Boundary Elements*, vol. 6, no. 2, pp. 97–107, 1989.

[7] S. T. Grilli, R. Subramanya, I. A. Svendsen, and J. Veeramony, "Shoaling of solitary waves on plane beaches," *J. Waterway, Port, Coastal, and Ocean Engng.*, vol. 120, no. 6, pp. 609–628, 1994.

[8] S. T. Grilli, I. A. Svendsen, and R. Subramanya, "Breaking criterion and characteristics for solitary waves on slopes," *J. Waterway, port, Coastal, and Ocean Engng.*, vol. 123, no. 3, pp. 102–112, 1997.

[9] F. E. Camfield, Y. Li, F. Raichlen, S. T. Grilli, I. A. Svendsen, and R. Subramanya, "Discussions and closure: Breaking criterion and characteristics for solitary waves on slopes," *J. Waterway, Port, Coastal, and Ocean Engng.*, vol. 124, no. 6, pp. 329–335, 1998.

[10] S. T. Grilli, P. Guyenne, and F. Dias, "A fully non-linear model for three-dimensional overturning waves over an arbitrary bottom," *International Journal for Numerical Methods in Fluids*, vol. 35, no. 7, pp. 829–867, 2001.

[11] P. Guyenne and S. Grilli, "Numerical study of three-dimensional overturning waves in shallow water," *Journal of Fluid Mechanics*, vol. 547, pp. 361–388, 2006.

[12] C. Fochesato, S. Grilli, and F. Dias, "Numerical modeling of extreme rogue waves generated by directional energy focusing," *Wave Motion*, vol. 44, no. 5, pp. 395–416, 2007.

[13] H. G. Sung and S. T. Grilli, "BEM computations of 3D fully nonlinear free-surface flows caused by advancing surface disturbances," *Intl. J. Offshore and Polar Engng.*, vol. 18, no. 04, pp. 292–301, 2008.

[14] S. T. Grilli, F. Dias, P. Guyenne, C. Fochesato, and F. Enet, "Progress in fully nonlinear potential flow modeling of 3d extreme ocean waves," in *Advances in numerical simulation of nonlinear water waves*. World Scientific, 2010, pp. 75–128.

[15] E. Guerber, M. Benoit, S. T. Grilli, and C. Buvat, "A fully nonlinear implicit model for wave interactions with submerged structures in forced or free motion," *Engineering Analysis with Boundary Elements*, vol. 36, no. 7, pp. 1151–1163, 2012.

[16] J. C. Harris, K. Kuznetsov, C. Peyrard, S. Saviot, A. Mivehchi, S. T. Grilli, M. Benoit, *et al.*, "Simulation of wave forces on a gravity based foundation by a bem based on fully nonlinear potential flow," in *The 27th International Ocean and Polar Engineering Conference*. International Society of Offshore and Polar Engineers, 2017.

[17] X. Barthelemy, M. L. Banner, W. L. Peirson, F. Fedele, M. Allis, and F. Dias, "On a unified breaking onset threshold for gravity waves in deep and intermediate depth water," *J. Fluid Mech.*, vol. 841, pp. 463–488, 2018.

[18] L. Greengard and V. Rokhlin, "A fast algorithm for particle simulations," *J. Comput. Phys.*, vol. 73, pp. 325–348, 1987.

[19] C. Fochesato and F. Dias, "A fast method for nonlinear three-dimensional free-surface waves," in *Proc. Royal Soc. London A*, vol. 462, no. 2073. The Royal Society, 2006, pp. 2715–2735.

[20] S. B. Nimmala, S. C. Yim, and S. T. Grilli, "An efficient three-dimensional FNPF numerical wave tank for large-scale wave basin experiment simulation," *J. Offshore Mech. and Arctic Engng.*, vol. 135, no. 2, p. 021104, 2013.

[21] J. C. Harris, E. Dombre, M. Benoit, and S. T. Grilli, "Fast integral equation methods for fully nonlinear water wave modeling," in *Proc. 24th Intl. Ocean and Polar Engng. Conf.* International Society of Offshore and Polar Engineers, 2014, pp. 583–590.

[22] J. Harris, E. Dombre, A. Mivehchi, M. Benoit, S. Grilli, and C. Peyrard, "Progress in fully nonlinear wave modeling for wave-structure interaction," *Proceedings of the 15th Journée de lHydrodynamique*, p. 12, 2016.

[23] G. Symm, "Integral equation methods in potential theory. ii," *Proc. R. Soc. Lond. A*, vol. 275, no. 1360, pp. 33–46, 1963.

[24] J. Lachat and J. Watson, "Effective numerical treatment of boundary integral equations: a formulation for three-dimensional elastostatics," *International Journal for Numerical Methods in Engineering*, vol. 10, no. 5, pp. 991–1005, 1976.

[25] A. K. Mitra and M. S. Ingber, "A multiple-node method to resolve the difficulties in the boundary integral equation method caused by corners and discontinuous boundary conditions," *Intl. J. Num. Methods in Engng.*, vol. 36, no. 10, pp. 1735–1746, 1993.

[26] A. Young, "A single-domain boundary element method for 3-d elastostatic crack analysis using continuous elements," *International journal for numerical methods in engineering*, vol. 39, no. 8, pp. 1265–1293, 1996.

[27] L. Gray and E. Lutz, "On the treatment of corners in the boundary element method," *J. Computational and Applied Math.*, vol. 32, no. 3, pp. 369–386, 1990.

[28] Z.-Y. Yan, "Treatment of sharp edges & corners in the acoustic boundary element method under neumann boundary condition," *COMPUTER MODELING IN ENGINEERING AND SCIENCES*, vol. 13, no. 2, p. 81, 2006.

[29] Q. Deng, C. G. Li, S. L. Wang, H. Tang, and H. Zheng, "A new method to the treatment of corners in the bem," *Engineering Analysis with Boundary Elements*, vol. 37, no. 1, pp. 182–186, 2013.

[30] S. T. Grilli and J. Horrillo, "Numerical generation and absorption of fully nonlinear periodic waves," *Journal of Engineering Mechanics*, vol. 123, no. 10, pp. 1060–1069, 1997.

[31] S. T. Grilli and J. Horrillo, "Shoaling of periodic waves over barred-beaches in a fully nonlinear numerical wave tank," *Intl. J. Offshore and Polar Engng.*, vol. 9, no. 4, pp. 257–263, 1999.

[32] S. Grilli and I. Svendsen, "The propagation and runup of solitary waves on steep slopes," *Center for Applied Coastal Research, University of Delaware, Research Report*, no. 91-4, 1991.

[33] H. G. Sung and S. T. Grilli, "Numerical modeling of nonlinear surfacewaves caused by surface effect ships dynamics and kinematics," in *Proc. 15th Intl. Offshore and Polar Engng. Conf.* International Society of Offshore and Polar Engineers, 2005, pp. 124–131.

[34] H. G. Sung and S. T. Grilli, "Combined eulerian-lagrangian or pseudo-lagrangian descriptions of waves caused by an advancing free surface disturbance," in *Proc. 16th Intl. Offshore and Polar Engng. Conf.*, vol. 3. International Society of Offshore and Polar Engineers, 2006, pp. 487–494.

[35] A. Clément, "Coupling of two absorbing boundary conditions for 2D time-domain simulations of free surface gravity waves," *J. Comput. Phys.*, vol. 126, no. 1, pp. 139–151, 1996.

[36] R. Cointe, "Numerical simulation of a wave channel," *Engineering Analysis with Boundary Elements*, vol. 7, no. 4, pp. 167–177, 1990.

[37] J. Zhang, M. Kashiwagi, *et al.*, "Application of ale to nonlinear wave diffraction by a non-wall-sided structure," in *Proc. 27th Intl. Ocean and Polar Engng. Conf.* International Society of Offshore and Polar Engineers, 2017.

[38] D. Kring, F. Korsmeyer, J. Singer, D. Danmeier, and J. White, "Accelerated nonlinear wave simulations for large structures," in *7th International Conference on Numerical Ship Hydrodynamics, Nantes, France*, 1999, pp. 1–16.

[39] B. Büchmann, "Accuracy and stability of a set of free-surface time-domain boundary element models based on B-splines," *Intl. J. Numerical Methods in Fluids*, vol. 33, pp. 125–155, 2000.

[40] C. Fochesato, S. Grilli, and P. Guyenne, "Note on non-orthogonality of local curvilinear co-ordinates in a three-dimensional boundary element method," *International journal for numerical methods in fluids*, vol. 48, no. 3, pp. 305–324, 2005.

[41] P. L.-F. Liu, H.-W. Hsu, and M. H. Lean, "Applications of boundary integral equation methods for two-dimensional non-linear water wave problems," *International journal for numerical methods in fluids*, vol. 15, no. 9, pp. 1119–1141, 1992.

[42] G. H. Behforooz and N. PAPAMICHAEL, "End conditions for cubic spline interpolation," *IMA J. Applied Math.*, vol. 23, no. 3, pp. 355–366, 1979.

[43] B. A. Barsky, "End conditions and boundary conditions for uniform b-spline curve and surface representations," *Computers in Industry*, vol. 3, no. 1-2, pp. 17–29, 1982.

[44] C. De Boor, "Convergence of cubic spline interpolation with the not-a-knot condition." WISCONSIN UNIV-MADISON MATHEMATICS RESEARCH CENTER, Tech. Rep., 1985.

[45] A. Mivehchi, J. C. Harris, S. T. Grilli, J. M. Dahl, C. M. O'Reilly, K. Kuznetsov, and C. F. Janssen, "A hybrid solver based on efficient BEM-potential and LBM-NS models: recent BEM developments and applications to naval hydrodynamics," in *Proc. 27th Intl. Ocean and Polar Engng. Conf.* International Society of Offshore and Polar Engineers, 2017, pp. 721–728.

[46] M. S. Longuet-Higgins, "Parametric solutions for breaking waves," *J. Fluid Mech.*, vol. 121, pp. 403–424, 1982.

[47] Y. Saad and M. H. Schultz, "GMRES: a generalized minimum residual algorithm for solving nonsymmetric linear systems," *SIAM Journal on Scientific and Statistical Computing*, vol. 7, pp. 856–869, 1986.

[48] R. Yokota, J. P. Bardhan, M. G. Knepley, L. A. Barba, and T. Hamada, "Biomolecular electrostatics using a fast multipole BEM on up to 512 GPUs and a billion unknowns," *Computer Physics Communications*, vol. 182, pp. 1272–1283, 2011.

[49] R. Yokota, "An FMM based on dual tree traversal for many-core architectures," *J. Algorithms and Computational Tech.*, vol. 7, pp. 301–324, 2013.

[50] R. Yokota and L. Barba, "A tuned and scalable fast multipole method as a preeminent algorithm for exascale systems," *International Journal of High-Performance Computing Applications*, vol. 26, pp. 337–346, 2012.

[51] W. Dehnen, "A hierarchical O(N) force calculation algorithm," *Journal of Computational Physics*, vol. 179, pp. 27–42, 2002.

[52] M. Tanaka, "The stability of solitary waves," *Physics Fluids*, vol. 29, no. 3, pp. 650–655, 1986.

[53] G. H. Behforooz, "A comparison of thee (3) and not-a-knot cubic splines," *Applied Mathematics and Computation*, vol. 72, no. 2-3, pp. 219–223, 1995.

[54] R. A. Dalrymple, "Wave-induced mass transport in water waves," *J. Waterway, port, Coastal, and Ocean Engng.*, vol. 102, no. 2, pp. 255–264, 1976.

BIBLIOGRAPHY

Abbott, I. H. and Von Doenhoff, A. E., *Theory of wing sections, including a summary of airfoil data.* Courier Corporation, 1959.

Alessandrini, B., "These dhabilitation en vue de diriger les recherches," *Ecole Centrale de Nantes, Nantes*, 2007.

Anderson, J. M., Streitlien, K., Barrett, D. S., and Triantafyllou, M. S., "Oscillating foils of high propulsive efficiency," *Journal of Fluid Mechanics*, vol. 360, pp. 41–72, Apr. 1998.

Autonomous Undersea Vehicle Applications Center, "AUV system spec sheet: Razor configuration," 2015, [Online; accessed 09-27-2015]. [Online]. Available: http://auvac.org/configurations/view/218

Banari, A., Janßen, C. F., and Grilli, S. T., "An efficient lattice boltzmann multiphase model for 3d flows with large density ratios at high reynolds numbers," *Computers & Mathematics with Applications*, vol. 68, no. 12, pp. 1819–1843, 2014.

Barsky, B. A., "End conditions and boundary conditions for uniform b-spline curve and surface representations," *Computers in Industry*, vol. 3, no. 1-2, pp. 17–29, 1982.

Barthelemy, X., Banner, M. L., Peirson, W. L., Fedele, F., Allis, M., and Dias, F., "On a unified breaking onset threshold for gravity waves in deep and intermediate depth water," *J. Fluid Mech.*, vol. 841, pp. 463–488, 2018.

Behforooz, G. H., "A comparison of thee (3) and not-a-knot cubic splines," *Applied Mathematics and Computation*, vol. 72, no. 2-3, pp. 219–223, 1995.

Behforooz, G. H. and PAPAMICHAEL, N., "End conditions for cubic spline interpolation," *IMA J. Applied Math.*, vol. 23, no. 3, pp. 355–366, 1979.

Blevins, E. and Lauder, G. V., "Swimming near the substrate: a simple robotic model of stingray locomotion," *Bioinspiration & Biomimetics*, vol. 8, no. 1, p. 016005, Mar. 2013.

Büchmann, B., "Accuracy and stability of a set of free-surface time-domain boundary element models based on B-splines," *Intl. J. Numerical Methods in Fluids*, vol. 33, pp. 125–155, 2000.

Cabral, J., Wrobel, L., and Brebbia, C., "A BEM formulation using B-splines: I-uniform blending functions," *Engineering analysis with boundary elements*, vol. 7, no. 3, pp. 136–144, 1990.

Cabral, J., Wrobel, L., and Brebbia, C., "A BEM formulation using B-splines: II-multiple knots and non-uniform blending functions," *Engineering Analysis with Boundary Elements*, vol. 8, no. 1, pp. 51–55, 1991.

Camfield, F. E., Li, Y., Raichlen, F., Grilli, S. T., Svendsen, I. A., and Subramanya, R., "Discussions and closure: Breaking criterion and characteristics for solitary waves on slopes," *J. Waterway, Port, Coastal, and Ocean Engng.*, vol. 124, no. 6, pp. 329–335, 1998.

Clément, A., "Coupling of two absorbing boundary conditions for 2D time-domain simulations of free surface gravity waves," *J. Comput. Phys.*, vol. 126, no. 1, pp. 139–151, 1996.

Cointe, R., "Numerical simulation of a wave channel," *Engineering Analysis with Boundary Elements*, vol. 7, no. 4, pp. 167–177, 1990.

Cointe, R. and Tulin, M. P., "A theory of steady breakers," *J. Fluid Mech.*, vol. 276, pp. 1–20, 1994.

Cui, E. and Zhang, X., *Ground Effect Aerodynamics, Encyclopedia of Aerospace Engineering.* John Wiley and Sons, Inc., 2015.

Curet, O. M., Patankar, N. A., Lauder, G. V., and MacIver, M. A., "Mechanical properties of a bio-inspired robotic knifefish with an undulatory propulsor," *Bioinspiration & Biomimetics*, vol. 6, no. 2, p. 026004, June 2011.

Dalrymple, R. A., "Wave-induced mass transport in water waves," *J. Waterway, port, Coastal, and Ocean Engng.*, vol. 102, no. 2, pp. 255–264, 1976.

De Boor, C., "Convergence of cubic spline interpolation with the not-a-knot condition." WISCONSIN UNIV-MADISON MATHEMATICS RESEARCH CENTER, Tech. Rep., 1985.

Dehnen, W., "A hierarchical O(N) force calculation algorithm," *Journal of Computational Physics*, vol. 179, pp. 27–42, 2002.

Deng, Q., Li, C. G., Wang, S. L., Tang, H., and Zheng, H., "A new method to the treatment of corners in the bem," *Engineering Analysis with Boundary Elements*, vol. 37, no. 1, pp. 182–186, 2013.

Derakhti, M., Banner, M. L., and Kirby, J. T., "Predicting the breaking strength of gravity water waves in deep and intermediate depth," *J. Fluid Mech.*, vol. 848, 2018.

Derakhti, M. and Kirby, J. T., "Breaking-onset, energy and momentum flux in unsteady focused wave packets," *J. Fluid Mech.*, vol. 790, pp. 553–581, 2016.

d'Humières, D., "Multiple–relaxation–time lattice boltzmann models in three dimensions," *Philosophical Transactions of the Royal Society of London A: Mathematical, Physical and Engineering Sciences*, vol. 360, no. 1792, pp. 437–451, 2002.

Doctors, L. J. and Sharma, S. D., "The wave resistance of an air-cushion vehicle in steady and accelerated motion," *J Ship Res.*, vol. 16, pp. 248–260, 1972.

Dold, J. W. and Peregrine, D. H., "An efficient boundary-integral method for steep unsteady water waves," *Numerical methods for fluid dynamics II*, vol. 671, p. 679, 1986.

Dommermuth, D. G., Yue, D. K. P., Lin, W. M., Rapp, R. J., Chan, E. S., and Melville, W. K., "Deep-water plunging breakers: a comparison between potential theory and experiments," *J. of Fluid Mech.*, vol. 189, pp. 423–442, 1988.

Dunavant, D., "High degree efficient symmetrical gaussian quadrature rules for the triangle," *International journal for numerical methods in engineering*, vol. 21, no. 6, pp. 1129–1148, 1985.

Duncan, J. H., "An experimental investigation of breaking waves produced by a towed hydrofoil," *Proc. R. Soc. Lond. A*, vol. 377, no. 1770, pp. 331–348, 1981.

Duncan, J. H., "The breaking and non-breaking wave resistance of a two-dimensional hydrofoil," *J. Fluid Mech.*, vol. 126, pp. 507–520, 1983.

Fernandez-Prats, R., Raspa, V., Thiria, B., Huera-Huarte, F., and Godoy-Diana, R., "Large-amplitude undulatory swimming near a wall," *Bioinspiration & Biomimetics*, vol. 10, no. 1, p. 016003, Feb. 2015.

Fochesato, C., Grilli, S., and Guyenne, P., "Note on non-orthogonality of local curvilinear co-ordinates in a three-dimensional boundary element method," *International journal for numerical methods in fluids*, vol. 48, no. 3, pp. 305–324, 2005.

Fochesato, C. and Dias, F., "A fast method for nonlinear three-dimensional free-surface waves," in *Proc. Royal Soc. London A*, vol. 462, no. 2073. The Royal Society, 2006, pp. 2715–2735.

Fochesato, C., Grilli, S., and Dias, F., "Numerical modeling of extreme rogue waves generated by directional energy focusing," *Wave Motion*, vol. 44, no. 5, pp. 395–416, 2007.

Gray, J., "Studies in Animal Locomotion VI. The Propulsive Powers of the Dolphin," *Journal of Experimental Biology*, vol. 13, no. 2, pp. 192–199, Apr. 1936.

Gray, L. and Lutz, E., "On the treatment of corners in the boundary element method," *J. Computational and Applied Math.*, vol. 32, no. 3, pp. 369–386, 1990.

Greengard, L. and Rokhlin, V., "A fast algorithm for particle simulations," *J. Comput. Phys.*, vol. 73, pp. 325–348, 1987.

Grilli, S. and Svendsen, I., "The propagation and runup of solitary waves on steep slopes," *Center for Applied Coastal Research, University of Delaware, Research Report*, no. 91-4, 1991.

Grilli, S. and Svendsen, I., "Corner problems and global accuracy in the boundary element solution of nonlinear wave flows," *Engineering Analysis with Boundary Elements*, vol. 7, no. 4, pp. 178–195, 1990.

Grilli, S. T., "On the development and application of hybrid numerical models in nonlinear free surface hydrodynamics," in *Proc. 8th Int. Conf. on Hydrodynamics*, 2008, pp. 21–50.

Grilli, S. T., Dias, F., Guyenne, P., Fochesato, C., and Enet, F., "Progress in fully nonlinear potential flow modeling of 3d extreme ocean waves," in *Advances in numerical simulation of nonlinear water waves*. World Scientific, 2010, pp. 75–128.

Grilli, S. T., Guyenne, P., and Dias, F., "A fully non-linear model for three-dimensional overturning waves over an arbitrary bottom," *International Journal for Numerical Methods in Fluids*, vol. 35, no. 7, pp. 829–867, 2001.

Grilli, S. T. and Horrillo, J., "Numerical generation and absorption of fully nonlinear periodic waves," *Journal of Engineering Mechanics*, vol. 123, no. 10, pp. 1060–1069, 1997.

Grilli, S. T. and Horrillo, J., "Shoaling of periodic waves over barred-beaches in a fully nonlinear numerical wave tank," *Intl. J. Offshore and Polar Engng.*, vol. 9, no. 4, pp. 257–263, 1999.

Grilli, S. T., Skourup, J., and Svendsen, I. A., "An efficient boundary element method for nonlinear water waves," *Engineering Analysis with Boundary Elements*, vol. 6, no. 2, pp. 97–107, 1989.

Grilli, S. T. and Subramanya, R., "Quasi-singular integrals in the modeling of nonlinear water waves in shallow water," *Engineering Analysis with Boundary Elements*, vol. 13, no. 2, pp. 181–191, 1994.

Grilli, S. T. and Subramanya, R., "Numerical modeling of wave breaking induced by fixed or moving boundaries," *Computational Mechanics*, vol. 17, no. 6, pp. 374–391, 1996.

Grilli, S. T., Subramanya, R., Svendsen, I. A., and Veeramony, J., "Shoaling of solitary waves on plane beaches," *J. Waterway, Port, Coastal, and Ocean Engng.*, vol. 120, no. 6, pp. 609–628, 1994.

Grilli, S. T., Svendsen, I. A., and Subramanya, R., "Breaking criterion and characteristics for solitary waves on slopes," *J. Waterway, port, Coastal, and Ocean Engng.*, vol. 123, no. 3, pp. 102–112, 1997.

Guerber, E., Benoit, M., Grilli, S. T., and Buvat, C., "A fully nonlinear implicit model for wave interactions with submerged structures in forced or free motion," *Engineering Analysis with Boundary Elements*, vol. 36, no. 7, pp. 1151–1163, 2012.

Guignard, S., Grilli, S. T., *et al.*, "Modeling of wave shoaling in a 2D-NWT using a spilling breaker model," in *Proc. 11th Intl. Offshore and Polar Engng. Conf.*, vol. 3. International Society of Offshore and Polar Engineers, 2001, pp. 116–123.

Guyenne, P. and Grilli, S., "Numerical study of three-dimensional overturning waves in shallow water," *Journal of Fluid Mechanics*, vol. 547, pp. 361–388, 2006.

Harris, J., Dombre, E., Benoit, M., and Grilli, S., "A comparison of methods in fully nonlinear boundary element numerical wave tank development," *14émes Journées de lHydrodynamique*, 2014.

Harris, J., Dombre, E., Mivehchi, A., Benoit, M., Grilli, S., and Peyrard, C., "Progress in fully nonlinear wave modeling for wave-structure interaction," *Proceedings of the 15th Journée de lHydrodynamique*, p. 12, 2016.

Harris, J. C., Dombre, E., Benoit, M., and Grilli, S. T., "Fast integral equation methods for fully nonlinear water wave modeling," in *Proc. 24th Intl. Ocean and Polar Engng. Conf.* International Society of Offshore and Polar Engineers, 2014, pp. 583–590.

Harris, J. C., Kuznetsov, K., Peyrard, C., Saviot, S., Mivehchi, A., Grilli, S. T., Benoit, M., *et al.*, "Simulation of wave forces on a gravity based foundation by a bem based on fully nonlinear potential flow," in *The 27th International Ocean and Polar Engineering Conference.* International Society of Offshore and Polar Engineers, 2017.

Hu, J., Guo, L., and Sun, S., "Numerical simulation of the potential flow around a submerged hydrofoil with fully nonlinear free-surface conditions," *J. Coastal Res.*, vol. 34, no. 1, pp. 238–252, 2017.

Izraelevitz, J. S. and Triantafyllou, M. S., "Adding in-line motion and model-based optimization offers exceptional force control authority in flapping foils," *Journal of Fluid Mechanics*, vol. 742, pp. 5–34, 2014.

Janssen, C., "Kinetic approaches for the simulation of non-linear free surface flow problems in civil and environmental engng," Ph.D. dissertation, PhD thesis, Technical Univ. Braunschweig, 2010.

Janssen, C. F., Krafczyk, M., Grilli, S., *et al.*, "Modeling of wave breaking andwave-structure interactions by coupling of fully nonlinear potential flow and lattice-boltzmann models," in *The Twentieth International Offshore and Polar Engineering Conference.* International Society of Offshore and Polar Engineers, 2010.

Janßen, C. F., Mierke, D., Überrück, M., Gralher, S., and Rung, T., "Validation of the gpu-accelerated cfd solver elbe for free surface flow problems in civil and environmental engineering," *Computation*, vol. 3, no. 3, pp. 354–385, 2015.

Krafczyk, M., Tölke, J., and Luo, L.-S., "Large-eddy simulations with a multiple-relaxation-time lbe model," *International Journal of Modern Physics B*, vol. 17, no. 01n02, pp. 33–39, 2003.

Kring, D., Korsmeyer, F., Singer, J., Danmeier, D., and White, J., "Accelerated nonlinear wave simulations for large structures," in *7th International Conference on Numerical Ship Hydrodynamics, Nantes, France*, 1999, pp. 1–16.

Lachat, J. and Watson, J., "Effective numerical treatment of boundary integral equations: a formulation for three-dimensional elastostatics," *International Journal for Numerical Methods in Engineering*, vol. 10, no. 5, pp. 991–1005, 1976.

Liang, H., Wang, X., Zou, L., and Zong, Z., "Numerical study of two-dimensional heaving airfoils in ground effect," *Journal of Fluids and Structures*, vol. 48, pp. 188–202, jul 2014.

Licht, S. C., Wibawa, M. S., Hover, F. S., and Triantafyllou, M. S., "In-line motion causes high thrust and efficiency in flapping foils that use power downstroke," *The Journal of Experimental Biology*, vol. 213, no. 1, pp. 63–71, Jan. 2010.

Licht, S., Polidoro, V., Flores, M., Hover, F. S., and Triantafyllou, M. S., "Design and projected performance of a flapping foil AUV," *IEEE Journal of Oceanic Engineering*, vol. 29, no. 3, pp. 786–794, 2004.

Licht, S. C., "Biomimetic oscillating foil propulsion to enhance underwater vehicle agility and maneuverability," Thesis, Massachusetts Institute of Technology, 2008.

Liu, P. L.-F., Hsu, H.-W., and Lean, M. H., "Applications of boundary integral equation methods for two-dimensional non-linear water wave problems," *International journal for numerical methods in fluids*, vol. 15, no. 9, pp. 1119–1141, 1992.

Long, J. H., Schumacher, J., Livingston, N., and Kemp, M., "Four flippers or two? Tetrapodal swimming with an aquatic robot," *Bioinspiration & Biomimetics*, vol. 1, no. 1, pp. 20–29, Mar. 2006.

Longuet-Higgins, M. S., "Parametric solutions for breaking waves," *J. Fluid Mech.*, vol. 121, pp. 403–424, 1982.

Longuet-Higgins, M. S. and Cokelet, E. D., "The deformation of steep surface waves on water-i. a numerical method of computation," *Proc. R. Soc. Lond. A*, vol. 350, no. 1660, pp. 1–26, 1976.

Lu, H., Lua, K. B., Lim, T. T., and Yeo, K. S., "Ground effect on the aerodynamics of a two-dimensional oscillating airfoil," *Experiments in Fluids*, vol. 55, no. 7, pp. 1–15, July 2014.

Maestre, J., Cuesta, I., and Pallares, J., "An unsteady 3d isogeometrical boundary element analysis applied to nonlinear gravity waves," *Computer Methods in Applied Mechanics and Engineering*, vol. 310, pp. 112–133, 2016.

Mitra, A. K. and Ingber, M. S., "A multiple-node method to resolve the difficulties in the boundary integral equation method caused by corners and discontinuous boundary conditions," *Intl. J. Num. Methods in Engng.*, vol. 36, no. 10, pp. 1735–1746, 1993.

Mivehchi, A., Dahl, J., and Licht, S., "Heaving and pitching oscillating foil propulsion in ground effect," *Journal of Fluids and Structures*, vol. 63, pp. 174–187, 2016.

Mivehchi, A., Dahl, J. M., and Licht, S., "Thrust and lift generation of heaving and pitching oscillating foil propulsion in ground effect," *Bulletin of the American Physical Society*, vol. 60, 2015.

Mivehchi, A., Harris, J. C., Grilli, S. T., Dahl, J. M., O'Reilly, C. M., Kuznetsov, K., and Janssen, C. F., "A hybrid solver based on efficient BEM-potential and LBM-NS models: recent BEM developments and applications to naval hydrodynamics," in *Proc. 27th Intl. Ocean and Polar Engng. Conf.* International Society of Offshore and Polar Engineers, 2017, pp. 721–728.

Mivehchi, A., Persichetti, A., Dunham, B., and Dahl, J. M., "Investigation of energy harvesting using flapping foils," *Bulletin of the American Physical Society*, vol. 58, 2013.

Molina, J. and Zhang, X., "Aerodynamics of a heaving airfoil in ground effect," *AIAA journal*, vol. 49, no. 6, pp. 1168–1179, 2011.

Moryossef, Y. and Levy, Y., "Effect of Oscillations on Airfoils in Close Proximity to the Ground," *AIAA Journal*, vol. 42, no. 9, pp. 1755–1764, 2004.

Muscari, R. and Di Mascio, A., "Numerical modeling of breaking waves generated by a ship hull," *J. Marine Science and Technology*, vol. 9, no. 4, pp. 158–170, 2004.

Nimmala, S. B., Yim, S. C., and Grilli, S. T., "An efficient three-dimensional FNPF numerical wave tank for large-scale wave basin experiment simulation," *J. Offshore Mech. and Arctic Engng.*, vol. 135, no. 2, p. 021104, 2013.

Nowroozi, B. N., Strother, J. A., Horton, J. M., Summers, A. P., and Brainerd, E. L., "Whole-body lift and ground effect during pectoral fin locomotion in the northern spearnose poacher (Agonopsis vulsa)," *Zoology (Jena, Germany)*, vol. 112, no. 5, pp. 393–402, 2009.

O'Reilly, C. M., Grilli, S. T., Harris, J. C., Mivehchi, A., Janssen, C. F., and Dahl, J. M., "A Hybrid Solver Based on Efficient BEM-potential and LBM-NS Models: Recent LBM Developments and Applications to Naval Hydrodynamics," in *Proc. 27th Intl. Ocean and Polar Engng. Conf.* International Society of Offshore and Polar Engineers, 2017, p. 713 720.

O'Reilly, C., Grilli, S., Harris, J., Mivehchi, A., Janssen, C., Dahl, J., *et al.*, "A hybrid solver based on efficient bem-potential and lbm-ns models: Recent lbm developments and applications to naval hydrodynamics," in *The 27th International Ocean and Polar Engineering Conference.* International Society of Offshore and Polar Engineers, 2017.

OREILLY, C., GRILLI, S., HARRIS, J., MIVEHCHI, A., JANSSEN, C., and DAHL, J., "Development of a hybrid lbm-potential flow model for naval hydrodynamics."

Park, H. and Choi, H., "Aerodynamic characteristics of flying fish in gliding flight," *The Journal of Experimental Biology*, vol. 213, no. 19, pp. 3269–3279, Oct. 2010.

Perkins, M., Elles, D., Badlissi, G., Mivehchi, A., Dahl, J., and Licht, S., "Rolling and pitching oscillating foil propulsion in ground effect," *Bioinspiration & biomimetics*, vol. 13, no. 1, p. 016003, 2017.

Perlin, M., Choi, W., and Tian, Z., "Breaking waves in deep and intermediate waters," *Annual Review Fluid Mech.*, vol. 45, pp. 115–145, 2013.

Quinn, D. B., Lauder, G. V., and Smits, A. J., "Flexible propulsors in ground effect," *Bioinspiration & Biomimetics*, vol. 9, no. 3, p. 036008, Sept. 2014.

Quinn, D. B., Moored, K. W., Dewey, P. A., and Smits, A. J., "Unsteady propulsion near a solid boundary," *Journal of Fluid Mechanics*, vol. 742, pp. 152–170, Mar. 2014.

Rayner, J. M. V., "On the Aerodynamics of Animal Flight in Ground Effect," *Philosophical Transactions: Biological Sciences*, vol. 334, no. 1269, pp. 119–128, Oct. 1991.

Read, D. A., Hover, F. S., and Triantafyllou, M. S., "Forces on oscillating foils for propulsion and maneuvering," *Journal of Fluids and Structures*, vol. 17, no. 1, pp. 163–183, Jan. 2003.

Reliquet, G., Drouet, A., Guillerm, P., Gentaz, L., and Ferrant, P., "Simulation of wave-ship interaction in regular and irregular seas under viscous flow theory using the swense method," in *Proc. 30th Symp. Naval Hydrod.(Tasmania, 11/2014)*, 2014.

Saad, Y. and Schultz, M. H., "GMRES: a generalized minimum residual algorithm for solving nonsymmetric linear systems," *SIAM Journal on Scientific and Statistical Computing*, vol. 7, pp. 856–869, 1986.

Shikin, E. V. and Plis, A. I., *Handbook on Splines for the User.* CRC Press, 1995.

Stansell, P. and MacFarlane, C., "Experimental investigation of wave breaking criteria based on wave phase speeds," *J. Phys. Oceanography*, vol. 32, no. 5, pp. 1269–1283, 2002.

Subramani, A. K., Beck, R. F., and Schultz, W. W., "Suppression of wave-breaking in nonlinear water wave computations," in *Proc. 13th Intl. Workshop Water Waves and Floating Bodies*, 1998, pp. 139–142.

Sung, H. G. and Grilli, S. T., "Numerical modeling of nonlinear surfacewaves caused by surface effect ships dynamics and kinematics," in *Proc. 15th Intl. Offshore and Polar Engng. Conf.* International Society of Offshore and Polar Engineers, 2005, pp. 124–131.

Sung, H. G. and Grilli, S. T., "Combined eulerian-lagrangian or pseudo-lagrangian descriptions of waves caused by an advancing free surface disturbance," in *Proc. 16th Intl. Offshore and Polar Engng. Conf.*, vol. 3. International Society of Offshore and Polar Engineers, 2006, pp. 487–494.

Sung, H. G. and Grilli, S. T., "BEM computations of 3D fully nonlinear free-surface flows caused by advancing surface disturbances," *Intl. J. Offshore and Polar Engng.*, vol. 18, no. 04, pp. 292–301, 2008.

Svendsen, I. A. and Madsen, P. A., "A turbulent bore on a beach," *J. Fluid Mech.*, vol. 148, pp. 73–96, 1984.

Svendsen, I. A., Madsen, P., and Hansen, J. B., "Wave characteristics in the surf zone," in *Proc. Intl. Coastal Engineering Conf.*, 1978, pp. 520–539.

Symm, G., "Integral equation methods in potential theory. ii," *Proc. R. Soc. Lond. A*, vol. 275, no. 1360, pp. 33–46, 1963.

Tanaka, M., "The stability of solitary waves," *Physics Fluids*, vol. 29, no. 3, pp. 650–655, 1986.

Tangorra, J., Davidson, S., Madden, P., Lauder, G., and Hunter, I., "A Biorobotic Pectoral Fin for Autonomous Undersea Vehicles," in *28th Annual International Conference of the IEEE Engineering in Medicine and Biology Society, 2006. EMBS '06*, 2006, pp. 2726–2729.

Techet, A. H., "Propulsive performance of biologically inspired flapping foils at high Reynolds numbers," *Journal of Experimental Biology*, vol. 211, no. 2, pp. 274–279, Jan. 2008.

Triantafyllou, M. S., Techet, A. H., and Hover, F. S., "Review of experimental work in biomimetic foils," *Oceanic Engineering, IEEE Journal of*, vol. 29, no. 3, pp. 585–594, 2004.

Truong, T. V., Byun, D., Kim, M. J., Yoon, K. J., and Park, H. C., "Aerodynamic forces and flow structures of the leading edge vortex on a flapping wing considering ground effect," *Bioinspiration & Biomimetics*, vol. 8, no. 3, p. 036007, Sept. 2013.

Um, T. I., Chen, Z., and Bart-Smith, H., "A novel electroactive polymer buoyancy control device for bio-inspired underwater vehicles," in *Robotics and Automation (ICRA), 2011 IEEE International Conference on.* IEEE, 2011, pp. 172–177.

Ushatov, R., Power, H., and Silva, J. R., "Uniform bicubic b-splines applied to boundary element formulation for 3-d scalar problems," *Engineering analysis with boundary elements*, vol. 13, no. 4, pp. 371–381, 1994.

Wu, J., Qiu, Y. L., Shu, C., and Zhao, N., "Pitching-motion-activated flapping foil near solid walls for power extraction: A numerical investigation," *Physics of Fluids (1994-present)*, vol. 26, no. 8, p. 083601, Aug. 2014.

Wu, J., Qiu, Y. L., Shu, C., Zhao, N., and Wang, X., "An adaptive immersed boundary-lattice Boltzmann method for simulating a flapping foil in ground effect," *Computers & Fluids*, vol. 106, pp. 171–184, Jan. 2015.

Wu, J., Shu, C., Zhao, N., and Yan, W., "Fluid Dynamics of Flapping Insect Wing in Ground Effect," *Journal of Bionic Engineering*, vol. 11, no. 1, pp. 52–60, Jan. 2014.

Yan, Z.-Y., "Treatment of sharp edges & corners in the acoustic boundary element method under neumann boundary condition," *COMPUTER MODELING IN ENGINEERING AND SCIENCES*, vol. 13, no. 2, p. 81, 2006.

Yokota, R., "An FMM based on dual tree traversal for many-core architectures," *J. Algorithms and Computational Tech.*, vol. 7, pp. 301–324, 2013.

Yokota, R. and Barba, L., "A tuned and scalable fast multipole method as a preeminent algorithm for exascale systems," *International Journal of High-Performance Computing Applications*, vol. 26, pp. 337–346, 2012.

Yokota, R., Bardhan, J. P., Knepley, M. G., Barba, L. A., and Hamada, T., "Biomolecular electrostatics using a fast multipole BEM on up to 512 GPUs and a billion unknowns," *Computer Physics Communications*, vol. 182, pp. 1272–1283, 2011.

Young, A., "A single-domain boundary element method for 3-d elastostatic crack analysis using continuous elements," *International journal for numerical methods in engineering*, vol. 39, no. 8, pp. 1265–1293, 1996.

Zhang, J., Kashiwagi, M., *et al.*, "Application of ale to nonlinear wave diffraction by a non-wall-sided structure," in *Proc. 27th Intl. Ocean and Polar Engng. Conf.* International Society of Offshore and Polar Engineers, 2017.